Improvements in Flood Forecasting in Mountain Basins

through a Physically-Based Distributed Model

by

Hernan Moreno Ramirez

A Dissertation Presented in Partial Fulfillment
of the Requirements for the Degree
Doctor of Philosophy

Approved July 2012 by the
Graduate Supervisory Committee:

Enrique R. Vivoni, Chair
Benjamin L. Ruddell
David J. Gochis
Larry W. Mays
Huei-Ping Huang

ARIZONA STATE UNIVERSITY

December 2012

ABSTRACT

This doctoral thesis investigates the predictability characteristics of floods and flash floods by coupling high resolution precipitation products to a distributed hydrologic model. The research hypotheses are tested at multiple watersheds in the Colorado Front Range (CFR) undergoing warm-season precipitation. Rainfall error structures are expected to propagate into hydrologic simulations with added uncertainties by model parameters and initial conditions. Specifically, the following science questions are addressed: (1) What is the utility of Quantitative Precipitation Estimates (QPE) for high resolution hydrologic forecasts in mountain watersheds of the CFR?, (2) How does the rainfall-reflectivity relation determine the magnitude of errors when radar observations are used for flood forecasts?, and (3) What are the spatiotemporal limits of flood forecasting in mountain basins when radar nowcasts are used into a distributed hydrological model?.

The methodology consists of QPE evaluations at the site (i.e., rain gauge location), basin-average and regional scales, and Quantitative Precipitation Forecasts (QPF) assessment through regional grid-to-grid verification techniques and ensemble basin-averaged time series. The corresponding hydrologic responses that include outlet discharges, distributed runoff maps, and streamflow time series at internal channel locations, are used in light of observed and/or reference data to diagnose the suitability of fusing precipitation forecasts into a distributed model operating at multiple catchments.

Results reveal that radar and multisensor QPEs lead to an improved hydrologic performance compared to simulations driven with rain gauge data only. In addition, hydrologic performances attained by satellite products preserve the fundamental properties of basin responses, including a simple scaling relation between the relative spatial variability of runoff and its magnitude. Overall, the spatial variations contained in gridded QPEs add value for warm-season flood forecasting in mountain basins, with sparse data even if those products contain some biases. These results are encouraging and open new avenues for forecasting in regions with limited access and sparse observations.

Regional comparisons of different reflectivity –rainfall (*Z*-*R*) relations during three summer seasons, illustrated significant rainfall variability across the region. Consistently, hydrologic errors introduced by the distinct *Z*-*R* relations, are significant and proportional (in the log-log space) to errors in precipitation estimations and stream flow magnitude. The use of operational *Z*-*R* relations without prior calibration may lead to wrong estimation of precipitation, runoff magnitude and increased flood forecasting errors. This suggests that site-specific *Z*-*R* relations, prior to forecasting procedures, are desirable in complex terrain regions.

Nowcasting experiments show the limits of flood forecasting and its dependence functions of lead time and basin scale. Across the majority of the basins, flood forecasting skill decays with lead time, but the functional relation depends on the interactions between watershed properties and rainfall characteristics. Both precipitation and flood forecasting skills are noticeably

reduced for lead times greater than 30 minutes. Scale dependence of hydrologic forecasting errors demonstrates reduced predictability at intermediate-size basins, the typical scale of convective storm systems. Overall, the fusion of high resolution radar nowcasts and the convenient parallel capabilities of the distributed hydrologic model provide an efficient framework for generating accurate real-time flood forecasts suitable for operational environments.

DEDICATION

To my wife Laura for the long hours of patience, help and love during this endeavor. To my mother and family in Colombia and their noble support in pursue of my ideals.

ACKNOWLEDGMENTS

I want to express gratitude to my supervisor, Prof. Enrique Vivoni who was abundantly helpful and offered invaluable assistance, support and guidance. My greatest appreciation to Dr. David Gochis whose comments were determinant when addressing critical research issues. Deepest gratitude is also due to the members of the supervisory committee, Prof. Dr. Larry Mays, Prof. Dr. Benjamin Ruddell and Prof. Dr. Huei Ping Huang without whose knowledge and assistance helped giving good course to my research topic.

Special thanks also to Drs. Giuseppe Mascaro, Agustin Robles, Taufique Mahmood and all ASU hydrology group members, Luis Mendez-Barroso, Nicole Pierini, Tiantian Xian, Alex Baish, Cody Anderson, Tom Volo, Gretchen Hawkins for sharing the literature and invaluable assistance.

I have been fortunate to have consistent funding for this research throughout the National Weather Service Office of Hydrologic Development (Grant NWS-NWSPO-2007-2000799), a fellowship from the Advanced Study Program (ASP) at the National Center for Atmospheric Research (NCAR) and an ASU graduate scholarship. I thank the HPC facility at ASU and to the following providers of data products: AmeriFLUX and Mesowest networks, Colorado Division of Water Resources, NOAA Center for Satellite Applications and Research, and the Center for Hydrometeorology and Remote Sensing at University of California, Irvine. I particularly appreciate the comments of Dr. Pedro Restrepo (National Weather Service) on earlier versions of these chapters.

I also want to thank my family who inspired, encouraged and fully supported me in every obstacle that came my way. To my beloved wife Laura V. Alvarez whose comments and constructive critics aided during the writing and dissertation defense preparation and mother Leisa, and brothers Pablo and Diego for believing that my passion could come through reality.

TABLE OF CONTENTS

Page

CHAPTER Page

LIST OF TABLES

Table Page

LIST OF FIGURES

Figure Page

Figure Page

Figure Page

Figure Page

Figure Page

Figure Page

Figure Page

Chapter 1

INTRODUCTION

MOTIVATION

Floods, one of the deadliest natural hazards around the world, are known by their rapid occurrence and subsequent limited opportunity for early warning preparation. Only in the United States, during the past 30 years, floods have claimed on average 200 lives per year (Droegemeier et al. 2000; Ashley and Ashley 2008), leaving property damages of approximately $1.5 billion per year. Around 75% of all U.S. presidentially declared natural disasters involve floods (Fread 1995). Flash-floods, typically occurring in mountain basins, during warm-season precipitation periods, are particularly difficult to predict due to their localized occurrence and the short time basin responses that reduce the chances to timely and accurately issue forecasts.

Challenges in flash-flood forecasting in topographically complex areas can be divided in two types, according with the sequence of processes leading to their generation. First, the small spatial scales and short lifetimes of convective precipitation events make them difficult to predict as their high spatio-temporal variability limits the preservation of correlation structures with forecasting time (Ganguly and Bras 2003; Sharif et al. 2004; Lin et al. 2005). Typically, the higher potential for convective systems formation during summer, combined with the fact that irregular topography forces atmospheric circulation, constitute the essential ingredients for flood-leading storm development (Warner et al. 2000; Bongioannini et al. 2005; Nikanen 2008). Second, the inherent variability

imprinted by basin properties in a mountain block like this including topography, exposed and fractured bedrock, soil and vegetation heterogeneities, snow melting processes, aquifer characteristics and antecedent water in the system (including that of long residence times) play a determinant role on the runoff production and the time it takes to be delivered to the channel network. Together, basin properties can interact to add significant uncertainty to the attempts of flood forecasting, regardless of that carried by the incorrect estimation (in time and space) of the rainfall solely.

Hydrologic science is challenged to demonstrate significant advances towards accurate modeling and forecasting of floods and flash floods by using Quantitative Precipitation Estimates (QPE) and Forecasts (QPF) from multiple sources, when fused with the new capabilities of distributed hydrologic models. Traditionally, operational river forecasts were only based on the precipitation already measured on the ground (Collier and Kzyzysztofowicz 2000), with the implicit assumption of zero rainfall beyond the time of the last observation, a dangerous supposition in the middle of a severe storm. Additionally, the use of empirical or lumped hydrologic models limited the capacity to track evolution of the flood wave, and the distributed potential for flash floods and associated risks (landslides, debris flows, etc). Lumped, conceptual models, traditionally used in operational settings, present advantages with respect to simplicity for aggregated predictands such as the outlet streamflow. However, to fully utilize the information readily available by satellite, weather radar observations and extrapolations and Numerical Weather Predictions (NWP) in a hydrological

forecast, a need arises for more complex distributed systems (Pessoa et al. 1993; Garrote and Bras 1995; Arduino et al. 2005; Bartholmes and Todini 2005). The introduced complexity is compensated by the knowledge and quantification of different hydrologic variables (e.g. runoff, soil moisture, evapotranspiration, groundwater table) and their spatiotemporal evolution at internal and nested locations within the watershed (Ivanov et al. 2004; Reed et al. 2004; Smith et al. 2004).

The use of a distributed model in flood forecasting is also justified by the better understanding of hydrologic processes in mountain areas, as physically meaningful parameters are selected into the model framework and multiple scale processes are possible to represent with detail (Garrote and Bras 1995). For example, runoff generation and streamflow accumulation processes leading to flood wave propagation are determinants of local susceptibility to floods that can be quantified with distributed models. Additionally, physical controls on the scale dependence relations of flood forecasting can be facilitated through a distributed approach (Mascaro et al. 2010). Thereby, differences in responses and model forecasting dispersion can be explained according to soil, vegetation or channel network properties. The use of distributed models copes with the representation of the intricate characteristics of rainfall and subsequent watershed responses. A recent DIMP (Distributed Model Intercomparison) initiative investigated the role of spatial variability of landscape characteristics and of meteorological forcing on hydrologic response (Le Lay and Saulnier 2007). Results demonstrated that (i) the role of rainfall spatial variability (Winchell et al. 1998; Koren et al. 1999; Arnaud

et al. 2002), initial soil moisture conditions (Zehe et al. 2005) and catchment characteristics (Saulnier et al. 1997) are all conditioned by threshold effects on runoff generation, hence suggesting difficulty to extrapolate results to other catchments (Le Lay and Saulnier 2007).

Although complex models have received criticism during the past decades principally due to their overparameterization (Grayson et al. 2002), they provide confidence in representing the leading physical processes conducting to replicate observed predictands with accuracy. Yet, prior work to selecting the most impacting parameters and initial conditions for each particular modeling exercise is fundamental to avoid unnecessary complexities. As a result, burdening of the model by multiple parameterizations can be reduced through prior simplification of its degrees of freedom but preserving spatiotemporal structures of hydrologic response. Further reduction in computational demand is attained in a continuous forecasting environment, where distributed models do not require calibration of its initial condition since tracking of vadose and saturated zones is maintained in time.

In the forecasting chain, uncertainties are usually supplied by several sources including the rainfall estimates and forecasts but also by hydrologic models through their difficulty in representing watershed conditions, a challenging task in mountain basins (Zappa et al. 2010). When radar data are used for short term predictions, QPE using reflectivity observations have been found to introduce significant amount of uncertainty (Habib et al. 2008; Schroter et al. 2011). Some of the reasons that produce those uncertainties include both technical

and atmospheric difficulties such as the radar bean attenuation, anomalous propagation, beam blockage, ground clutter, hail contamination, spurious returns and the inappropriate use of a reflectivity-rainfall relation. The last has been found to be crucial in obtaining correct representation of the rainfall fields (Pessoa et al. 1993; Baek and Smith 1998; Habib et al. 2008). On the other hand, QPF might carry additional uncertainties as they are based on readily available QPE and the correlation structures between QPF and QPE turn weak for large lead times. Further sources of uncertainty in hydrologic modeling are provided by the model structure, model parameter values, and initial condition. Quantification of hydrologic uncertainty and partitioning of its components remain a challenging task. Model structural uncertainties, for example, can not be easily distinguished from parameter and initial condition errors, unless another calibrated model is available at the moment of an intercomparison exercise. Finally, further limitations in ground data availability (e.g. rain and stream gauges), that are commonly few and sparse in areas of evident complexity, impose serious constraints in terms of the calibration and validation of actual precipitation fields and hydrologic responses. Thus, lack of good quality ground information can result in decreased hydrologic performance.

The Front Region in Colorado is an ideal setting to study the origin and development of flood events due to the availability of hydro-meteorological information, the sampling of a broad range of landscape characteristics and the presence of convective storm events during the summer season. In the past, this region has experienced several major flash floods causing fatalities and losses

over 4 billion dollars present money (Petersen et al. 1999; Chen et al. 2001). The presence of recurrent flooding events in these complex environments encourage the coupling of precipitation predictions to distributed hydrologic forecasts. The Triangulated Irregular Network (TIN)-based Real-time Integrated Basin Simulator (tRIBS) is adopted as a hydrologic verification tool. The model explicitly accounts for spatial variations in topography, land surface characteristics and channel network structure, as well as spatiotemporal meteorological forcing (Ivanov et al. 2004; Vivoni et al. 2007a).

The work developed here intends to fill voids in the present and future of operational flood forecasting chain when both QPEs and QPFs are fully utilized, accounting for the introduced uncertainties and their propagation from the rainfall estimation to the simulated hydrological response. In the following paragraphs a brief description of the dissertation chapters is provided.

OUTLINE OF CHAPTERS 2-5

Chapter 2 provides an initial examination to the value of current high resolution QPEs (hourly, 4-km) in four study basins of the CFR using a calibrated distributed hydrologic model as verification tool. Improvements in flood predictions are expected as the quality of radar, multisensor and satellite observations improves. To evaluate QPE skill, we compare the precipitation properties at the site (i.e., rain gauge location), basin-average and regional scales and evaluate their influence on the simulated basin response, including the outlet discharge, runoff mechanisms and seasonal water balance. We also analyze the value of gridded QPEs with respect to uniform forcing derived from rain gauges.

We find that radar and multisensor QPEs lead to improved hydrologic model performance compared to simulations driven with rain gauge data only with respect to the observed streamflow. Satellite QPEs exhibit lower overall streamflow simulation skill compared with estimates derived from radar-based QPEs, but are preferable to assuming uniform forcing from nearby rain gauges in the mountain settings studied here. One demonstration of this is the fact that satellite QPEs preserve the fundamental properties of the basin response, including a simple scaling relation between the relative spatial variability of runoff and its magnitude. As a result, satellite QPE products open new avenues for forecasting in regions with limited access and sparse observations.

In chapter 3, we outline the importance of using an appropriate *Z-R* relation that translates radar reflectivity into rainfall intensities, prior to developing regional QPF intended to be used in distributed hydrologic models to predict floods and flash floods. Nonetheless, uncertainty remains in the use of the reflectivity-rainfall (*Z-R*) relation, in particular for mountainous regions where ground validation stations are often lacking, land surface datasets are inaccurate and the spatial variability in many features is high. We assess the propagation of rainfall errors introduced by different *Z-R* relations on distributed hydrologic model performance for four mountain basins in the Colorado Front Range. To do so, we compare spatially-integrated and distributed rainfall and runoff metrics at seasonal and event time scales during the warm season when convective storms dominate. Results reveal that the basin simulations are quite sensitive to the uncertainties introduced by the *Z-R* relation in terms of streamflow, runoff

mechanisms and the water balance components. The propagation of rainfall errors into basin responses follow power law relationships that link streamflow uncertainty to the precipitation errors and streamflow magnitude. Overall, different *Z-R* relations preserve the spatial distribution of rainfall relative to a reference case, but not the precipitation magnitude, thus leading to large changes in streamflow amounts and runoff spatial patterns at seasonal and event scales. Furthermore, streamflow errors from the *Z-R* relation follow a typical pattern that varies with catchment scale where higher uncertainties exist for intermediate-sized basins. The relatively high error values introduced by two operational *Z-R* relations (WSR-57 and NEXRAD) in terms of the streamflow response indicate that site-specific *Z-R* relations are desirable in this complex terrain region, particularly in light of other uncertainties in the modeling process, such as model parameter values and initial conditions.

Chapter 4 is dedicated to investigate the predictability characteristics of floods and flash floods using quantitative precipitation forecasts from radar nowcasts when used for distributed hydrologic predictions, at eleven mountain watersheds undergoing warm-season precipitation. The effects of lead time, rainfall distribution and basin area on the flood forecasting skill are quantified by means of regional grid-to-grid verification analysis, hydrologic integrated and distributed responses and the identification of typical patterns in the predictability and error dispersion functions during two significant Storms in 2004 and 2006. We find that flood forecasting skill decreases with lead time but functional relationships depend on the interactions between watershed properties (soils,

topography, and vegetation) and rainfall characteristics. Across the majority of basins, flood forecasting skill reduces noticeably for lead times greater than 30 minutes. Error structures introduced by rainfall magnitude and spatial distribution characteristics propagate into streamflow forecast uncertainties in a manner that is controlled by changes in local runoff production that find their most critical point at intermediate-sized scales. The effect of model parameter uncertainties during an independent validation is tested and found to be significant (on the same order of magnitude) when compared to the hydrologic uncertainties introduced by forecasted rainfall.

Chapter 5 presents general conclusions of the preceding chapters and provides insight into future directions. Chapters 2-4 correspond to either published, submitted or in preparation articles whose titles and authors appear below:

Chapter 2: Moreno, H.A., Vivoni, E.R., Gochis, D., 2012a. Utility of quantitative precipitation estimates for high resolution hydrologic forecasts in mountain watersheds of the Colorado Front Range. *J. Hydrol.* 438-439, 66-83.

Chapter 3: Moreno, H.A., Vivoni, E.R., Gochis, D.J., 2012b. Propagation of errors from the reflectivity-rainfall relation into simulated streamflows in mountain watersheds during summer convection. *Hydrol Process.*, (revisions after submission).

Chapter 4: Moreno, H.A., Vivoni, E.R., Gochis, D.J., 2012c. Spatiotemporal limits to flood forecasting in mountain catchments under summer

convection using radar nowcasting and a distributed hydrologic model. *J. Hydrometeorol.,* (in preparation).

The unifying theme of the dissertation circumscribes to distributed hydrologic modeling for flood forecasting during summer convection in mountain regions. The thesis expands the current body of knowledge with the following novelties: (1) A methodology to evaluate different QPE in multiple mountain basins by using both direct comparisons with rain gauges and hydrologic verifications through observed streamflows. (2) A procedure for deriving the reflectivity rainfall relation from ground rain gauges and its verification through hydrologic measurements in multiple catchments. This encourages the testing of the radar-rainfall conversion expressions before use into the operational forecasting chain. (3) The use of radar nowcasting techniques coupled to a distributed hydrologic model to explore the boundaries of flood forecasting prediction in multiple catchments. Results discussed in this thesis remark the need for the use of distributed forcing in distributed models for flash flood warning procedures. This promising alternative provides computationally efficient and accurate forecasts of the spatio-temporal structures of rainfall and runoff in areas where watershed and rainfall complexities challenge the power of current prediction systems.

Chapter 2

UTILITY OF QUANTITATIVE PRECIPITATION ESTIMATES FOR HIGH RESOLUTION HYDROLOGIC FORECASTS IN MOUNTAIN WATERSHEDS OF THE COLORADO FRONT RANGE

INTRODUCTION

Evaluations of Quantitative Precipitation Estimates (QPEs) from weather radar or satellite retrievals are typically performed through comparisons to rain gauges at individual sites or over regional scales. Despite progress in the development and use of remotely-sensed QPE products in complex terrain regions, significant uncertainties still exist (e.g., Zangl et al. 2008; Germann et al. 2009). One promising alternative for QPE evaluation in mountain settings is through the use of calibrated hydrologic models as verification tools (e.g., Gourley and Vieux 2005; Vivoni et al. 2007b). The appeal of hydrologic verification lies in the relative availability of streamflow data in mountain regions which are collected for flash flood alerts and water supply estimates. The spatially and temporally integrating characteristics of watersheds serve to organize or 'filter' precipitation events from a measurement perspective. Both real watersheds and distributed model representations of these are thus sensitive to the timing, intensity and geographic details of the precipitation forcing (e.g., Carpenter and Georgakakos 2004; Vivoni et al. 2006; Collier 2007).

Most QPE products have origins in radar reflectivity, infrared and passive microwave satellite data, and multisensor algorithms combining these sources. Historically, rain gauges have been the primary data source, but these only

provide a point measurement of a distributed input. Weather radars offer a high spatial coverage and resolution, but include a variety of errors, (e.g., beam attenuation, mixed-phase hydrometeor effects, terrain blockage), especially during warm-season convection in mountainous areas (Delrieu et al. 2000; Grassotti et al. 2003; Lee and Zawaski 2005; Morin et al. 2005; Habib et al. 2008). Satellite-based estimates are a complementary approach, but have weaker relations between the observed radiances and rainfall rates (Scofield and Kuligowski 2003; Sapiano and Arkin 2009; Gochis et al. 2009; Yucel et al. 2011). Multisensor estimates combine data sources through numerical or heuristic algorithms (Fulton et al. 1998; Seo et al. 1999; Young et al. 2000; Xie et al. 2005). Despite their promise, the underlying accuracy is tied to the properties of each product, inter-platform consistency and the particular algorithm used (Wang et al. 2008). Thus, inherent shortcomings of different QPE products will directly influence the rainfall errors in mountainous landscapes where substantial rainfall variability is present (Menabde et al. 1996; Kang and Ramirez 2007; Zangl et al. 2008).

Previous studies have evaluated QPE products with respect to rain gauges and hydrologic data at the basin scale. For example, Gourley and Vieux (2005) found that modeled streamflows using rain gauge data did not provide sufficient coverage for an accurate hydrologic simulation. Clearly, the use of sparse rainfall data may lead to significant differences in runoff production and the integrated basin response as compared to spatially-varying products (e.g., Yilmaz et al. 2005). To alleviate this issue, rain gauges have been used to correct biases in distributed QPEs from other platforms, yielding improved simulations (Fulton et

al. 1998; Gourley and Vieux 2005; Tobin and Bennett 2009). These results have shown that hydrologic models also help to elucidate the mechanisms through which a watershed responds to each type of QPE forcing.

Questions remain with respect to the use of hydrologic models as tools for QPE verification. Prior studies have focused on areas with high rain gauge coverage relative to the storm spatial scale. Can hydrologic models be used to verify QPEs in sparsely-gauged, mountain areas? How do errors from different QPEs propagate to the simulated basin response? What is the value of satellite-based products in distributed hydrologic models relative to mountain rain gauges? To address these questions, we selected the Colorado Front Range (CFR) in Colorado, USA, due to its physiographic complexities, warm-season convective storms and their associated flood and flash flood hazards, and the presence of reasonably high quality NEXRAD radar data coverage. We compare ten high-resolution (4-km, hourly) QPEs in four mountain basins ranging from 35 to 350 km^2 in area during the 2004 summer season that was coincident with the North American Monsoon Experiment (NAME; Higgins and Gochis 2007).

To evaluate the QPE products, we analyze the spatiotemporal variability in precipitation at the local, basin and regional scales, and compare these to available rain gauges using several statistical metrics. Subsequently, we assess the QPE products through hydrological verification using a distributed hydrologic model, the Triangulated Irregular Network (TIN)-based Real-time Integrated Basin Simulator (tRIBS), at each watershed. The model explicitly accounts for spatial variations in watershed characteristics and meteorological forcing as well

as represents the hydrological dynamics at internal locations (Ivanov et al. 2004; Vivoni et al. 2007a).

METHODS

Study Area and Watersheds

The CFR is characterized by varied topography, vegetation, soils, and convective storms during the summer. Several major flash floods have taken place in the region. For example, an event on 28 July 1997 at Spring Creek in Fort Collins, CO, caused five fatalities and losses over 200 million dollars (Petersen et al. 1999). Thus, societal impacts associated with floods provide a compelling motivation for improving hydrologic forecasts. We delineated eleven basins in the CFR region upstream of stream gauging stations operated by the Colorado Division of Water Resources (CDWR; Figure 2.1). Four of these were selected for hydrologic verification: Buckhorn Creek (BUCK, 350 km^2), Fish Creek (FISH, 41 km^2), Ralston Creek (RALS, 117 km^2) and South Saint Vrain River (SVRAIN, 35 km^2). This selection was based on the availability of rain gauge data, and the sampling of a range of landscape properties along a north-to-south gradient. Figure 2.2 shows the distributions of vegetation, soils, elevation and hydrography in each basin. Hourly weather stations recording wind speed, pressure, and air and dew point temperatures are also collocated with the four rain gauges. As in other applications, the extrapolation of station data over the basins likely contributes to uncertainty in the meteorological forcing.

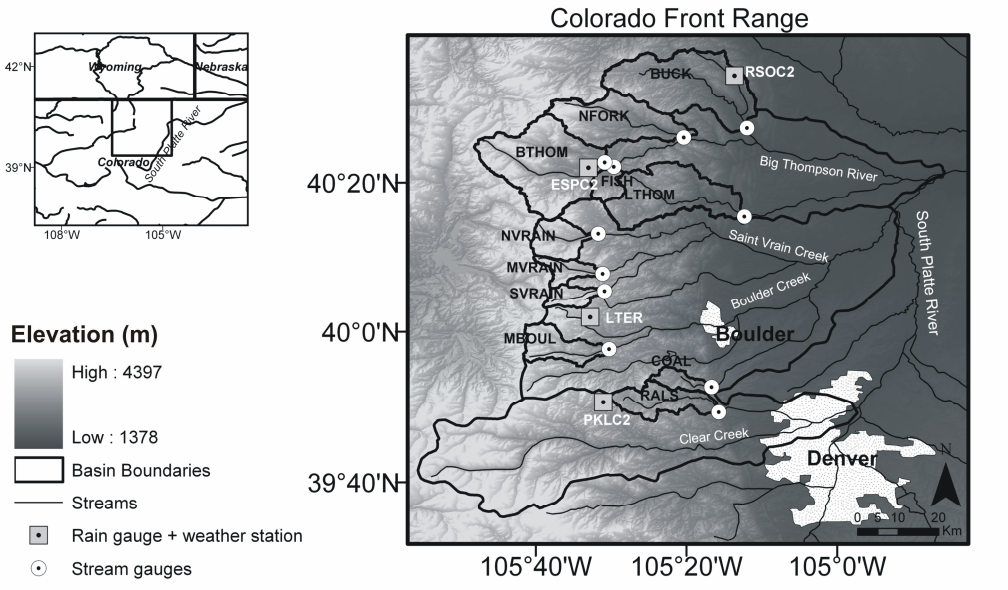

Figure 2.1. Colorado Front Range (CFR) location, elevation distribution and boundaries of eleven study watersheds. Four basins are selected for this study: Buckhorn Creek (BUCK), Fish Creek (FISH), South Saint Vrain Creek (SVRAIN) and Ralston Creek (RALS). Four hourly rain gauge and weather stations are shown: RSOC2, ESPC2, LTER and PKLC2.

The set of mountain catchments are characterized by pronounced elevation gradients with generally east-facing aspects, narrow valleys, and dendritic channel networks. There is a prevalence of sandy loam, loam and exposed bedrock as the main soil types, and forests and grasslands as the dominant land cover. Table 2.1 summarizes the major characteristics of the four basins.

Quantitative Precipitation Estimates

We compiled rain gauge, weather radar, satellite and multisensor rainfall estimates from multiple sources.

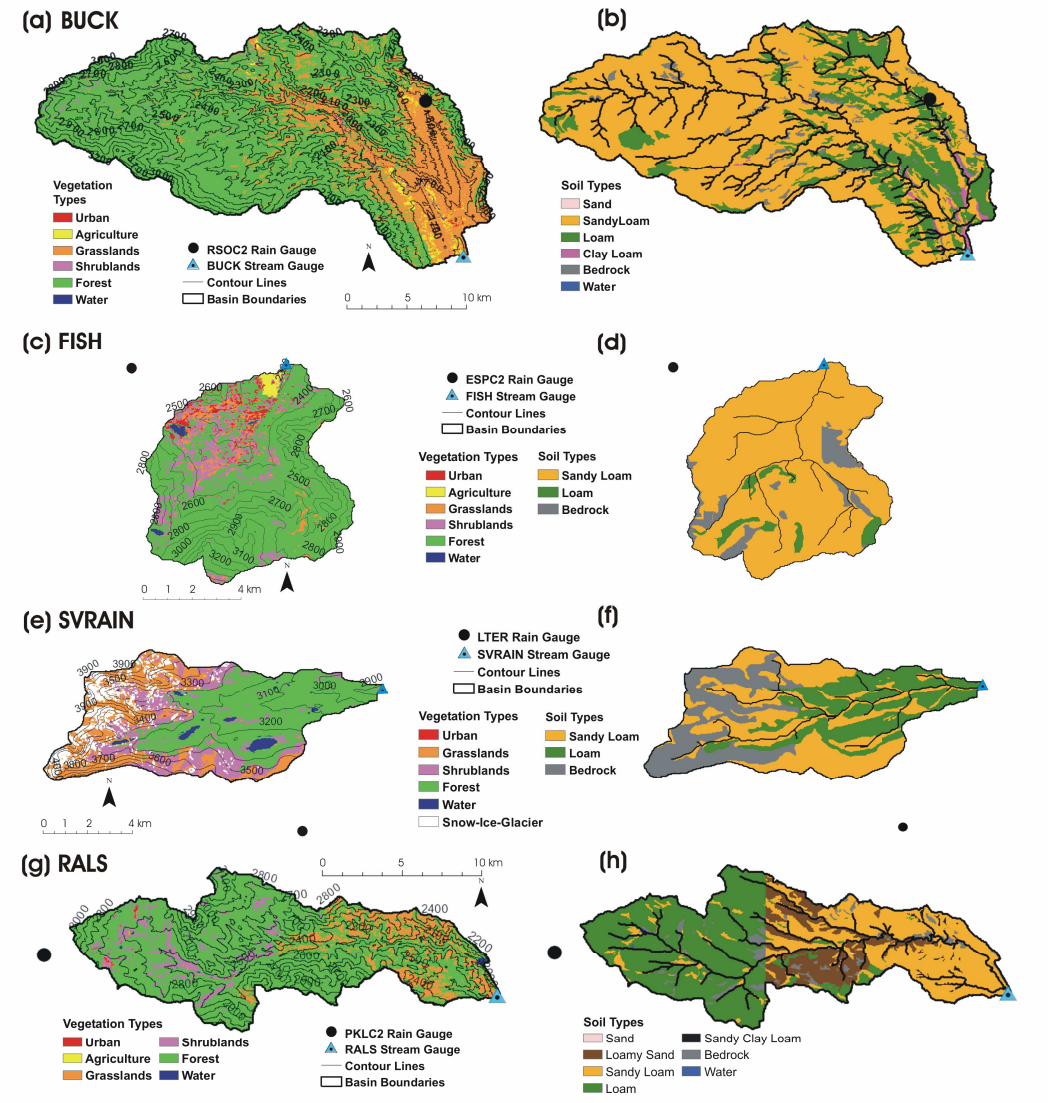

Figure 2.2. Spatial distributions of elevation contours, hydrography, vegetation and soil classes in the four study basins. Rain gauge, weather and stream gauge stations are also shown.

Table 2.2 presents the characteristics and sources of the precipitation datasets, which include ten QPE products (Level II, Stage III, Stage IV, A-E, H-E, H-Erad, GMSRA1, GMSRA2, Blend, PERSIANN) and four rain gauges (RSOC2, ESPC2, LTER, PKLC2). These were selected based on data availability in summer 2004 and a reasonably high spatiotemporal resolution (4-km, 1-hr).

Table 2.1 Topographic, soil and vegetation characteristics of the study watersheds.

Property	Buckhorn Creek	Fish Creek	South Saint Vrain Creek	Ralston Creek
ID	BUCK	FISH	SVRAIN	RALS
Stream Gauge ID	BUCRMVCO	FISHESCO	SSVWARCO	RALCRKCO
Rain Gauge Name	RSOC2	ESPC2	LTER	PKLC2
Total Area [km^2]	350.5	40.8	35.1	117.3
Length of main channel [km]	45.6	9.7	12.6	25.8
Slope of main channel [m/km]	26.2	70.5	42.3	32.1
Mean elevation [m]	2418	2858	3455	2517
Minimum/maximum elevations [m]	1583/3268	2284/3473	2858/4087	1847/3204
Std. Elevation [m]	482	333	344	387
Mean slope [%]	28.0	28.2	30.0	29.2
Std. Slope [%]	16.3	19.9	26.7	17.9
Major soil class 1 (% area)	Sandy loam (74.6)	Sandy loam (86.7)	Sandy loam (44.1)	Loam (45.5)
Major soil class 2 (% area)	Loam (21.2)	Bedrock (6.9)	Loam (30.6)	Sandy Loam (34.4)
Major soil class 3 (% area)	Bedrock (3.1)	Loam (4.6)	Bedrock (25.2)	Loamy sand (13.0)
Major vegetation class 1 (% area)	Forest (70.4)	Forest (76.2)	Forest (43.1)	Forest (77.8)
Major vegetation class 2 (% area)	Grassland (27)	Shrubland (13.8)	Grassland (22)	Grassland (14.6)
Major vegetation class 3 (% area)	Agriculture (1.4)	Grassland (5.1)	Shrubland (19.4)	Shrubland (7.1)

For PERSIANN, rainfall depths were aggregated in time from 30-min to 1-hr intervals. Data gaps of hourly rain gauge data from May through September (MJJAS) accounted for less than 3% of the period in all cases. Neighboring hourly stations were used to estimate missing data. Radar reflectivity data was obtained from a mosaic of the WSR-88D Level II 'NEXRAD' radars at Denver, CO (KFTG), Pueblo, CO (KPUX) and Cheyenne, WY (KCYS) over minimum and maximum volume scan altitudes of 3-km and 6-km, respectively.

Table 2.2 Summary of main characteristics of rain gauge, radar, satellite and multisensor QPEs.

Data Set	Type	Full Name	Brief description	References
RSOC2, ESPC2, LTER, PKLC2	Rain gauge	Redstone, Estes Park, Long Term Ecological Research Site at Niwot Peak, Pickle Gulch	Hourly rain gauges from Mesowest and AMERIFLUX networks	Steenburgh 2003; Horel et al. 2002; Lazarus et al. 2002.
Level II	Radar	NWS WSR-88D Level II at 1-km and 4-km	NWS Doppler Radar Network	Kelleher et al. 2007.
Stage III	Multisensor	Multisensor Precipitation Estimator NEXRAD Stage III	Mosaicked radar scans and mean field bias adjustment.	Young et al. 2000; Xie et al. 2005; Wang et al. 2008.
Stage IV	Multisensor	Multisensor Precipitation Estimator NEXRAD Stage IV	National mosaicked product from hourly multisensor precipitation.	Fulton et al. 1998; Mitchell et al. 2004.
A-E	Satellite	Auto-Estimator	Brightness temperatures from GOES Infrared (IR). Radar screening of no-rain pixels.	Vicente et al. 1998, 2002.
H-E, H-Erad	Satellite	Hydro-Estimator Hydro-Estimator with radar screening	Brightness temperatures from GOES IR modulated by cloud evolution, stability, atmospheric moisture. Radar and local topography used to adjust rates.	Scofield and Kuligoswki 2003.
GMSRA1, GMSRA2	Satellite	GOES Multispectral Rainfall Algorithms V1, V2	Combined information from visible, near-IR and IR measurements with two different algorithms for analyzing brightness temperatures for day and night time.	Ba and Gruber 2001.
Blend	Satellite	Naval Research Laboratory Blended Technique	Histogram-matching calibration of IR to merged microwave.	Turk and Miller 2005.
PERSIANN	Satellite	Precipitation Estimation From Remotely Sensed Information using Artificial Neural Networks	Adaptive Neural Network calibration of GOESS and TRMM using a cloud classification system.	Hong et al. 2004; Hong et al. 2007.

Reflectivity values were transformed to 5-min, 1-km resolution rainfall rates by applying a *Z-R* relation and accumulating to hourly depths (i.e., Level II 1-km product). The rainfall-reflectivity coefficient and exponent, $Z = 700R^{1.3}$, were obtained from a multi-criteria optimization method that minimized the Root Mean Square Error (RMSE) and maximized the Critical Success Index (CSI) between the observed time series at seven hourly rain gauges and the radar estimates at collocated pixels (Moreno et al. 2012b). The Level II 1-km product was aggregated to 4-km resolution for comparison to satellite QPEs, which include several algorithms that derive rainfall rates from infrared cloud top temperature and were resampled to 4-km, hourly resolution (Table 2.2). Two of the products (Stage III, Stage IV) are classified as multisensor precipitation estimates.

Distributed Hydrologic Modeling

Model Overview

In this study, we apply tRIBS for continuous flood forecasting using precipitation from multiple sources. Prior studies have demonstrated effective use of the model for flood forecasting in basins with different characteristics (Ivanov et al. 2004; Vivoni et al. 2007b; Mascaro et al. 2010), including mountain areas (Mahmood and Vivoni 2008; Vivoni et al. 2009; Nikolopoulus et al. 2011). The model accounts for spatial heterogeneities in terrain, vegetation and soil properties, and atmospheric forcing to reproduce the space-time hydrologic evolution of a basin. Simulations of the coupled surface-subsurface response are performed by tracking infiltration fronts, water table fluctuations and lateral

moisture fluxes. Surface runoff is triggered through infiltration-excess, saturation-excess, perched return flow and groundwater exfiltration mechanisms, while routing is performed through hydrologic overland flow and hydraulic channel routing. Evapotranspiration consists of soil evaporation, plant transpiration and evaporation of intercepted rainfall. An important model characteristic is the use of a TIN to represent a basin and reduce the number of computational nodes relative to the original data with minimal loss of information (Vivoni et al. 2004). Computational time savings in this study are further achieved through a parallel computing approach based on sub-basin partitioning and the use of a high performance computing (HPC) platform. The model processes, computational framework and parallelization capabilities are given in full detail in Ivanov et al. (2004) and Vivoni et al. (2011).

Model Parameters

As a distributed-parameter model, tRIBS requires spatially-varying input fields including topography, soils, vegetation, and aquifer characteristics. We obtained a 30-m Digital Elevation Model (DEM) from the National Elevation Dataset (Gesch et al. 2002) for the CFR region. Watershed delineation was based on creating depressionless DEMs, deriving the overland flow directions along the steepest paths, and computing the upslope areas at each outlet. Channel networks were delineated from constant-area thresholds used to classify DEM points as stream cells (e.g., O'Callaghan and Mark 1984; Tarboton et al. 1991). For each study basin, a TIN was generated by minimizing the number of computational nodes and the Root Mean Squared Error (RMSE) relative to the original DEM

following the methods of Vivoni et al. (2004). This resulted in an optimum horizontal point density (d = n_t/n_g, where n_t is the number of TIN nodes and n_g is the number of DEM cells) of: BUCK (d = 0.47, n_t = 122,050 nodes), FISH (d = 0.27, n_t = 22,231 nodes), SVRAIN (d = 0.46, n_t = 19,672 nodes), and RALS (d = 0.43, n_t = 52,231 nodes). As shown by Vivoni et al. (2004), the TINs preserve terrain characteristics, the channel network structure and the basin boundary. Voronoi polygons are constructed from the derived TINs and used as the finite-volume domain for mass balance and flux computations.

Soil texture maps were derived from the Soil Survey Geographic (SSURGO) database at 1:24,000 scale, with gaps filled by the State Soil Geographic (STATSGO) database at a scale of 1:250,000. Most soils in the CFR region are sandy loam, loam and exposed bedrock. Table 2.1 and Figure 2.2 provide details on the major soil classes for each study basin. Soil texture is used in tRIBS to derive the soil parameters listed in Table 2.3, including soil hydraulic and thermal properties. As an example, feasible ranges of reference (or uncalibrated) soil parameter values are provided for sandy loam in Table 2.3. Hydraulic characteristics of the underlying aquifer are described by the depth variation of soil properties, particularly through the ratio of horizontal to vertical hydraulic conductivities (anisotropies, A_r), the hydraulic conductivity decay parameter (f) and the depth to bedrock (B). To avoid model overparameterization, soil classes such as unweathered and weathered bedrock and stones were grouped into a single class. Similarly, soils classified as slightly decomposed plant material were grouped into the dominant sandy loam class.

Table 2.3 Soil (*), vegetation (+), routing (%) and aquifer (^) parameters in the tRIBS model with minimum, reference and maximum values for sandy loam and forest classes.

Parameter	Units	Symbol	Min.	Ref.	Max.
Sat. hydraulic conductivity*	[mm/h]	K_s	0.36	10.9	36
Soil moisture at saturation*	[-]	θ_s	0.271	0.412	0.608
Residual soil moisture*	[-]	θ_r	0.024	0.041	0.106
Pore size distribution index*	[-]	λ_0	0.14	0.378	2.0
Air entry bubbling pressure*	[mm]	ψ_b	-454.7	-146.6	0
Conductivity exponent decay*	[-]	f	0.00035	0.008758	0.05
Sat. and unsat. anisotropy ratios*	[-]	a_r	1	223	1000
Porosity*	[-]	n	0.351	0.453	0.611
Thermal conductivity*	$[Jm^{-1}s^{-1}K^{-1}]$	k_s	0.825	1.65	2.475
Volumetric heat capacity*	$[Jm^{-3}K^{-1}]$	C_s	1360715	2721430	4082145
Free throughfall coefficient+	[-]	p	0.15	0.25	0.65
Canopy field capacity+	[mm]	S	0.525	1.05	1.575
Canopy drainage rate coefficient+	[-]	K	0.1	0.12	0.25
Canopy drainage rate exponent+	[-]	$b2$	3.2	3.7	4.3
Albedo+	[-]	a	0.102	0.205	0.307
Vegetation height+	[m]	H_v	14	20	35
Optical transmission coefficient+	[-]	K_t	0.15	0.3	0.45
Canopy ave. stomatal resistance+	[s/m]	r_s	87.5	175	262.5
Vegetation fraction+	[-]	V	0.5	0.7	0.8
Manning coefficient%	[-]	n_e	0.03	0.04	0.07
Kinematic routing velocity coeff.%	[-]	C_v	12.5	25	37
Non-linear discharge exponent%	[-]	r	0.2	0.4	0.45
Channel width coefficient%	[-]	a_B	0.568	1.1357	1.7036
Channel width exponent%	[-]	b_B	0.2273	0.4546	0.6819
Bedrock depth^	[m]	B	0.25	2	3

In a similar fashion, vegetation maps were obtained from the USGS National Land Cover Dataset (Homer et al. 2004). Dominant vegetation types in the basins are forests and grasslands, followed by smaller fractions of glaciated

terrains, agricultural and urban areas (see Table 2.1 and Figure 2.2 for details). Both deciduous and evergreen forests were grouped into a single forest class. Vegetation types are used in the model to derive rainfall interception and evapotranspiration parameters. As an example, Table 2.3 presents reference vegetation parameter values for a forest cover. Soil and vegetation classes are mapped directly to Voronoi polygons (Ivanov et al. 2004) and are associated with an attribute table with the corresponding parameters used in the energy and mass continuity equations. To avoid the potential for model overparameterization, parameter values are not allowed to vary within soil and vegetation classes, only between classes.

Model parameterization also includes aquifer and routing properties. A range of spatially-uniform bedrock depths in the different basins was inferred from seven soil catenas constructed by Birkeland et al. (2003) along a transect in the CFR. Parental rocks are broadly uniform with high contents of feldspar, quartz, biotite and hornblende. The mean depth to bedrock determines the aquifer thickness and thereby the amount of water that can be stored and moved through the subsurface (Ivanov et al. 2004). Routing parameters control runoff through hillslope flow paths and the stream network. Channel roughness and hillslope routing parameters were obtained from prior studies (Chow 1959; Ivanov et al. 2004), while a geomorphic relation between channel width (w in m) and contributing area (A in km^2) was derived from field measurements taken by the CDWR from 2003 through 2008 at the eleven basins shown in Figure 2.1,

resulting in $w = 1.14A^{0.45}$ (http://www.dwr.state.co.us). Table 2.3 reports a set of reference routing parameters.

Model Initialization

As in most surface-subsurface models, tRIBS requires an initial condition determined by the spatial distribution of soil water content. Lacking direct observations, the initial soil moisture can be inferred from the depth to groundwater table due to the assumption of hydrostatic equilibrium (Ivanov et al. 2004). Following Vivoni et al. (2007a), we conducted a drainage experiment for each basin to derive a rating curve linking simulated basin outlet discharges (Q_b) to model-based estimates of the spatial mean depth to groundwater (N_{wt}). The experiments start with a fully-saturated basin that is allowed to drain for a long period (~10 years) without any weather forcing, leading to hydrographs that are controlled by geomorphology, channel geometry and soil properties (e.g., Vivoni et al. 2008). A maximum expected depth to bedrock of 3 m was used to provide a wide range of initialization cases. Feasible scenarios (10 per basin from dry to wet) for the initial N_{wt} were extracted from the rating curve through the simulated Q_b that correspond to percentiles of the exceedence probability of the observed discharge at each stream gauge for summers 2003 to 2006. Using the exceedence probability of observed discharge provides realistic streamflow values that are uniquely related to spatially distributed groundwater depths. Figure 2.3a illustrates the groundwater rating curves for the four basins.

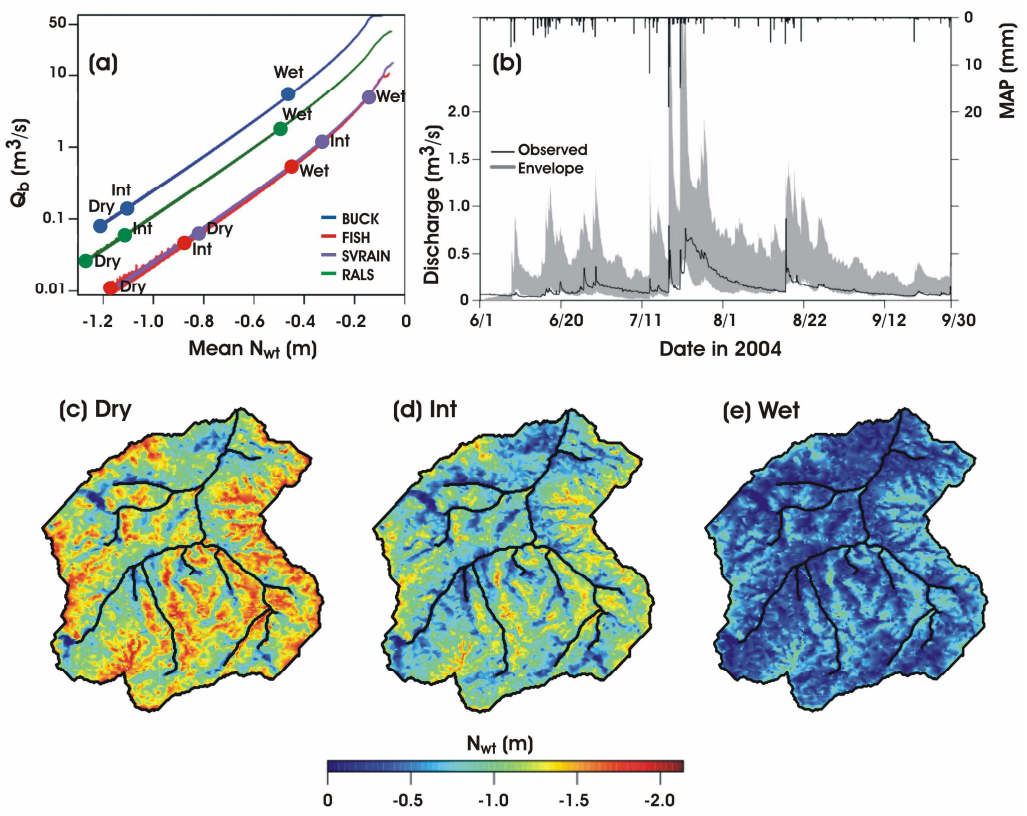

Figure 2.3. Selection of initial condition for calibration of hydrologic model. (a) Discharge rating curves from drainage experiments at BUCK, FISH, SVRAIN and RALS. Symbols illustrate the dry, intermediate and wet cases derived from percentiles from historic flow duration curves. N_{wt} is the mean groundwater table depth below the surface, and Q_b is outlet baseflow discharge. (b) Observed (solid line) and uncertainty envelope (shaded area) of the simulated hydrographs at FISH along with the mean areal precipitation (MAP). Spatial distribution of the initial depth to groundwater as dictated by the (c) dry, (d) intermediate and (e) wet cases for FISH.

Percentiles at 0.05, 50 and 99.5% are shown to represent three possible initial scenarios: dry, intermediate and wet. For FISH, these initial Q_b states correspond to maps of groundwater depth shown in Figure 2.3c-e. Based on the sampling of the initial conditions, we conducted preliminary runs for FISH using reference (uncalibrated) parameter values (Table 2.3) for uniform sandy loam soils, and found the uncertainty envelope in Figure 2.3b.The wide spread in the

discharge indicates that the initialization should be considered in the calibration approach, as described in the following. As we excluded snow processes in the simulations (Rinehart et al. 2008), their impact on streamflow in SVRAIN was handled by a higher basin water storage in the selected initial condition. Thus, the aquifer is expected to slowly release water in a fashion that mimics the summer snowmelt contribution.

Calibration Strategy

Identifying a set of reasonable initial conditions and parameter values in the CFR basins is challenging due to the complex hydrologic processes in the region. Our approach combines the advantages of manual and automatic procedures by first evaluating the importance of each model parameter in a One-At-a-Time (OAT) sensitivity analysis, followed by an optimization method using the Shuffled Complex Evolution (SCE) algorithm (Duan et al. 1993). OAT analyses were carried out in FISH and RALS using spatially-uniform classes that represented dominant soil and vegetation types. These basins were selected to represent summer conditions without a major snowmelt component, as observed at SVRAIN, to reduce parameter dependence on the snowmelt period. Soil, vegetation and routing parameters were varied within ranges found in the literature (Chow 1959; Bear 1972; Rutter et al. 1977; Rawls et al. 1982; Shuttleworth 1988; Birkeland et al. 2003; Ivanov et al. 2004; Mitchell et al. 2004; Todd and Mays 2005), although estimated guesses from preliminary model runs were incorporated to improve those ranges when a limited number of values were available from other studies (e.g., conductivity decay exponent). OAT results

indicated that the outlet streamflow response was controlled by: air entry bubbling pressure (ψ_b), non-linear hillslope discharge exponent (r), pore size distribution index (λ_0), soil moisture at saturation (θ_s), hydraulic conductivity decay (f), saturated hydraulic conductivity (K_s) and depth to bedrock (B). These results are considered relevant for all study basins during the summer season, but might vary for other locations, time periods or target observations. The seven parameters resulting from the OAT analysis were subsequently used for model calibration.

Based on the selected model parameters and initial conditions, the SCE method was used to minimize the RMSE between the observed and simulated hydrographs. Initial groundwater distributions from the drainage experiments were included in the automated optimization. The parameters identified in the OAT analyses and the initial conditions constituted the search space for the optimization routine. The SCE algorithm combines the features of multiple complex shuffling and competitive evolution, leading to an efficient exploration of the feasible parameter space. The model calibration was based on the hourly Level II 1-km product obtained from the *Z*-*R* relation derived using rain gauge measurements, as this constituted one of the best-available products in the region. Level II 1-km has the highest spatiotemporal resolution over CFR (5-min, 1-km) and was adjusted to replicate time series at seven rain gauges. Naturally, the Level II 1-km forcing itself may contain estimation errors due to issues of mountain beam blockage and hail contamination as well as uncertainties in the *Z*-*R* relation, among others. Comparisons between observed and simulated outlet streamflows may also vary due to uncertainties in the observations themselves. Minor gaps in

the observed streamflow at FISH (2% of the full record), SVRAIN (2.9%) and RALS (1.4%) were filled in using simple interpolation. Measured hydrographs are based on discharge-stage relations with potential estimation errors caused by channel geometry changes, overbank storage and unsteady flow (Herschy 1995).

Figure 2.4 presents the observed hydrographs and the simulations derived from the calibration exercise for each basin along with *RMSE* and Nash-Sutcliffe efficiency (*NS*) scores. A subset of model parameter values minimizing the *RMSE* between observed and simulated hydrographs are shown in Table 2.4 and correspond to the 'modeled' series. Note that the streamflow response varies considerably in time and among each basin, reflecting the nature of the meteorological forcing, landscape properties and the initial conditions. The distributed model is able to capture the different responses fairly well with *RMSE* ranging from 0.09 m^3/s to 0.66 m^3/s. Calibrated parameter values and initial water table depths presented in Table 2.4 are not the same across all basins but they fall within realistic ranges. Certainly, parameters provide degrees of freedom to compensate for model errors in a manner that differs for each basin. To consider the uncertainty introduced by the calibration process, Figure 2.4 also presents an envelope of the top 10% of the tested parameter sets in terms of *RMSE*. In most cases, the observed streamflow lies within the uncertainty envelope. Notice that the model is unable to reproduce the high baseflow in SVRAIN due to snowmelt, as verified from a Landsat image on June 2004 (not shown).

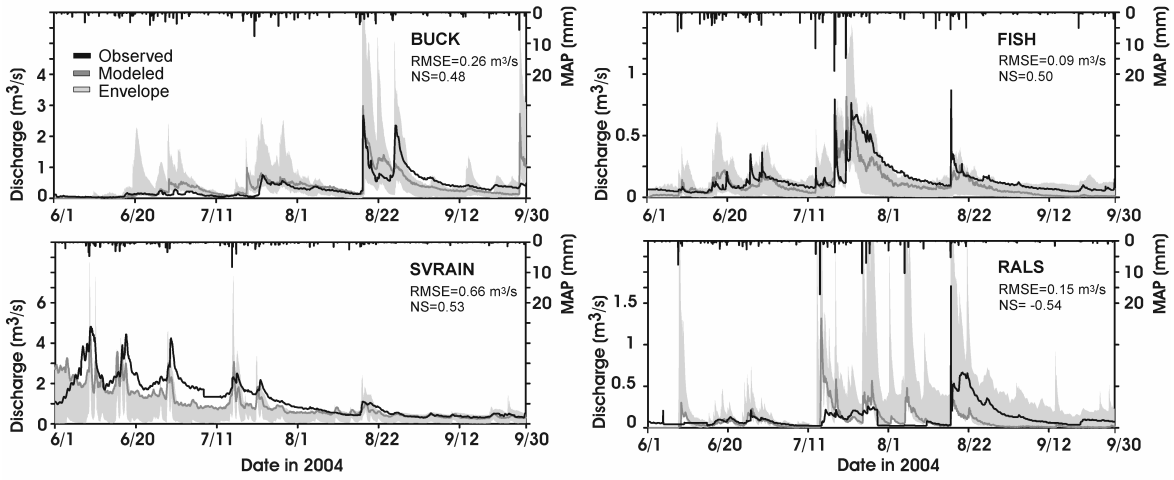

Figure 2.4. Observed (black lines) and simulated hydrographs (dark gray lines) resulting from model calibration in each basin, along with NS and RMSE skill scores. Mean areal precipitation (MAP) in each basin is derived from the hourly, 1-km Level II product. Uncertainty in parameter values and initial conditions is depicted by the light gray envelopes.

The remaining discrepancies can be explained by model structural error and the uncertainties introduced through precipitation forcing and streamflow data. Note that this effort considered each complex basin independently and calibrated the model for the entire summer based on forcing from small-scale convective precipitation systems (Yates et al. 2000; Ashley and Ashley 2008).

Parallel Model Experiments

Efficient fully-distributed modeling is achieved in this study through the use of a High Performance Computing (HPC) facility at Arizona State University. The parallel capabilities of tRIBS are based on a domain decomposition using a sub-basin partitioning of each watershed (Vivoni et al. 2011). Individual sub-basins are assigned to computer processors that exchange surface and subsurface fluxes along the channel network and across adjacent groundwater boundaries.

Table 2.4. Summary of calibrated parameter values and initial conditions. $\mu(N_{wt})$ is the mean depth to the groundwater table in each basin.

Parameter	BUCK		FISH		SVRAIN		RALS	
	Sandy loam	Loam	Sandy loam	Bedrock	Sandy loam	Loam	Loam	Sandy loam
K_s [mm/h]	7.96	30.29	17.18	2.04	8.16	22.38	25.76	18.64
θ_s [-]	0.32	0.37	0.35	0.07	0.57	0.56	0.52	0.58
λ_0 [-]	0.81	1.46	1.47	0.06	1.48	0.58	1.67	1.19
ψ_b [mm]	-244.22	-704.46	-84.36	-221.89	-21.71	-804.97	-385.37	-324.37
f [mm^{-1}]	0.033364	0.025288	0.00222	0.03063	0.000364	0.000956	0.036551	0.008452
r	0.4459		0.4491		0.4074		0.4340	
B [m]	1.26		1.05		2.84		1.66	
$\mu(N_{wt})$ [m]	1.17		1.01		0.169		1.28	

Domain partitioning is achieved by a connectivity table assigning each sub-basin to a processor. The connectivity table for each basin was generated through METIS (Karypis and Kumar 1999), a graph partitioning software that properly balances the computational workload. Parallel run times were significantly reduced, in average by a factor of five, which enhanced the capability to execute a larger number of model iterations for the calibration efforts and to test the multiple QPE products in each basin.

RESULTS AND DISCUSSION

Multi-scale Comparison of Quantitative Precipitation Estimates

The spatiotemporal distribution of warm-season precipitation derived from the different QPE products was analyzed with respect to the entire CFR region, at each rain gauge site and within the study basins. The spatial variability of total seasonal precipitation shown in Figure 2.5 is relevant for assessing the flood

potential in the region during 2004 (JJAS) and comparing the characteristics of the different QPE products. For this analysis, any temporal gaps for a particular QPE were filled in with rainfall estimates from the Level II product at hourly, 4-km resolution, whose time series is complete and which should, in general, impart a positive impact to the product skill evaluation given its gauge-calibrated nature. At the seasonal aggregation scale, a recognizable rainfall pattern in all QPE products was the presence of higher rainfall in the eastern portion of CFR at lower elevations. Furthermore, QPEs that incorporate weather radar estimates (Level II, Stage III, Stage IV) share common features, including a high spatial mean (μ) and standard deviation (σ). Certain areas in the Level II product have marked differences with Stage III and IV (north and southeast regions) due to corrections in the multisensor estimates not incorporated into the *Z-R* relation. Of the satellite QPE products, only A-E exhibits magnitudes and spatial patterns resembling the radar and multisensor products. Most satellite QPEs (H-E, H-Erad, GMSRA1, GMSRA2 and PERSIANN) show lower means and smoother spatial variations, except for Blend that has high rainfall amounts due to outliers in June. Additional analyses confirmed that Level II has the highest number of rainy hours, an indication of the presence of a larger number of small accumulation precipitation events. Seasonal comparisons over the CFR were complemented by inspecting hourly rainfall at each rain gauge site and their collocated pixel values from each QPE product.

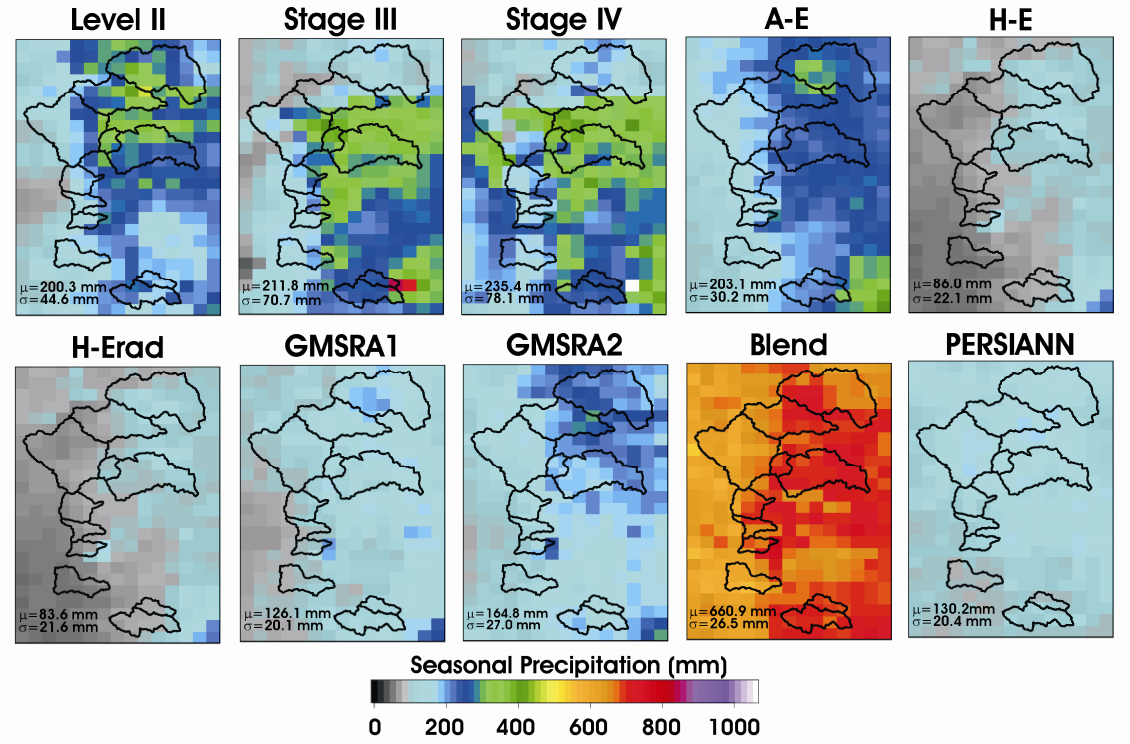

Figure 2.5. Spatial distribution of summer season (JJAS in mm) accumulated precipitation in 2004 in the CFR region from each hourly, 4-km QPE product. Watershed divides for 11 basins (Fig. 2.1) are depicted in black. Spatial mean and standard deviations are also shown.

Figure 2.6 presents an example for the LTER site and a subset of QPEs, while Table 2.5 provides statistical evaluations at all rain gauge sites and all QPEs. The comparisons reveal that Level II, Stage III, Stage IV and A-E provide the best estimates of the total rainfall (P_{tot}) and its temporal distribution at the rain gauge sites. In Figure 2.6, Level II 4-km shows a good performance that represents well the timing and magnitude of storms. This is in part due to the use of seven rain gauges in the calibration of the *Z-R* relation. For the LTER site, Stage III and Stage IV tend to underestimate rainfall, while the satellite QPEs exhibit weaker relations with rain gauge data.

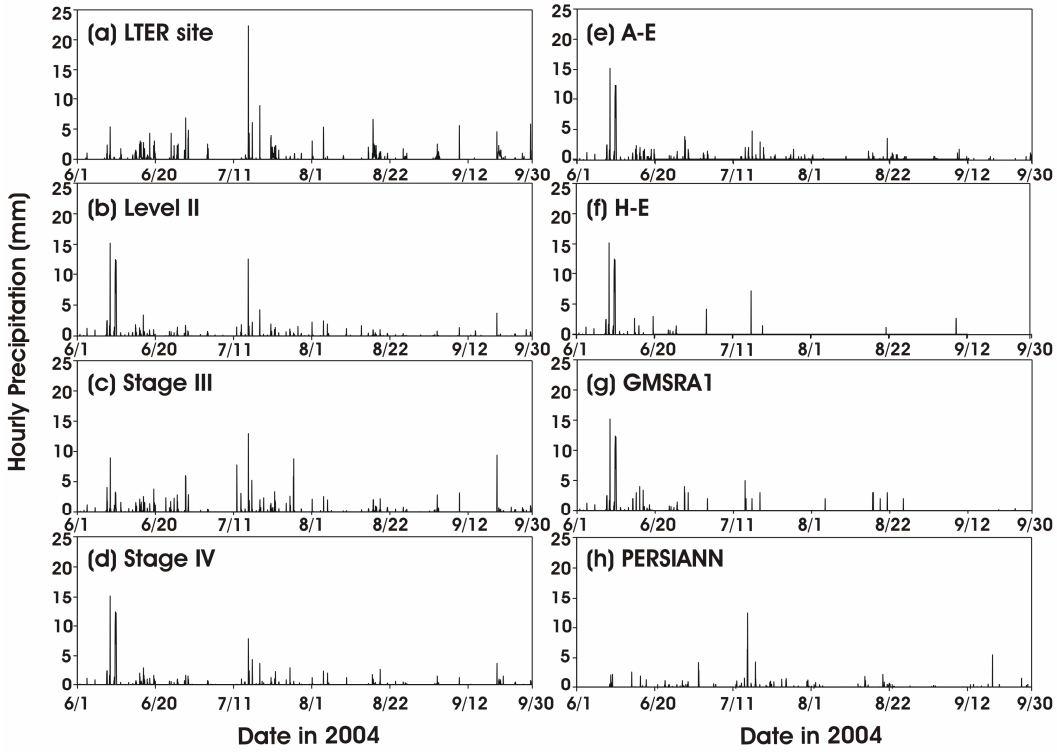

Figure 2.6. Hourly precipitation (mm) at (a) LTER rain gauge and the collocated pixels for (b) Level II at 4-km, (c) Stage III, (d) Stage IV, (e) A-E, (f) H-E, (g) GMSRA1, and (h) PERSIANN.

This is consistent with studies comparing ground data to satellite precipitation retrievals (Scofield and Kuligowski 2003; Sapiano and Arkin 2009; Yucel et al. 2011). While rain occurrences are reasonably captured by satellite QPEs, they tend to overestimate rainfall amounts in the early summer and underestimate them for the rest of the season. In general, all QPEs underestimate rainfall with respect to rain gauges, as evidenced by the Bias scores less than unity for most cases.

Table 2.5. Statistical evaluation of rainfall estimates from rain gauges and collocated pixels. ρ and R are the Pearson and Spearman rank correlations. P_{tot} is the seasonal rainfall accumulation. Bias is the ratio of the mean forecast and mean observation values (Wilks, 2006).

Precipitation Product	ESPC2 (P_{tot} = 355.2 mm)					RSOC2 (P_{tot} = 248.0 mm)				
	P_{tot} [mm]	ρ	R	Bias	RMSE [mm]	P_{tot} [mm]	ρ	R	Bias	RMSE [mm]
Level II	320.0	0.24	0.48	0.90	1.21	173.2	0.58	0.44	0.70	0.43
Stage III	403.4	0.37	0.63	1.14	1.09	110.9	0.36	0.36	0.45	0.50
Stage IV	429.1	0.45	0.62	1.21	1.03	117.0	0.36	0.29	0.47	0.50
A-E	199.6	0.26	0.38	0.56	1.07	220.4	0.23	0.29	0.89	0.59
H-E	95.3	0.22	0.28	0.27	1.08	111.7	0.24	0.21	0.45	0.56
H-Erad	92.6	0.23	0.28	0.26	1.08	108.7	0.24	0.21	0.44	0.56
GMSRA1	146.6	0.25	0.26	0.41	1.08	149.2	0.27	0.16	0.60	0.56
GMSRA2	191.0	0.2	0.19	0.54	1.10	182.6	0.16	0.09	0.74	0.59
Blend	649.4	0.06	0.24	1.83	2.13	650.9	0.02	0.10	2.62	2.00
PERSIANN	136.6	0.05	0.11	0.38	1.13	156.7	0.10	0.08	0.63	0.59
	PKLC2 (P_{tot} = 323.1 mm)					**LTER (P_{tot} = 352.9 mm)**				
Level II	214.0	0.55	0.49	0.66	0.61	250.6	0.32	0.47	0.71	0.80
Stage III	249.0	0.38	0.50	0.77	0.62	287.5	0.52	0.56	0.81	0.62
Stage IV	308.8	0.45	0.48	0.96	0.69	275.7	0.37	0.53	0.78	0.76
A-E	194.0	0.47	0.32	0.60	0.59	267.4	0.20	0.30	0.76	0.84
H-E	76.3	0.37	0.16	0.24	0.62	158.0	0.13	0.20	0.45	0.87
H-Erad	75.0	0.37	0.16	0.23	0.62	158.0	0.13	0.20	0.45	0.87
GMSRA1	121.9	0.41	0.19	0.38	0.62	192.8	0.11	0.22	0.55	0.84
GMSRA2	170.3	0.38	0.140	0.53	0.65	225.4	0.11	0.18	0.64	0.89
Blend	693.3	0.10	0.23	2.15	2.06	757.8	0.10	0.25	2.15	2.08
PERSIANN	101.5	0.18	0.17	0.31	0.64	131.5	0.23	0.11	0.37	0.69

Multiple factors could explain the underestimation including diurnal sampling uncertainties, tuning of the precipitation algorithm for other regimes, the comparatively small spatial scale of CFR storms, or unusual surface or atmosphere properties that QPE algorithms do not correctly interpret (Smith et al. 2006). There is also scale mismatch effect between pixel and point measurements that translates into lower rainfall estimates per pixel (Boushaki et al. 2009). For

most sites, the Pearson and Spearman rank correlations are larger for Level II, Stage III, Stage IV and A-E products, suggesting that these QPEs contain the most accurate depiction of rainfall at these validation locations. Figure 2.7 shows event distributions of hourly, basin-averaged rainfall for non-zero periods. In addition, the number of rain hours is presented, indicating when rainfall occurred at any site in the basin area. The lower number of rain hours for the rain gauges is related to two factors. First, rain gauges have a resolution of 0.1 mm, while QPE algorithms do not curtail rainfall below a threshold. Second, rain gauges measure at a single site where the likelihood of rainfall is smaller than for all pixels in a basin. These two factors lead to a higher median rainfall for rain gauges and larger outliers at FISH, SVRAIN and RALS. In most cases, the Level II 4-km product has the highest number of rainfall hours and the lowest median accumulations. Since this is a basin-average, this implies that Level II contains a large number of small rainfall events distributed in each basin. The Stage III and Stage IV products show similar behavior, but tend to have a lower number of events, in particular for BUCK where seasonal accumulations were low. In general, satellite QPEs exhibit similar event distributions among themselves and are characterized by low medians, reduced number of rainfall hours and a low number of outliers. Consistent with prior analyses, A-E has properties closest to radar and multisensor QPEs, while Blend presents outliers that affect its ability to capture the site, basin-average or regional rainfall distributions.

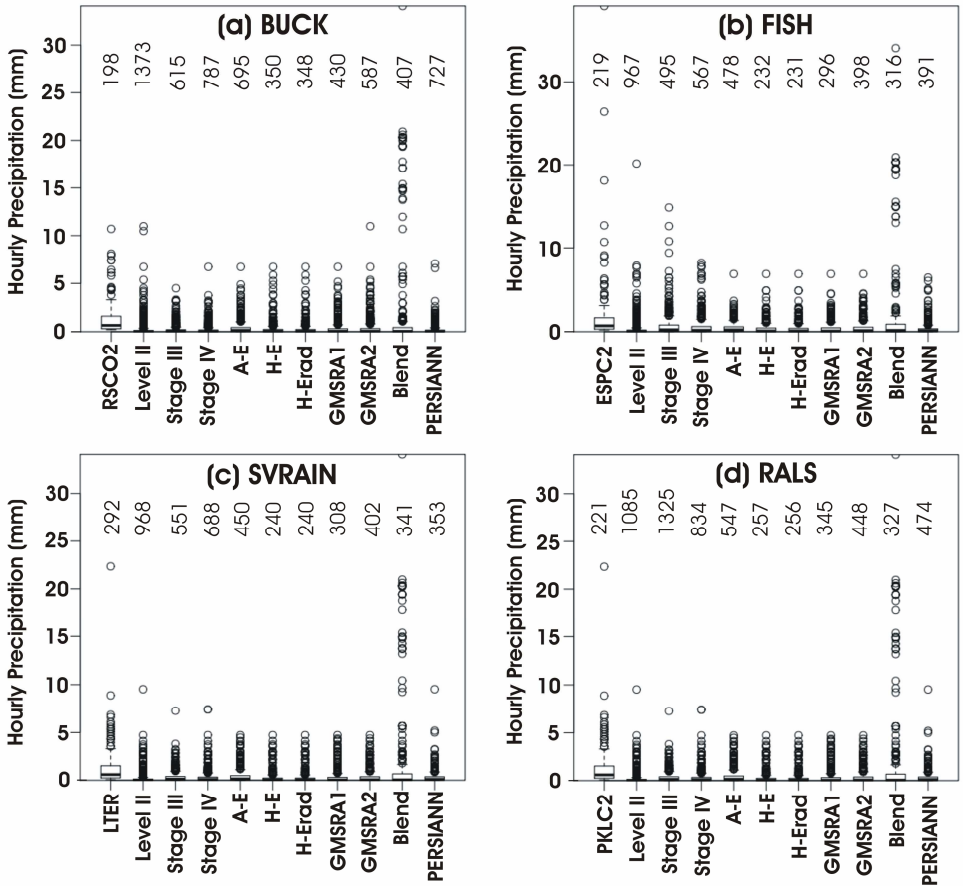

Figure 2.7. Box-and-whisker plots of hourly basin-averaged precipitation (mm) in each basin from the QPE products and closest rain gauge. Each plot presents the median (horizontal line), lower and upper quartiles (box) and the outliers beyond the 1.5 interquartile range (circles). Numbers at the top represent the total number of hourly (non-zero) rainfall values considered for each case.

Hydrological Intercomparison using Integrated Measures

The simulated basin responses resulting from the different QPE products are compared in terms of the outlet streamflow, underlying runoff mechanisms and water balance components. Streamflow error metrics are obtained from two reference hydrographs based on stream gauge data or the simulated response from the Level II 1-km forcing used for model calibration. Figure 2.8 presents the simulated hydrographs in each study basin for a number of representative QPEs

(Level II, Stage III, PERSIANN) as well as simulations obtained using spatially-uniform rain gauge forcing from the nearest gauge to each basin (i.e., 'Rain Gauge'). Results for all QPE products are presented in Table 2.6 through the use of evaluation metrics (ρ, *R*, *NS*, *Bias*, *RMSE*). The Pearson and Spearman Rank correlation coefficients (ρ and *R*) indicate the degree of agreement over all values, while the Root Mean Squared Error (*RMSE*) and Nash-Sutcliffe efficiency (*NS*) weight streamflow peak errors more heavily.

To aid in the comparison, Figure 2.9 shows the outlet discharge *RMSE* between the simulations and the observed streamflow, as well as, the *RMSE* between each case and the simulations obtained with the Level II 1-km forcing. Rain gauge forcing tends to overestimate simulated streamflow in each basin relative to both observations and Level II 1-km simulations. These errors are due to the assumption of spatially-uniform rainfall in each watershed where, in reality, summer storms or the principal rain cores of cloud systems are smaller in scale relative to the basin size. As a result, the *RMSE* of the rain gauge simulations are greater than most of the QPEs (except Blend) when compared against observations and Level II 1-km forcing (Figure 2.9). This has important implications for the different QPE products as their use is superior to assuming uniform rainfall conditions from nearby rain gauges.

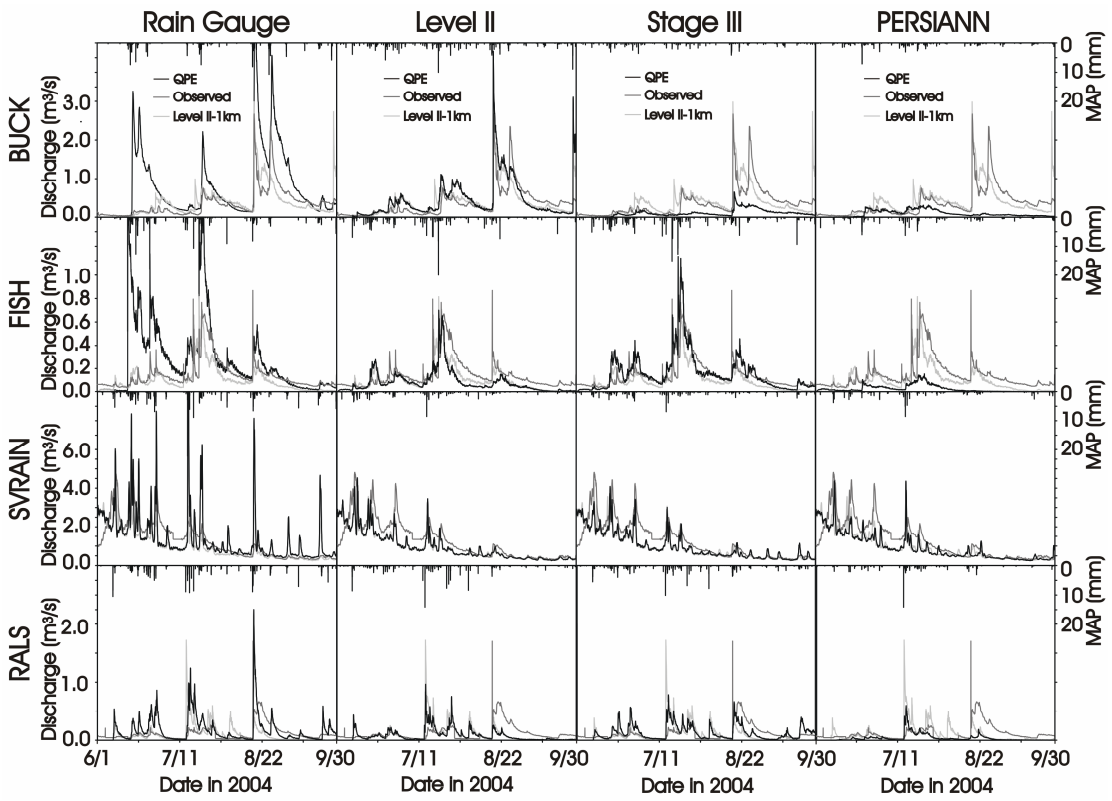

Figure 2.8. Simulated outlet streamflow (black lines) for the rain gauges and selected QPEs (Level II, Stage III, PERSIANN) in each basin. Observed (dark gray) and reference hydrographs (light gray) derived from the Level II 1-km forcing are shown for reference.

Based on the various statistical metrics, the QPEs with superior performance in terms of the outlet discharge are the following for each basin (in order): BUCK (Level II 4-km, Stage III), FISH (Stage III, Stage IV, Level II 4-km), SVRAIN (Stage III, Stage IV, A-E) and RALS (Stage III, Stage IV, PERSIANN). Over most basins, Stage III provides the most reliable simulations, though high *RMSE*s are present at BUCK due to low rainfall in northern areas (Figure 2.5). Good hydrologic performance of the multisensor products suggests that merging radar and rain gauge data, as achieved by the Stage III algorithm, is valuable for mountain areas.

Table 2.6. Statistical evaluation of streamflow simulations from multiple QPEs relative to the observed and simulated hydrographs derived from the Level II 1-km forcing (in parentheses). *NS* is the Nash-Sutcliffe efficiency (Legates and McCabe, 1999).

Basin			**BUCK**					**FISH**		
Precipitation Product	ρ **[-]**	***R*** **[-]**	**Bias [-]**	**NS [-]**	**RMSE [m^3/s]**	ρ **[-]**	***R*** **[-]**	**Bias [-]**	**NS [-]**	**RMSE [m^3/s]**
Rain gauge	0.76	0.72	2.23	-4.14	0.82	0.57	0.73	1.94	-5.07	0.30
	(0.64)	(0.62)	(2.14)	(-4.40)	(0.86)	(0.67)	(0.81)	(2.71)	(-6.73)	(0.31)
Level II	0.72	0.71	1.22	0.05	0.35	0.74	0.75	0.57	0.30	0.10
	(0.93)	(0.94)	(1.18)	(0.67)	(0.21)	(0.92)	(0.93)	(0.79)	(0.80)	(0.05)
Stage III	0.78	0.82	0.29	-0.13	0.39	0.80	0.86	1.12	0.37	0.10
	(0.74)	(0.76)	(0.28)	(-0.19)	(0.40)	(0.94)	(0.91)	(1.56)	(0.39)	(0.09)
Stage IV	0.04	0.23	0.37	-0.40	0.43	0.72	0.80	0.72	0.41	0.09
	(0.23)	(0.54)	(0.36)	(-0.33)	(0.43)	(0.90)	(0.89)	(1.00)	(0.80)	(0.05)
A-E	-0.13	0.06	1.42	-5.19	0.90	0.25	0.44	0.28	-0.62	0.15
	(0.08)	(0.42)	(1.36)	(-4.07)	(0.84)	(0.51)	(0.72)	(0.40)	(-0.06)	(0.11)
H-E	-0.17	-0.02	0.69	-1.31	0.55	-0.06	0.11	0.17	-1.01	0.17
	(0.06)	(0.32)	(0.66)	(-1.07)	(0.54)	(0.17)	(0.44)	(0.23)	(-0.46)	(0.13)
H-Erad	-0.15	-0.02	0.56	-0.93	0.50	-0.05	0.14	0.16	-1.02	0.17
	(0.0)	(0.32)	(0.54)	(-0.77)	(0.49)	(0.18)	(0.48)	(0.23)	(-0.46)	(0.13)
GMSRA1	-0.08	0.09	0.54	-0.66	0.47	0.23	0.32	0.20	-0.81	0.16
	(0.13)	(0.54)	(0.52)	(-0.41)	(0.44)	(0.54)	(0.64)	(0.27)	(-0.23)	(0.12)
GMSRA2	-0.03	0.17	0.97	-1.91	0.62	0.08	-0.05	0.22	-0.82	0.16
	(0.16)	(0.30)	(0.93)	(-1.31)	(0.57)	(0.36)	(0.23)	(0.31)	(-0.26)	(0.12)
Blend	-0.13	0.01	63.66	-36527	69.36	0.02	0.56	12.48	-2645	6.29
	(-0.07)	(0.36)	(61.20)	(-34709)	(69.33)	(0.03)	(0.72)	(17.4)	(-3192)	(6.30)
PERSIANN	-0.03	0.23	0.26	-0.55	0.45	0.72	0.54	0.17	-0.64	0.16
	(0.19)	(0.59)	(0.25)	(-0.48)	(0.45)	(0.77)	(0.70)	(0.23)	(-0.14)	(0.12)
			SVRAIN					**RALS**		
Rain gauge	0.57	0.82	1.09	-0.38	1.13	0.48	0.67	1.42	-1.64	0.20
	(0.68)	(0.87)	(1.43)	(-1.12)	(1.08)	(0.47)	(0.67)	(1.76)	(-1.07)	(0.21)
Level II	0.79	0.92	0.77	0.53	0.66	0.22	0.27	0.69	-0.38	0.15
	(0.99)	(0.99)	(1.01)	(0.97)	(0.13)	(0.91)	(0.96)	(0.85)	(0.77)	(0.07)
Stage III	0.81	0.92	0.79	0.57	0.63	0.49	0.56	1.06	-0.01	0.13
	(0.96)	(0.97)	(1.04)	(0.93)	(0.20)	(0.63)	(0.70)	(1.32)	(0.32)	(0.12)
Stage IV	0.79	0.91	0.84	0.58	0.62	0.39	0.52	0.86	-0.08	0.13
	(0.95)	(0.96)	(1.11)	(0.87)	(0.26)	(0.78)	(0.85)	(1.07)	(0.61)	(0.09)
A-E	0.80	0.91	0.81	0.58	0.62	0.12	0.32	0.77	-0.51	0.15
	(0.96)	(0.96)	(1.06)	(0.91)	(0.22)	(0.46)	(0.62)	(0.96)	(0.15)	(0.14)
H-E	0.77	0.92	0.70	0.42	0.73	-0.09	0.23	0.28	-0.74	0.16
	(0.94)	(0.96)	(0.92)	(0.87)	(0.27)	(0.12)	(0.32)	(0.35)	(-0.22)	(0.16)
H-Erad	0.77	0.92	0.70	0.42	0.73	-0.09	0.18	0.27	-0.76	0.16
	(0.94)	(0.96)	(0.92)	(0.87)	(0.27)	(0.13)	(0.41)	(0.33)	(-0.22)	(0.16)
GMSRA1	0.79	0.92	0.75	0.52	0.66	0.06	0.33	0.47	-0.69	0.16
	(0.96)	(0.97)	(0.99)	(0.91)	(0.22)	(0.56)	(0.71)	(0.59)	(0.25)	(0.13)
GMSRA2	0.77	0.87	0.77	0.50	0.68	0.02	0.23	0.55	-0.67	0.16
	(0.94)	(0.92)	(1.01)	(0.87)	(0.26)	(0.54)	(0.49)	(0.68)	(-0.25)	(0.13)
Blend	0.32	0.89	2.22	-50.27	6.88	-0.03	-0.08	39.6	-29751	21.4
	(0.28)	(0.90)	(2.92)	(-88.41)	(7.03)	(-0.04)	(0.55)	(49)	(-20819)	(21.4)
PERSIANN	0.77	0.88	0.74	0.47	0.70	0.30	0.41	0.31	-0.33	0.14
	(0.89)	(0.93)	(0.97)	(0.79)	(0.34)	(0.74)	(0.78)	(0.38)	(0.30)	(0.12)

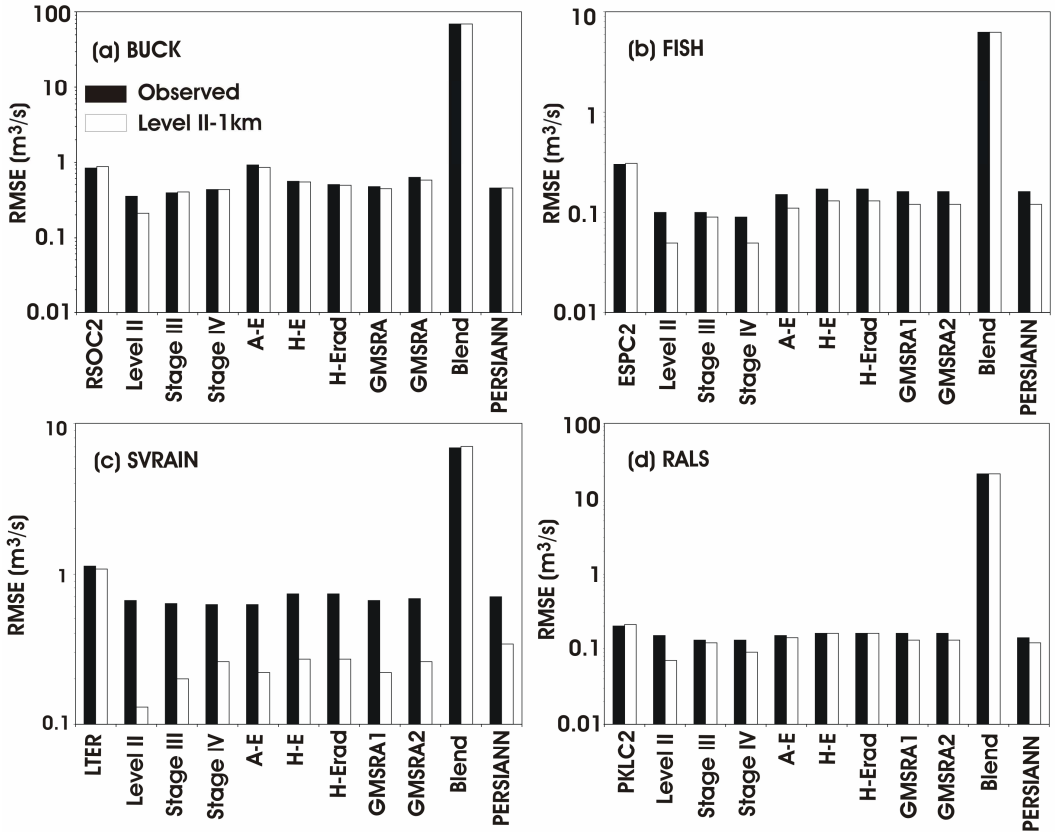

Figure 2.9. Outlet streamflow *RMSE* between simulations with different QPEs and observed data (black bars) and simulated hydrographs obtained using the Level II 1-km forcing (white bars). Note the varying logarithmic scale on the RMSE for each basin.

This also holds for the Level II product that used a limited number of rain gauges to derive a *Z-R* relation. Errors in the Level II 4-km simulations with respect to the 1-km forcing show that spatial aggregation has a substantial effect on the simulations relative to the calibrated model. Most satellite QPEs (except Blend) tend to underestimate the outlet discharge volume as indicated by the low Bias with respect to the observations and Level II 1-km forcing (Table 2.6). In addition, *RMSE*s are larger than the radar and multisensor products, but lower than rain gauge forcing. Since satellite QPEs exhibit lower rainfall magnitudes

and smoother fields, the resulting streamflow simulations are characterized by lower volumes and reduced variability, as shown for PERSIANN in Figure 2.8. For certain basins, however, some satellite QPEs can have performances that approach those obtained from the radar and multisensor products (e.g., A-E in SVRAIN and PERSIANN in RALS). Nevertheless, poorer performances of these products in other basins (e.g., A-E in RALS and PERSIANN in BUCK) suggest that their use in streamflow simulations across the CFR should be done with caution and perhaps with some kind of additional bias correction. These results indicate that satellite QPEs can serve as an effective alternative to uniform rain gauge forcing, but not for radar and radar-based multisensor products.

Differences in space-time rainfall behavior in each QPE may also condition the runoff mechanisms composing the basin response. Figure 2.10 presents the fraction of the outlet streamflow volume from each runoff type. Basin properties and model parameters yield differences in runoff composition across the basins, with BUCK and RALS consisting of infiltration-excess (INF) and saturation-excess (SAT) runoff; SVRAIN composed of groundwater exfiltration (GW) and SAT; and FISH having a mixture of all types. Clearly, the properties of each QPE lead to some variations in runoff mechanisms in each basin. Radar and multisensor QPEs with good performance relative to streamflow data exhibit similarities in runoff types. In most basins, Stage III and IV have higher fractions of SAT as compared to Level II, indicating that less frequent and lower magnitude rainfall pulses (Figure 2.7) favor this runoff type, as expected based on prior studies (Vivoni et al. 2007a).

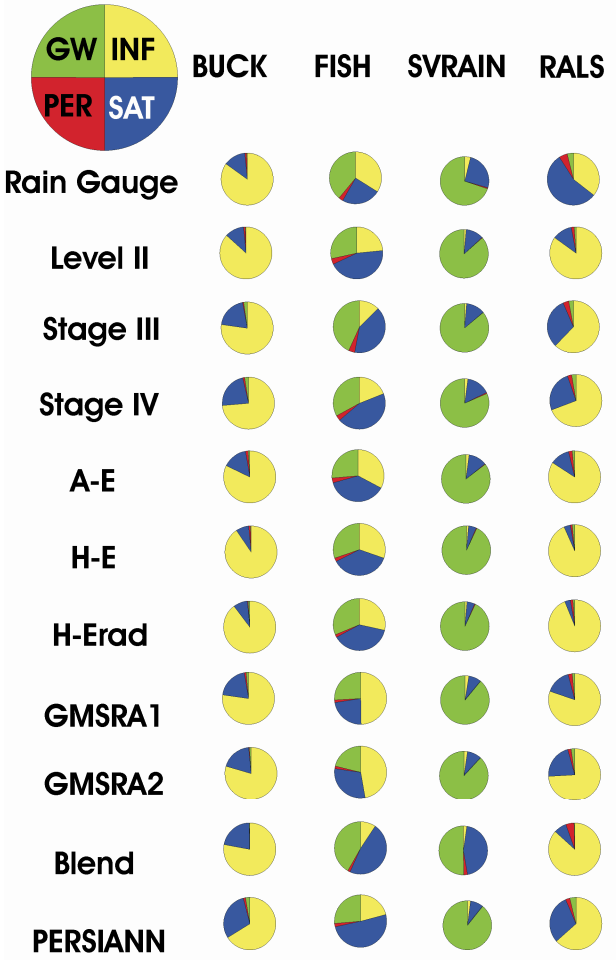

Figure 2.10. Fractions of runoff mechanisms for each QPE and study basin for: infiltration excess (INF), saturation excess (SAT), perched return flow (PER) and groundwater exfiltration (GW).

Rain gauge input also favors SAT as compared to Level II in most basins, except in FISH where GW and INF are enhanced with uniform forcing. Overall, the satellite QPE products induce variations in runoff types relative to Level II that are comparable to rain gauge and multisensor products (except Blend at SVRAIN). This indicates that while satellite QPE products lead to discrepancies in outlet streamflow, they do not fundamentally change the nature of the runoff types underlying the model response.

The seasonal water balance may also vary according to the precipitation forcing from each QPE. Figure 2.11 presents the water balance components for the simulation period (1 June to 30 September 2004, Δt = 4 mon) as $\Delta S / \Delta t = P - ET - Q$, where ΔS is change in basin water storage estimated from the basin-averaged precipitation (*P*) and evapotranspiration (*ET*), and streamflow at the outlet (*Q*). In three of the four basins (except SVRAIN), *P* is partitioned primarily into *ET*, as *Q* is less than 25% of *P*. For most QPEs in these basins, *ET* is greater than or comparable to *P*, indicating that warm-season *ET* is high and that a fraction of water in storage is consumed by *ET* during the summer, leading to negative ΔS. At the low to mid altitudes of FISH, BUCK and RALS, high *ET* occurs in response to elevated air temperatures and broad forest cover. SVRAIN has a different seasonal behavior, with relatively low *ET*, high *Q* and negative ΔS, indicating that the high altitude basin drains its water storage and precipitation input. This occurs in response to wet initial conditions imposed in the basin to account for snowmelt inputs in the early summer. Radar and multisensor QPEs with good performance relative to streamflow observations have similarities in water balance components. Differences in *P* are compensated by variations in ΔS and *ET*, with their proportional changes varying for each basin (i.e., ΔS compensations in BUCK, *ET* compensations in FISH). In most cases, uniform rain gauge forcing is similar to the Level II 4-km and multisensor products. One notable difference is higher *Q* in the rain gauge simulations observed when either *P* is larger or smaller than in the Level II forcing, implying that spatially-uniform forcing has prominent effects on basin runoff amounts.

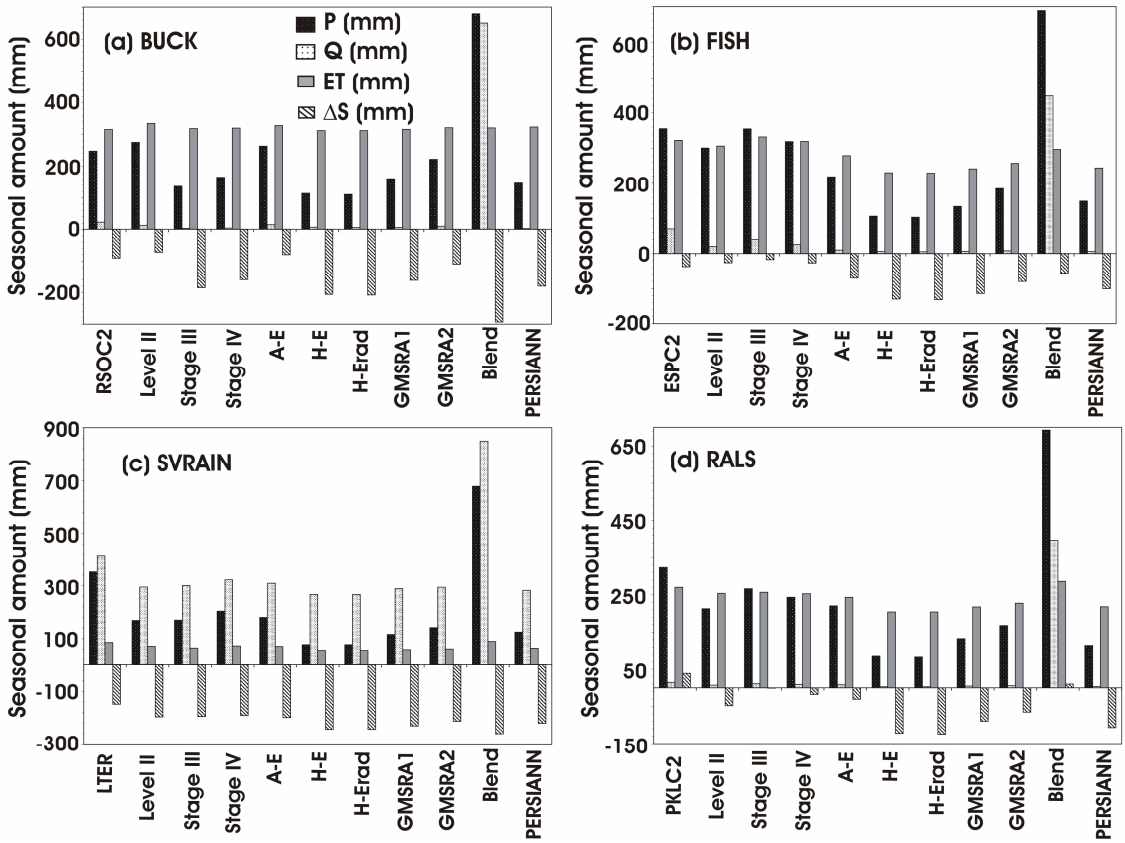

Figure 2.11. Seasonal water balance components for each QPE and study basin for: precipitation (*P*), streamflow (*Q*), evapotranspiration (*ET*) and change in storage (Δ*S*).

Overall, for the satellite QPEs, a low *P* and comparable *ET* lead to greater storage losses from the basins (more negative *ΔS*). When precipitation is severely underestimated (e.g., H-E at BUCK, RALS), low amounts of available soil moisture also begins to limit *ET*. Other than these discrepancies, the satellite QPEs are similar to radar and multisensor products, with the exception of Blend that has a high *P* that is partitioned into streamflow with limited impacts on storage or evapotranspiration.

Hydrological Intercomparisons using Distributed Measures

The spatiotemporal variability of rainfall from each QPE product may also influence the distributed basin response. For each basin and product, hydrographs at internal sites, runoff maps and the relations between the spatial variability in rainfall and runoff are compared. Figure 2.12 presents an example of the intercomparison for a significant storm event on 18-19 August in BUCK (Figure 2.4) for a selected set of QPEs (Rain gauge, Level II 1-km and 4-km, Stage III and PERSIANN). Although Level II 1-km and uniform rain gauge inputs do not possess the same effective spatial resolution, they have been added to this analysis for comparison purposes. For each QPE, the 24-hr rainfall and 87-hr runoff accumulation maps are shown. To derive the runoff accumulation, the hourly runoff amounts at individual sites prior to routing are aggregated in time. In addition, hydrographs at four channel sites show internal streamflow variations that are associated with the mean areal precipitation within upstream areas.

Cleary, the spatial aggregations of rainfall have an influence on the runoff patterns at the storm scale. Rain gauge forcing leads to low and nearly uniform runoff production, while Level II 1-km identifies a storm cell in the western region that concentrates rainfall and runoff in that area, with minor amounts elsewhere. As a result, the rain gauge hydrographs differ from Level II 1-km as well as the observed discharge, with underestimations at the storm location and overestimations at the outlet. In contrast, Level II 4-km captures the runoff response well with only minor variations at internal sites and coarsening of the runoff map.

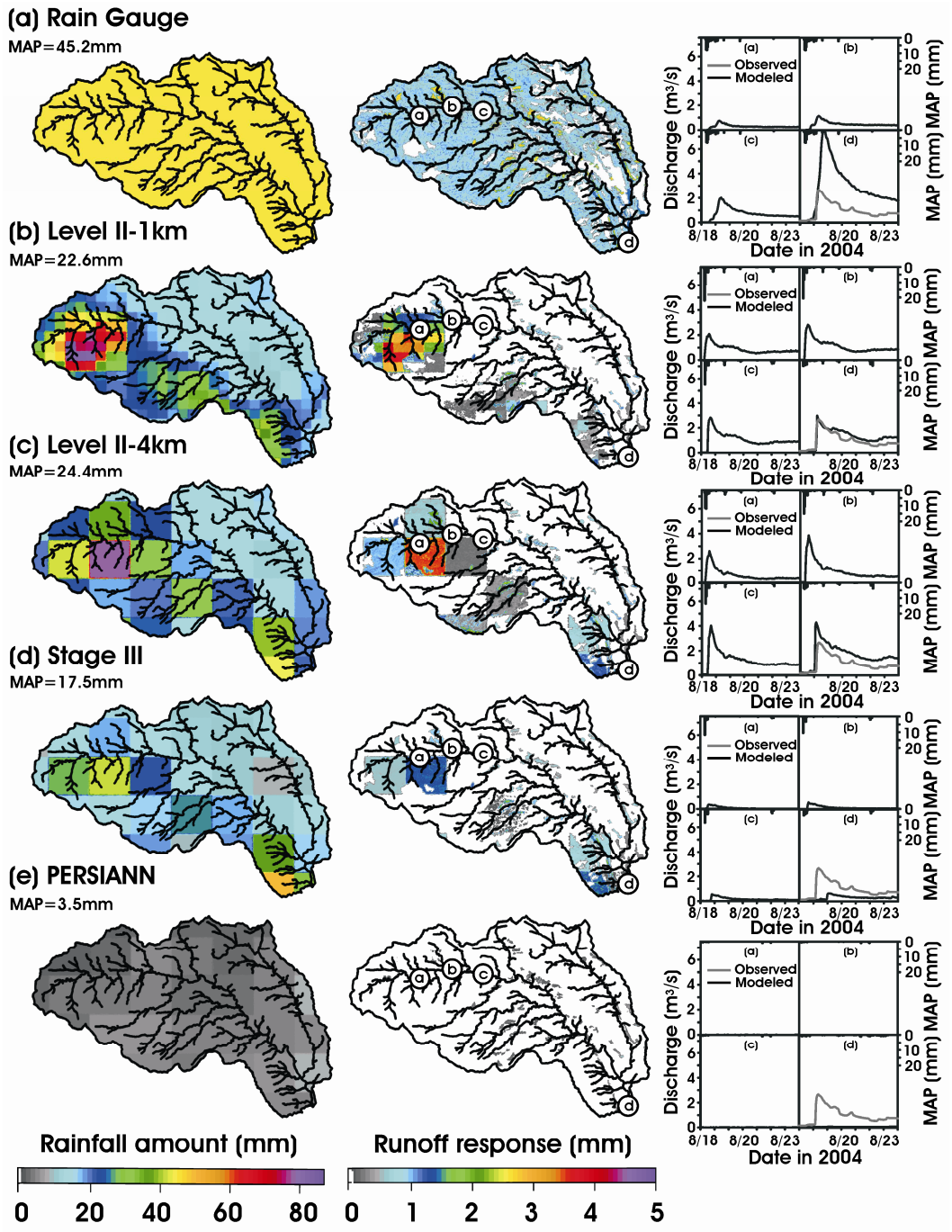

Figure 2.12. Spatial distribution of rainfall (left panels) and runoff (middle panels) accumulations in BUCK for selected QPEs (Rain gauge, Level II 1-km, Level II 4-km, Stage III, PERSIANN) for an event occurred in August 18, 2004. Sub-basin averaged precipitation and streamflow at three nested locations and the basin outlet are presented in the right panel.

This indicates that aggregation effects of Level II are not severe, though outlet discharge metrics are somewhat impacted (Figure 2.9). At BUCK, multisensor and satellite QPEs underestimate rainfall, leading to poor comparisons at internal sites relative to Level II 1-km. For example, PERSIANN has a low and nearly uniform rainfall, thus generating insufficient runoff. Stage III, on the other hand, is able to depict better the rainfall and runoff distributions in the basin, though the observed discharge at the outlet is underestimated. This is consistent with the low reported rainfall values by Stage III at BUCK. Thus, radar and multisensor QPEs that preserve small storms relative to the basin size have advantages in runoff prediction over QPEs with low or no spatial variations.

The impact of the spatial rainfall distribution is explored for all QPEs in Figure 2.13 for the three most significant events in each basin. Table 2.7 summarizes the rainfall start times and total event durations. In these analyses, the spatially-uniform rain gauge forcing is used as a reference and there are 132 QPE simulations based on eleven products, four basins and three events. For example, Figure 2.13a illustrates the *RMSE* of outlet discharge for each QPE relative to the observed discharge versus the equivalent *RMSE* obtained from the rain gauge forcing. For most cases, the QPE *RMSE*s are below the 1:1 line (except for one storm in RALS), indicating that QPEs have smaller peak errors compared to those from rain gauge simulations. The degree of improvement achieved by distributed forcing is shown in Figure 2.13b as the percentage of events for which QPEs have a lower *RMSE*.

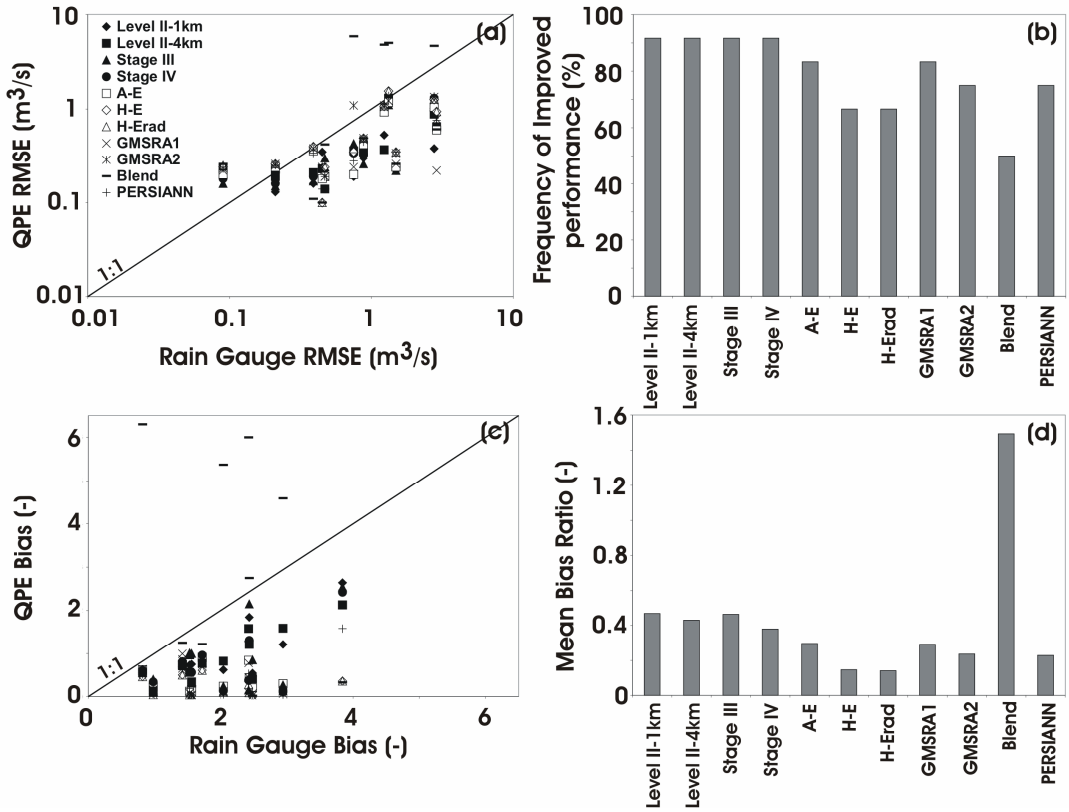

Figure 2.13. Comparison of QPE product skill relative to rain gauge simulations for three selected storms in all study basins. (a) Outlet discharge *RMSE*. (b) Frequency of improved performance using QPEs. (c) Outlet discharge bias. (d) Mean ratio of QPE bias to rain gauge bias.

A similar analysis based on the streamflow volumes, using the *Bias*, is presented in Figure 2.13c. QPE simulations have a lower *Bias* than equivalent rain gauge simulations (except for five events for Blend). Thus, the *mean bias ratio* shown in Figure 2.13d, defined as the bias of a QPE simulation divided by the bias of a rain gauge simulation, shows values lower than unity for most products. This indicates that distributed QPEs, including satellite-based products, have improved streamflow volumes relative to the uniform rain gauge forcing.

Table 2.7. Three selected events in each basin, including the rainfall start time (month/day/hour) in 2004 and the total event duration (h), including rainfall and runoff periods.

	BUCK		FISH		SVRAIN		RALS	
Event	**Start time in 2004**	**Duration [h]**	**Start time in 2004**	**Duration [h]**	**Start time in 2004**	**Duration [h]**	**Start time in 2004**	**Duration [h]**
1	07/22/02	110	07/18/08	40	06/26/17	150	07/15/00	167
2	08/18/10	87	07/21/06	370	07/30/10	150	08/17/15	50
3	08/25/06	210	08/17/08	100	09/01/18	250	08/26/12	100

A further distributed comparison of the QPE products is carried out by quantifying the spatial coefficient of variation (CV) of the rainfall (*CVrain*) and runoff (*CVrunoff*) fields for each hour with non-zero values (*N*). CV is obtained as the spatial standard deviation of the quantity of interest divided by the basin-average quantity. The metric $CVratio = CVrunoff/CVrain$ is defined to compare the relative spatial variability of the runoff field to the rainfall field, with larger values implying a more variable runoff distribution. Figure 2.14 presents *CVratio* for the four basins and a selected number of QPEs (Level II 1-km and 4-km, Stage III and PERSIANN) as a function of the hourly runoff ratio ($\phi = Q/P$) averaged over the basin. For each case, there are *N* values corresponding to the hours with coincident runoff and rainfall in each basin. In addition, a power law regression of the form $CVratio = c\phi^a$ is shown for each case, with *c* and *a* as the coefficient and exponent, respectively. Since *CVratio* is undefined for uniform rain gauge forcing ($CVrain = 0$), the ranges of values of ϕ for the rain gauge simulations are shown as reference.

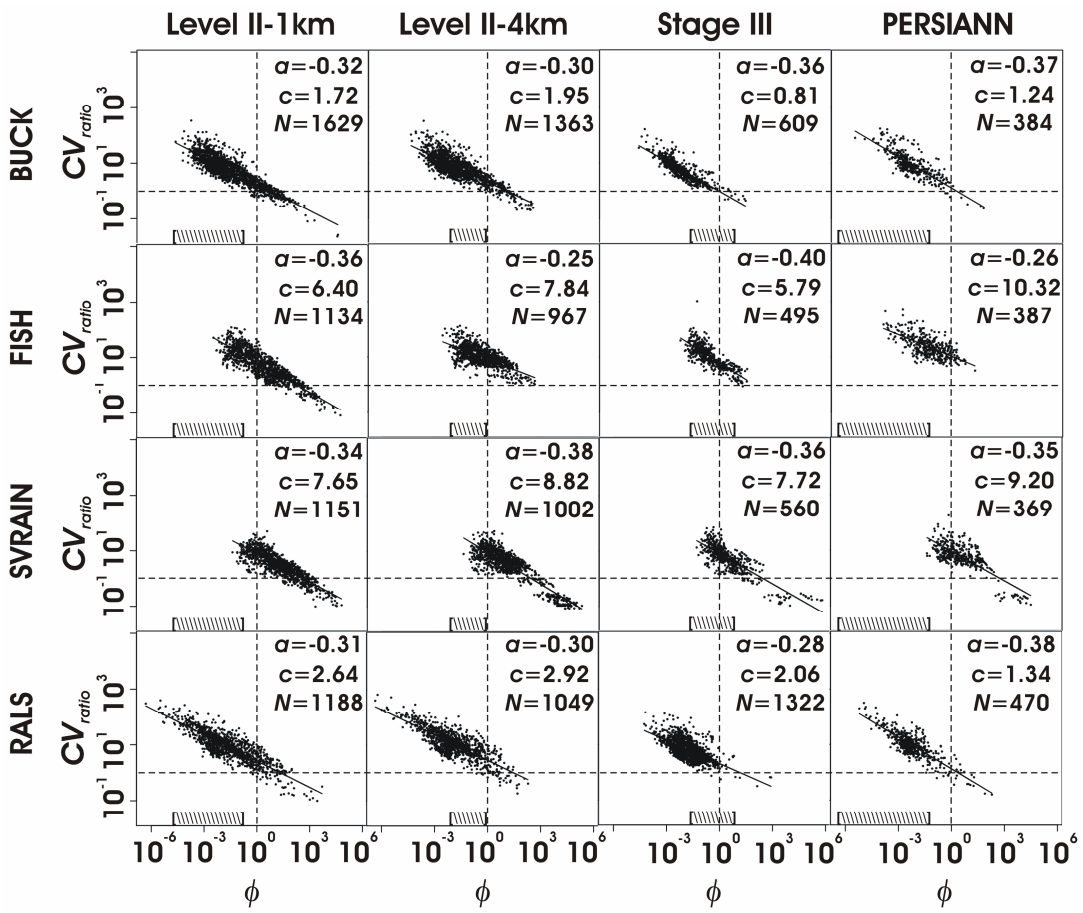

Figure 2.14. Relation between CV_{ratio} and runoff ratio (ϕ) for all basins and selected QPEs (Level II 1-km, Level II 4-km, Stage III, PERSIANN). Regressions shown as power laws (solid lines): $CV_{ratio} = c\phi^a$, with *c* and *a* indicated for each case. *N* is the sample size. The shaded region represents the range of ϕ for the rain gauge simulations.

Clearly, the spatial variation in runoff is typically larger than the corresponding variation in rainfall (*CVratio* > 1), as represented by values above the dashed horizontal line. This is due to several factors, including the landscape properties (terrain, soils, vegetation) that induce spatial runoff variations at scales smaller than precipitation forcing. For example, several runoff types induce patterns that follow the linear channel network features, which are smaller than

individual QPE pixels (Figure 2.12). The highest *CVratio* are observed for the lowest ϕ and vice versa, indicating that the hourly periods with lower runoff (relative to rainfall) have proportionally greater runoff variability in space, likely due to the delayed runoff contributions from groundwater that occur near channels. This effect is due to an interaction of the spatial rainfall variability, which exhibits greater variation with higher magnitudes (not shown), with the watershed properties in each basin. Interestingly, the slope of the relation between *CVratio* and ϕ has limited range of a = -0.25 to -0.4 across all basins and QPE products, suggesting that a single scaling relation can explain spatial patterns across a wide range of basin conditions For a few hours in each basin, both $\phi > 1$ and *CVratio* < 1, indicating that major runoff events with low relative spatial variability in runoff are infrequent. These events have both storm event and pre-event groundwater contributions to the total runoff, leading to $\phi > 1$. Note the ranges of values of ϕ for the rain gauge simulations are either smaller than or at the middle of the QPE range. This is consistent with analyses indicating overestimation of rainfall by the uniform forcing and their corresponding runoff underestimation.

SUMMARY AND CONCLUSIONS

In this study, we compared a set of Quantitative Precipitation Estimates (QPEs) in the Colorado Front Range for their ability to serve as forcing to a distributed hydrologic model that can issue flood forecasts. The region is known to generate warm-season convective storms with a high potential for flood and

flash flood events in individual basins. Given the sparse rain gauge data in the mountain region, we postulated that a distributed model could be used to verify QPEs from radar, multisensor and satellite algorithms. Hydrologic simulations in the mountain setting are challenging due to the complex nature of the basin characteristics as well as the small-scale of storm events. In evaluating the QPEs, we focused on the rainfall properties at the site, basin-average and regional scales and its propagation to the hydrologic response, including the outlet discharge, runoff mechanisms and seasonal water balance components. In addition, an emphasis was placed on identifying the value of gridded QPEs with respect to uniform forcing from rain gauges and to compare simulations against observed streamflows. Results indicate the following:

1) The timing, distribution and magnitude of warm-season precipitation are similar in the radar and radar-based multisensor products and can be captured well by some satellite QPE products (e.g., A-E). Overall, satellite products tend to underestimate rainfall at the site, basin-average and regional scales. One satellite QPE (Blend) exhibited poor performance in rainfall estimation. Basin-averaged forcing from mountain rain gauges results in overestimations in total volume and underestimations in the number of low accumulation rain events within a watershed.

2) The timing and magnitude of outlet streamflow in the four basins varies depending on the QPE forcing indicating its usefulness as a verification tool. Radar and multisensor products have good performances relative to the stream gauge observations and the Level II 1-km forcing used during model calibration.

Satellite QPEs, on the other hand, underestimate total discharge volume and introduce errors from their smoother and lower magnitude rainfall fields. However, as compared to uniform forcing from rain gauge data, most satellite QPEs exhibit improved abilities to capture streamflow across mountain basins with different land surface properties.

3) Individual watershed characteristics and initial wetness states condition the response in terms of the runoff generation types and water balance components. Relative to Level II 1-km, each QPE induces modifications to the runoff and water balance partitioning. Satellite QPEs that underestimate rainfall lead to greater storage changes to meet evapotranspiration demand; while rain gauges tend to produce more streamflow. Overall, however, QPEs do not fundamentally change the nature of the runoff or water balance partitioning that underlies the model response

4) The spatial variability of precipitation impacts the distributed basin response, including storm runoff patterns and discharge at interior channel locations, with clear effects of the spatial aggregation of QPE products. Relative to rain gauge forcing, radar and multisensor QPEs that preserve small storms relative to the basin area have advantages in terms of runoff prediction. Satellite QPEs also show better performance than rain gauges with respect to streamflow timing and volume for most cases, indicating their value for hydrologic forecasting in mountain areas.

5) A scaling relation ($CVratio = c\phi^{a}$) was found between the relative spatial variability of runoff and the runoff ratio across all study basins and QPE

products. This indicates that periods with low runoff ratios exhibit higher spatial variations in runoff relative to precipitation patterns, and vice-versa. The exponent of the relation was found to vary within a narrow range, a = -0.25 to -0.4, suggesting that is applicable across a wide range of basin conditions. Rain gauge forcing exhibits smaller runoff ratios than QPEs, consistent with other uniform forcing analyses.

The results of this study are based on the use of a distributed hydrologic model calibrated during one summer season using the hourly, Level II 1-km product. Given the differences among basins, model calibration was based on merging manual and automated methods independently for each watershed. Good model performance relative to the outlet streamflow observations and realistic model behavior for the given conditions in each basin support the use of the distributed model. The model was then used to study the propagation of the radar, multisensor and satellite QPEs and the uniform rain gauge forcing into the response of each study watershed. Simulations with the multisensor and satellite QPEs are considered independent of the calibration effort, while the rain gauges were used to derive the *Z-R* relation for the Level II 1-km product. Despite this advantage, spatially-averaged rain gauge simulations are not comparable in skill to those obtained from the gridded products. This indicates that spatial variations present in gridded QPEs add value for flood forecasting in mountain areas with sparse data even if those products contain some biases. Since the rain gauges were critical in calibrating the radar QPEs, our results do not suggest that in situ data do not have value since these are essential for ground-truthing remote sensing

products. In contrast, this study highlights the advantages and disadvantages associated with ground measurements and QPEs derived from remote sensing. Clearly, these conclusions need to be further evaluated in other basins and for additional summer periods in the region.

The results of this study are encouraging in that radar, multisensor and satellite QPEs offer a new window to study hydrological processes of mountain areas. At varying degrees of ability, gridded QPEs from these platforms are able to depict spatiotemporal rainfall patterns that are accurate with respect to their streamflow forecasts at individual gauging sites. Moreover, the QPEs and their error sources do not appear to fundamentally alter the simulated processes in particular basins. As a result, this study suggests that advances in mountain flood forecasting are possible by using high-resolution QPEs, including those from satellite platforms that more readily observe precipitation in regions with complex topography. For operational applications, the use of gridded QPE products should be superior to the assumption of uniform forcing from rain gauges in mountain areas, where the scale of warm-season storms is smaller than the basin area. Furthermore, the use of a distributed hydrologic model for flood forecasting with gridded QPEs opens new avenues to study the relations that characterize spatial patterns in precipitation and runoff generation. The simple scaling relation presented here that links relative spatial runoff variability and magnitude across the distinct watersheds also warrants further attention.

Chapter 3

PROPAGATION OF ERRORS FROM THE REFLECTIVITY-RAINFALL RELATION INTO SIMULATED STREAMFLOWS IN MOUNTAIN WATERSHEDS DURING SUMMER CONVECTION

INTRODUCTION

Accurate flood and flash flood predictions using distributed hydrologic models rely upon the underlying quality of the rainfall input (Moulin et al. 2009; Krajewski et al. 2010; McMillan et al. 2011; Schröter et al. 2011). This premise is particularly relevant in mountain catchments under summer convective storms where terrain features add complexity to the rainfall-runoff transformation (e.g., Zappa et al. 2011; Moreno et al. 2012a). Weather radars are widely used for quantifying precipitation at fine spatial and temporal resolutions by measuring the power of the return echo or reflectivity (Z) to derive rainfall rates (R) using a power law, $Z=AR^b$, where A and b depend on radar and precipitation characteristics (Collier 1996; Habib et al. 2008; Krajewski et al. 2010). Frequently, a single Z-R relation is used for estimating rainfall fields for all conditions as they offer operational advantages for flood forecasting (Habib et al. 2008; Alfieri et al. 2010) and retain storm characteristics important for seasonal modeling (Yoo et al. 2010).

Difficulty arises when the lack of a calibration procedure from rain gauges or disdrometer data for a particular area results in the assumption of an operational Z-R relation, such as the WSR-57 ($Z=200R^{1.6}$, Marshall and Palmer 1948) or the NEXRAD relations ($Z=300R^{1.4}$, Fulton et al. 1998; Krajewski et al.

2010). Use of an operational or climatological *Z-R* derived for other sites and climatic conditions, is not ideal as parameters, *A* and *b*, are known to vary with many factors, most prominently the drop size distribution (DSD). DSD has been found to vary between climatic regions, temporal aggregations and types of precipitation (Lee and Zawadzki 2005; Habib et al. 2008; Mapiam and Sriwongsitanon 2009). As a result, precipitation estimation errors can be introduced from the assumed *Z-R* relation, as shown by Morin et al. (2006) for summer storms in Arizona. One approach to overcome this limitation is through the derivation of a seasonal *Z-R* valid for particular storm types (i.e., convective, stratiform) which attempts to maximize the similarity of the radar product with rain gauges in a region or season of interest.

Precipitation estimates from weather radars also suffer from a range of other uncertainties including beam attenuation, hydrometeor melting or so-called bright band effects, anomalous propagation, beam blockage, ground clutter, hail contamination and other spurious returns (Baeck and Smith 1998; Krajewski et al. 2010). Many of those factors are difficult to avoid as they depend on the physics of the interaction between the beam signal, the hydrometeors and the surrounding environment. However, the *Z-R* relation has been shown to be a crucial factor in obtaining a correct spatial and temporal representation of rainfall (Pessoa et al. 1993; Baek and Smith 1998; Habib et al. 2008). The parameters of this relation depend on the time scale of calibration (minutes to days; Mapiam and Sriwongsitanon 2009; Alfieri et al. 2010), type of rainfall (convective, snow, stratiform; Pratt and Barros 2009), topographic setting (flat or mountain areas;

Baeck and Smith 1998) and the parameter estimation method from measured DSDs or rain gauges at known locations (Yoo et al. 2010; McMillan et al. 2011). Therefore, theoretically, coefficient and exponent of the *Z-R* relation should reflect their variation through spatio-temporal dependence functions $A_{t,s}=f(t,s)$ and $b_{t,s}=g(t,s)$ that could constitute the basis for ensemble members in a stochastic framework approach. In operational meteorology, however, a practical assumption is frequently made by keeping those parameters deterministic across broad regions for seasonally characteristic rainfall types.

Quantification of the uncertainties introduced by a *Z-R* relation on the hydrologic response of mountain watersheds remains a challenging question. Numerous studies have evaluated the impact of *Z-R*-derived radar rainfall fields on the accuracy of hydrologic models, but relatively few have focused on mountain catchments. For example, Habib et al. (2008) explores the sensitivity of streamflow simulations in a 35 km^2 basin in Louisiana to different *Z-R* relations using DSD as calibration data. *Z-R* relations at different temporal aggregations showed large variations between storms and within the same storm. A combined method for estimating the *Z-R* parameters, that maintained a constant exponent *b* for the summer season but adjusted coefficient *A* for each event, was found to be more practical and similar in accuracy as compared to event-specific parameters for storms in Arizona and Louisiana (Morin et al. 2006; Habib et al. 2008).

The use of a distributed hydrologic model allows investigating the spatial characteristics of the hydrologic response (Habib et al. 2008) while also assessing the impact of the *Z-R* relation on spatial processes. In principle, precipitation

errors introduced by the specification of the *Z-R* relation propagate to the hydrologic model, interacting with catchment properties. Compared to other error sources, such as parameter values or initial conditions, several studies have concluded that rainfall errors dominate the hydrologic response (Sharif et al. 2004; Germann et al. 2009; McMillan et al. 2011; Schröter et al. 2011; Zappa et al. 2011). Essentially, flood forecast errors should depend on how the precipitation forcing interacts with the spatial patterns of catchment properties (e.g., soil, vegetation, terrain and channel network). For example, Mascaro et al. (2010b) provided a physical explanation for flood forecasting error dispersion across different catchment scales by comparing how catchment properties affected the sub-basin responses.

Given the complexity in translating precipitation estimation errors into simulated hydrologic responses, questions remain regarding the effect of errors introduced by an incorrect sampling of the parameters of the *Z-R* relation, or the assumption of an operational relation, on the flood forecasting skill. For example, how do reflectivity-rainfall sampling errors propagate to the streamflow response? How does the sampling of different *Z-R* relations translate into spatial patterns of runoff production? Are there characteristic streamflow and flood forecasting error dependencies across aggregated spatial scales? To address these questions, we selected the Colorado Front Range (CFR) as a test bed due to its complex topography, the presence of reasonably close range weather radars, the frequency of convective storms during the summer season and an appreciable flood and flash flood risk (Moreno et al. 2012a). We evaluate the uncertainty introduced by

different *Z-R* relations applied to 1-km, hourly radar fields in four mountain basins (35 to 350 km^2 in area) during the 2004 summer season that was coincident with the North American Monsoon Experiment (Higgins and Gochis 2007).

In the following, we first derive a seasonal *Z-R* relation ($Z=700R^{1.3}$) for the CFR during summer 2004 with respect to seven rain gauges. Subsequently, we assess the propagation of rainfall errors introduced by different *Z-R* relations using the Triangulated Irregular Network (TIN)-based Real-time Integrated Basin Simulator (tRIBS) calibrated in each basin. The model explicitly accounts for spatial variations in watershed characteristics (topography, soils, vegetation) as well as rainfall forcing from weather radars (e.g., Ivanov et al. 2004; Vivoni et al. 2007a). tRIBS includes parameterizations of rainfall interception, evapotranspiration, infiltration with continuous soil moisture accounting, lateral moisture transfer in the unsaturated and saturated zones, and runoff routing. The model stresses the role of topography in lateral soil moisture redistribution accounting for the effects of heterogeneous and anisotropic soil. Spatially distributed surface-subsurface hillslope runoff is integrated by channel network routing. As a result, it is an excellent tool to study the propagation of precipitation errors into streamflow simulations and the distributed hydrologic response. The model allows exploration of the effects of the reflectivity-rainfall sampling on the types and spatial distribution of triggered runoff, the components of the seasonal water balance and the uncertainty introduced by rainfall at different catchment scales.

METHODS

Study Region and Watershed Properties

The CFR was selected for testing the hydrologic uncertainty of radar precipitation fields for several reasons. First, the varied topography and its range of vegetation and soil types result in complex, highly variable watershed responses when forced with summer convective storms. Second, the region has reasonably good radar coverage and a number of rain gauges, weather stations, and streamflow measurements despite its mountainous setting. Fig. 3.1 presents the locations of these observations within the CFR. Eleven headwater basins upstream of river gauging stations operated by the US Geological Survey and the Colorado Division of Water Resources were delineated as a part of an ongoing research effort. Four of these basins were selected for this hydrologic evaluation: Buckhorn Creek (BUCK, 350 km^2), Fish Creek (FISH, 41 km^2), Ralston Creek (RALS, 117 km^2) and South Saint Vrain Creek (SVRAIN, 35 km^2). This selection was based on the sampling of different drainage areas and a variety of landscape properties along a north-to-south gradient including the presence of snow melting processes during summer stream flows. Thus selected catchments constitute an excellent test bed for purposes of multiple hydrologic verification. Fig. 3.2 shows the spatial distribution of vegetation and soil maps across the CFR region, while Table 3.1 summarizes types and sources of the hydrologic information used in this study.

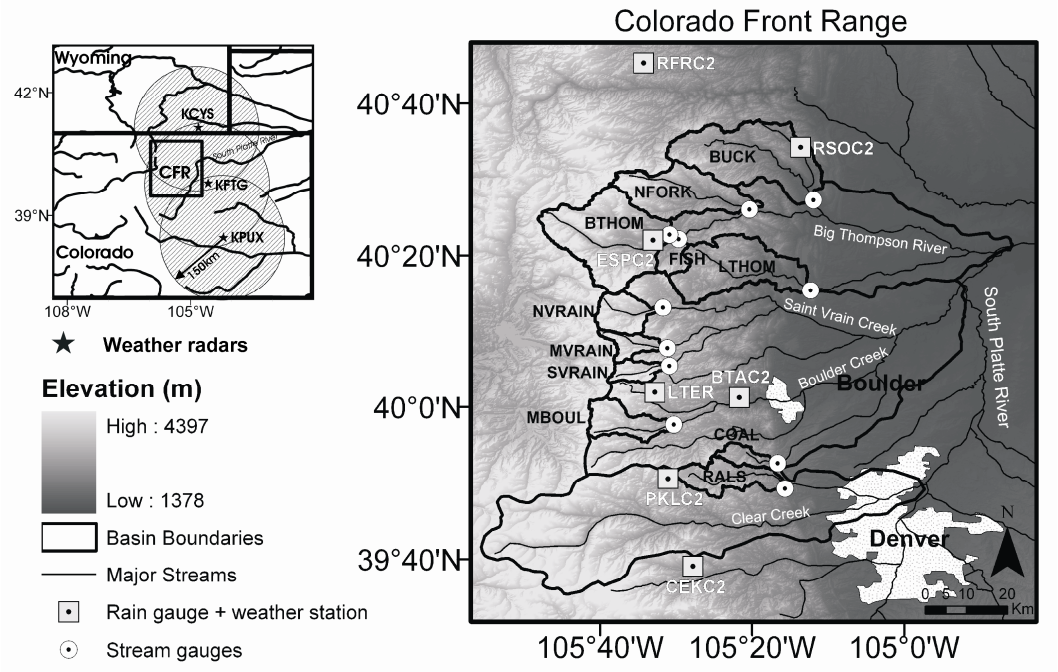

Figure 3.1. CFR location, elevation distribution and boundaries of eleven watersheds. Four basins are selected here: BUCK, FISH, RALS and SVRAIN. Seven hourly rain gauge and weather stations are shown: RFRC2, RSOC2, ESPC2, LTER, BTAC2, PKLC2 and CEKC2. Three weather radars KCYS, KFTG, KPUX and their 150 km coverage umbrellas are depicted.

The CFR is characterized by large elevation gradients, descending from west to east, which is dissected with narrow valleys and dendritic channel networks, resulting in a series of west-east ridgelines and north- and south- facing slopes. The soils are predominantly sandy loam, loam and exposed bedrock structure while prevalent vegetation types are constituted by forests and grasslands, as illustrated by the Figure 3.2.

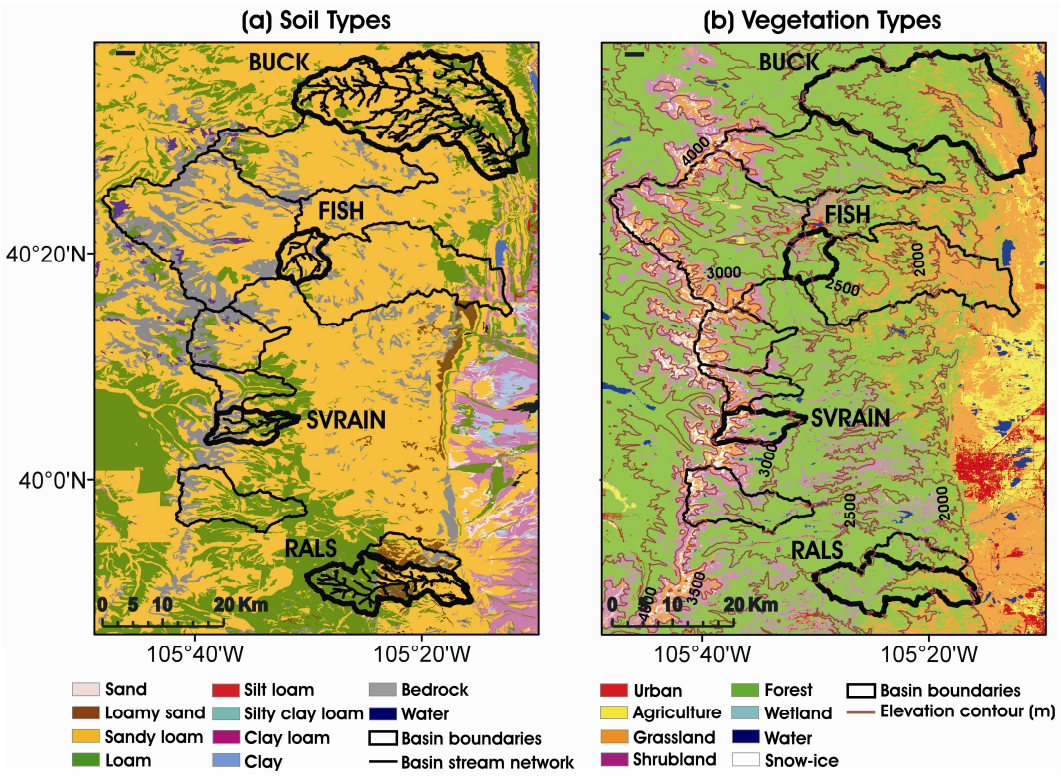

Figure 3.2. Spatial distributions of (a) soil types and (b) vegetation classes across the CFR. Elevation contours and basin stream networks for the selected watersheds are also shown.

Regional Radar Rainfall Data and *Z*-*R* Relations

Radar volume scan reflectivity observations were obtained from the NEXRAD WSR-88D radars at Denver, CO (KFTG), Pueblo, CO (KPUX) and Cheyenne, WY (KCYS). Level II conical scans were then converted to constant altitude plots over minimum and maximum scan altitudes of 3-km and 6-km, respectively.

Table 3.1 Description of hydrologic model inputs and sources.

Information type	Resolution	Source	References
Digital Elevation Model	30 m	National Elevation Dataset	Gesch et al. (2002)
Soil Texture Maps	30 m	Soil Survey Geographic, State Soil Geographic	Wang and Melesse (2006)
Vegetation Types	30 m	USGS National Land Cover Dataset	Homer et al. (2004)
Rain Gauge and Weather Data	1 hour	Mesowest and AMERIFLUX networks	Steenburgh (2003), Horel et al. (2002), Lazarus et al. (2002)
WSR-88D NEXRAD Level II	5 min, 1 km	NWS Doppler Radar Network	Kelleher et al. (2007).
Streamflow Data	1 hour	Colorado Division of Water Resources	Moreno et al. (2012a)

Reflectivity values from the 3 radars were then mosaicked together and transformed to 5-minute, 1-km resolution rainfall rates by selecting different *Z-R* relations from feasible ranges of *A* and *b* found in the literature (see Table 3.2; Morin et al. 2006; Nykanen et al. 2007; Habib et al. 2008; Vieux et al. 2009) and accumulated to hourly amounts. A hail threshold of 53 dBZ was applied and reflectivity values below 10 dBZ were designated as having a rain rate equal to zero. Hourly rain gauge data from seven sites were used to compute error and skill metrics at collocated pixels with the radar product for summer (JJAS) 2004.

A subsequent analysis was conducted to derive the most appropriate *Z-R* relation by minimizing the sum of Root Mean Square Errors (*RMSE*) and maximizing the mean Critical Success Indexes (*CSI*) (Wilks 2005) of precipitation series at the seven rain gauges and Level II collocated pixels. Equation (3.1) defines *RMSE*.

Table 3.2 List of *Z-R* relations found in the literature.

Z-R	Source
$Z=200R^{1.6}$	Marshall and Palmer (1948)
$Z=300R^{1.4}$	Fulton et al. (1998)
$Z=300R^{1.5}$	Joss and Waldvogel (1970)
$Z=79.1R^{1.81}$	Alfieri et al. (2010)
$Z=250R^{1.2}$	Vieux and Bedient (1998)
$Z=421R^{1.57}$,$Z=111R^{1.61}$,$Z=58R^{1.77}$, $Z=165R^{1.41}$,$Z=303R^{1.48}$,$Z=246R^{1.54}$, $Z=280R^{1.4}$,$Z=156R^{1.48}$, $Z=337R^{1.39}$	Habib et al.(2008)
$Z=250R^{1.4}$,$Z=75R^{1.75}$	Bouilloud et al. (2009)
$Z=486R^{1.37}Z=31R^{1.7}$,$Z=313R^{1.25}$	Prat and Barros (2009)
$Z=655R^{1.4}$	Morin et al. (2006)
$Z=250R^{1.2}$	Vieux et al. (2009)

$$RMSE_i = \sqrt{\frac{1}{N}\sum_{t=1}^{N}\left(P_t^i - R_t^i\right)^2} \tag{3.1}$$

where P_t^i and R_t^i denote respectively Level II and rain gauge simultaneous observations, at hour t and rain gauge site i. Complementarily, Equation (3.2) defines CSI from contingency tables that allow extracting categorical variables.

$$CSI_i = \frac{h_i}{(h_i + f_i + m_i)} \tag{3.2}$$

where h_i, f_i and m_i represent the number of successes, false alarms and misses when Level II precipitation values are used to predict the occurrence or not of rainfall at specific rain gauge sites i. The objective function (I), represented by equation (3.3),

$$I(A,b) = \frac{1}{2}\left[\left(1 - \frac{sum(RMSE_i)}{\max(sum(RMSE_i))}\right) + \left(\frac{mean(CSI_i)}{\max(mean(CSI_i))}\right)\right]$$
$$I(A,b) = \frac{1}{2}\left[f_1(A,b) + f_2(A,b)\right] \quad (3.3)$$

is thus maximized to obtain the best fit values of A and b. I balances the two metrics since *RMSE* weights the presence of large precipitation differences, whereas *CSI* emphasizes the number of matching events. The variations of f_1, f_2 and I with A and b are presented in Fig. 3.3 as two-dimensional contour plots (This type of plot is used frequently in subsequent analyses). Notice how the f_1 surface gradient decreases as both A and b grow. Additionally, the range of f_2 is smaller than f_1 and depends primarily on b. The exponent b controls the rate of change of the *Z-R* transformation in the logarithmic space and is commonly related to the type of originating rainfall system (e.g., summer convective or winter stratiform; Morin et al. 2006; Habib et al. 2008). The two functions f_1 and f_2 exhibit a complementary behavior. High values of the *Z-R* coefficient and exponent result in low *RMSE*, but at the expense of an increased number of false alarms and thus lower *CSI*. This is due to the prevalent overforecasting characteristic of small-depth precipitation events by Level II that are rather not captured by the rain gauges.

We replicated this exercise for summers (JJAS) in 2005 and 2006 using the same rain gauges and found a similar functional surface for I. The consistency among summers suggests that an appropriate seasonal *Z-R* relation might be in the region of $600 \leq A \leq 700$ and $1.1 \leq b \leq 1.4$.

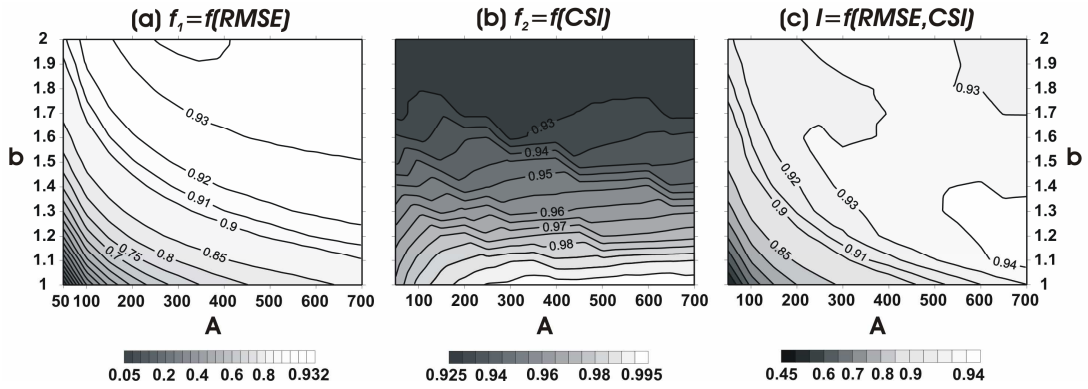

Figure 3.3. Contour lines of (a) f_1, (b) f_2 and (c) I functions for different combinations of coefficient (A) and exponent (b) for summer 2004 relative to hourly rain gauges in the CFR.

As a result, a single seasonal relation, $Z=700R^{1.3}$, was selected as a "reference" case to generate rainfall fields for the CFR region and calibrate the hydrologic model. We acknowledge that the selection of this reference *Z-R* relation is influenced by the objective function and that different functions may well lead to different 'optimal' values. However, for the purposes of this study, this procedure provides a fairly simple, quantitative and objective method from which we can explore the impact of rain rate estimation errors on simulated hydrologic responses. Several other reasons support the use of a single *Z-R* seasonal relation: (1) Single relations are of practical applications by river forecasting centers, (2) the similar topographic and landcover characteristics in a compact mountain block, (3) the capture of both storm and inter-storm periods that are important in hydrologic modeling, (4) the presence of summer convection as one of the main rainfall generation mechanisms and (5) the establishment of a fair comparison between reference and default operational *Z-R*s.

Distributed Hydrologic Modeling

We use the tRIBS distributed hydrologic model to investigate the uncertainty introduced by different *Z-R* relations in four headwater basins. tRIBS has been tested for continuous flood forecasting in different regions (e.g., Vivoni et al. 2007b; Mascaro et al. 2010; Nikolopoulus et al. 2011), including the CFR (Moreno et al. 2012a). The model is able to ingest spatially-varying terrain, soil and vegetation fields (e.g. Table 3.1) as well as meteorological forcing to represent the surface-subsurface moisture dynamics within a system of interconnected hillslopes and channel reaches. Given its distributed nature, tRIBS recognizes non-uniform surface properties represented by model parameters, per information layers (e.g. soils, vegetation, topography, channel network) that drive the energy and water balance equations at each computational element. Elements consist of sloped columns of heterogeneous, anisotropic soil with an exponential decay in saturated hydraulic conductivity (Beven 1982; Vivoni et al. 2007a). Vadose zone dynamics is represented through infiltration fronts, water table fluctuations and moisture losses due to evapotranspiration. A kinematic approximation for unsaturated flow is used to compute infiltration and propagate moisture fronts in the soil column (Cabral et al. 1992; Garrote and Bras, 1995; Ivanov et al. 2004; Vivoni et al. 2007a). Lateral moisture redistribution in the vadose zone and shallow aquifer are driven by gradients in surface and groundwater topography. Water table dynamics is computed from groundwater fluxes, vertical recharge and exfiltration. Surface runoff is produced by infiltration-excess (INF), saturation-excess (SAT), groundwater exfiltration (GW)

and perched return mechanisms, while routing is carried out by hydrologic hillslope and hydraulic channel approaches. An important model characteristic is the use of a TIN to represent a complex basin and reduce the number of computational nodes relative to the original data with minimal loss in terrain information (Vivoni et al. 2004). Additional details on the model characteristics and formal numerical framework are provided in Ivanov et al. (2004), Vivoni et al. (2004), Vivoni et al. (2005) and Vivoni et al. (2007b).

Model parameters describing the soil, vegetation, channel network and subsurface aquifer control the hydrologic response to storm and interstorm periods. Table 3.3 describes the basin topography, soils, vegetation and their associated model parameters obtained from Moreno et al. (2012a), who conducted a calibration strategy using a combination of manual and automated approaches. Calibration was made independently for each basin using the Level II product and the reference relation, $Z=700R^{1.3}$. The calibration method minimized the RMSE of observed and simulated outlet hydrographs at hourly time steps. Fig. 3.4 presents calibrated and observed cumulative hydrographs in each basin. RMSE and Nash-Sutcliffe Efficiency (NS) values confirm that the distributed model is able to capture the different basin responses fairly well, with positive NS obtained at BUCK (0.48), FISH (0.50) and SVRAIN (0.53), although weaker values are found at RALS (-0.54). Negative NS values are a consequence of model structural errors and uncertainties introduced by the rainfall forcing and streamflow data.

Table 3.3. Terrain and channel network characteristics and calibrated (*) parameter values for the watersheds.

Property/Paramete	Buckhorn Creek		Fish Creek		South Saint Vrain Creek		Ralston Creek	
ID	BUCK		FISH		SVRAIN		RALS	
Stream Gauge ID	BUCRMVCO		FISHESCO		SSVWARCO		RALCRKCO	
Total Area [km^2]	350.5		40.8		35.1		117.3	
Length of main channel [km]	45.6		9.7		12.6		25.8	
Slope of main channel [m/km]	26.2		70.5		42.3		32.1	
Mean elevation [m]	2418		2858		3455		2517	
Minimum/maximum elevations [m]	1583/3268		2284/3473		2858/4087		1847/3204	
Std. Elevation [m]	482		333		344		387	
Mean slope [%]	28.0		28.2		30.0		29.2	
Std. Slope [%]	16.3		19.9		26.7		17.9	
Non-linear discharge exponent, r [-]*	0.4459		0.4491		0.4074		0.4340	
Bedrock depth, B [m]*	1.26		1.05		2.84		1.66	
Mean depth to groundwater, $\mu(N_{wt})$ [m]*	1.17		1.01		0.169		1.28	
Soil cover [%]	Sandy loam (75%)	Loam (21%)	Sandy loam (87%)	Bedrock (7%)	Sandy loam (44%)	Loam (31%)	Loam (46%)	Sandy loam (34%)
Sat. hydraulic conductivity, K_s [mm/h]*	7.96	30.29	17.18	2.04	8.16	22.38	25.76	18.64
Soil moisture at saturation, θ_s [-]*	0.32	0.37	0.35	0.07	0.57	0.56	0.52	0.58
Pore size distribution index, λ_0 [-]*	0.81	1.46	1.47	0.06	1.48	0.58	1.67	1.19
Air entry bubbling pressure, ψ_b [mm]*	-244.2	-704.5	-84.36	-221.89	-21.71	-804.97	-385.37	-324.37
Conductivity exponent decay, f [mm^{-1}]*	0.0334	0.0253	0.00222	0.03063	0.00037	0.00096	0.03655	0.00845

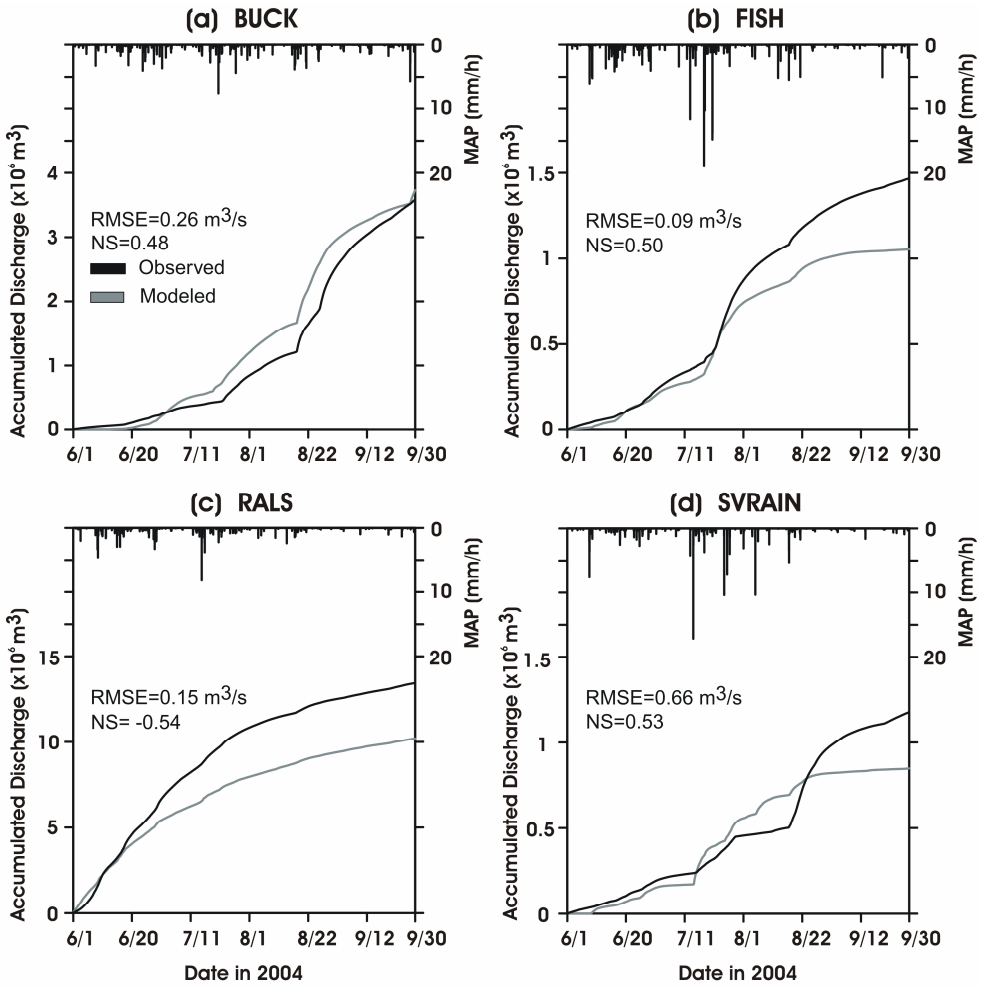

Figure 3.4. Observed (black lines) and simulated cumulative hydrographs (dark gray lines) resulting from model calibration in each basin, with NS and RMSE skill scores. Mean areal precipitation (MAP) is derived from the hourly, 1-km Level II product using the reference *Z-R* relation.

RESULTS AND DISCUSSION

Sensitivity of Integrated Hydrologic Response

The watershed responses resulting from the sampled *Z-R* relations are compared in terms of the outlet streamflow, the underlying runoff mechanisms and the water balance components. Fig. 3.5 presents the performance of the outlet

streamflow against the observed hydrographs as contour lines of three skill metrics in the *A* and *b* space: Root Mean Square Error (RMSE), streamflow Volume Bias and Pearson Correlation Coefficient. Although it is well known that the *Z-R* transformation obeys to a non-linear relation, hydrologic responses could not necessarily preserve both error and correlation structures when compared to rainfall estimations independently. Three points have been added for comparison purposes: the reference (rain gauge calibrated, $Z=700R^{1.3}$), WSR-57 ($Z=200R^{1.6}$) and NEXRAD ($Z=300R^{1.4}$) relations. A few simulations in BUCK with low values of *A* are missing due to the excessive computational demands for cases with unreasonably high runoff generation (and excluded from further analysis). The three metrics are complementary and help identify the impact of the *Z-R* relation on the integrated basin response: RMSE that weights streamflow peak errors more heavily, Volume Bias that provides fraction of simulated to observed seasonal discharge volumes and the Correlation Coefficient that indicates the degree of temporal agreement of simulated and observed hydrographs over the entire time series.

In general, white areas and the dashed boxes in Fig. 3.5 correspond to good performances for each metric (i.e., low RMSE, Volume Bias near unity, high Correlation). Better performance is found in a region in the vicinity of high *A* and *b* that tend to produce smaller runoff volumes (Bias less than one). In contrast, areas with darker shades associated to poorer performance are generally linked to a combination of low *A* and low *b* values with excessive streamflow that overestimate total discharge volumes (Bias much greater than one).

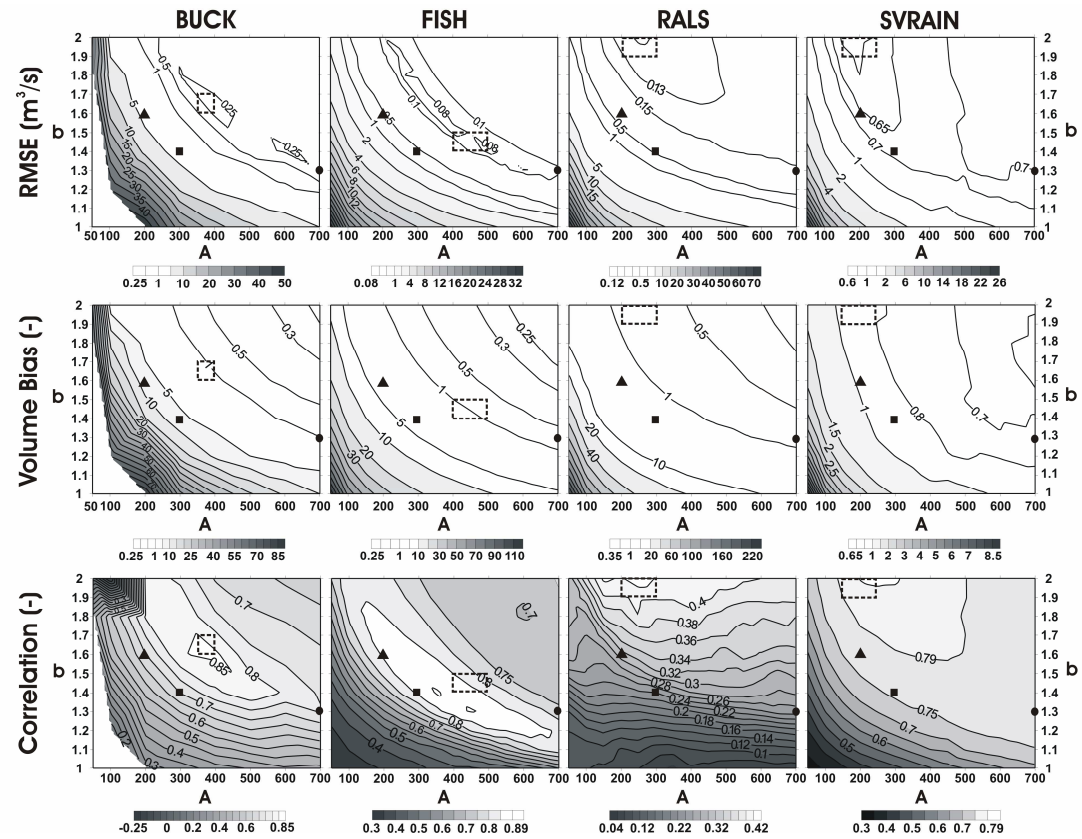

Figure 3.5. Contour lines of streamflow metrics at BUCK, FISH, RALS and SVRAIN for different *A* and *b* values. Locations of the reference (circle), WSR-57 (triangle) and NEXRAD (square) relations are shown.

The resulting hydrologic uncertainties and skills correspond well to the objective function (*I*) of the radar rainfall errors (Fig. 3.3c) for different *Z-R* relations, in particular for streamflow RMSE and Volume Bias. In most cases, the reference (circle), WSR-57 (triangle) and NEXRAD (square) relations lie near areas of good performance, but the WSR-57 and NEXRAD relations overestimate discharge volume (Bias greater than unity) and have poorer performance (higher RMSE) than the reference relation, except in SVRAIN where snowmelt drives the basin response (Moreno et al. 2012a). This basic analysis suggests that

operational *Z-R* relations are capable of introducing considerable uncertainty in flood forecasts for the CFR.

Differences in the magnitude and spatial distribution of rainfall from each *Z-R* relation may also condition the runoff mechanisms in the basins. Fig. 3.6 presents the fraction of the outlet streamflow volume from each runoff type. The triangular legend shows combinations of the three dominant mechanisms (with vertex colors): INF (red), SAT (green) and GW (blue). Differences in basin properties and model parameters yield variations in the runoff composition across basins, with BUCK and RALS consisting primarily of INF and SAT, SVRAIN composed of GW and SAT, and FISH having a mixture of all types but mostly GW and SAT (Moreno et al. 2012a). The precipitation forcing from each *Z-R* relation leads to variations in the contributed proportions. Generally, low values of *A* and *b*, resulting in large rainfall volumes, tend to increase saturation-excess runoff (SAT) as the wetter systems develop shallower water tables that interact with the surface, particularly near channels. In contrast, high values of *A* and *b* do not seem to introduce large changes in runoff generation mechanisms at BUCK, SVRAIN and RALS, indicating that rainfall underestimation is not a significant factor for changing the type of prevalent runoff mechanism in these basins. At FISH, however, high values of *A* and *b* lead to a slight decrease of both INF and GW due to less intense rainfall events and a diminished recharge. Across all basins, the reference and operational *Z-R* relations (WSR-57 and NEXRAD) produce similar runoff mechanism proportions, despite their differences in streamflow RMSE.

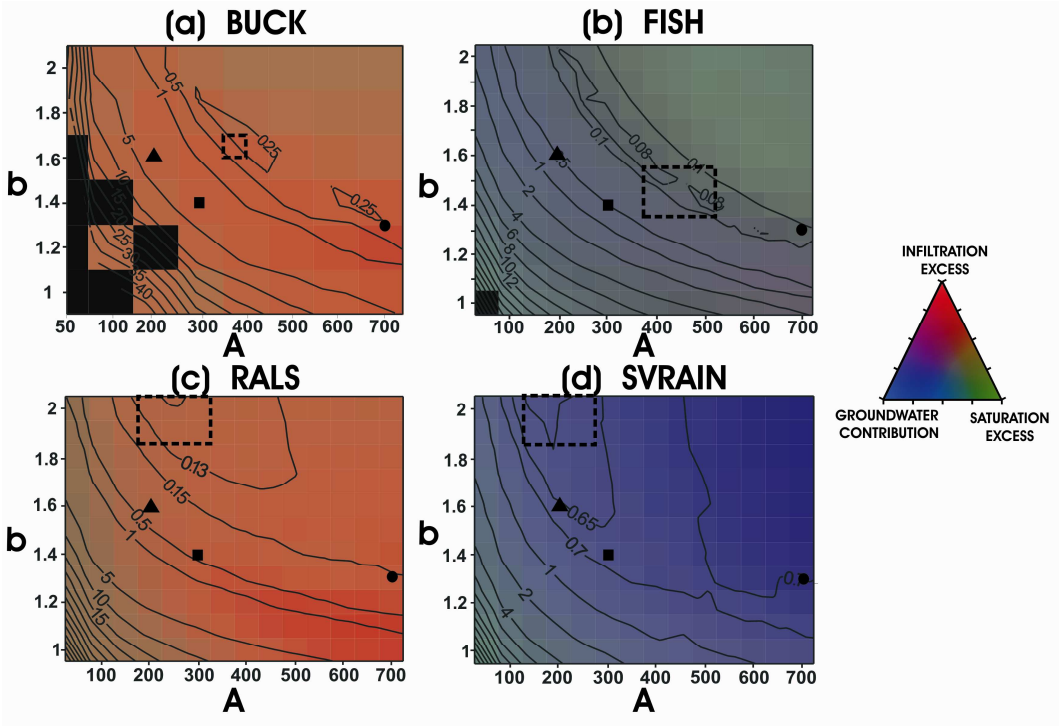

Figure 3.6. Fractions of runoff mechanisms for each *Z-R* relation at the four basins represented by color combinations. Contour lines corresponding to RMSE are shown for reference. Except in FISH (A=50, b=1) where it reaches 99%, the perched return contribution is <3% and is excluded.

The seasonal water balance may also vary according to the precipitation forcing from the different *Z-R* relations. Fig. 3.7 presents contour lines of water balance components ($\Delta S/\Delta t = P - ET - R$) as a function of A and b for the simulations (Δt = 4 months), where ΔS is the change in storage estimated from basin-averaged precipitation (P), evapotranspiration (ET), and outlet streamflow (R). Reference values for each water balance component correspond to black circles in Figure 3.7. Due to the increased energy availability during the summer season at low and mid elevation lands (e.g. BUCK FISH, RALS), ET_{ref} tend to present similar or slightly larger values than P_{ref}. Thus, negative changes in storage are required to supply a fraction of the high atmospheric demand.

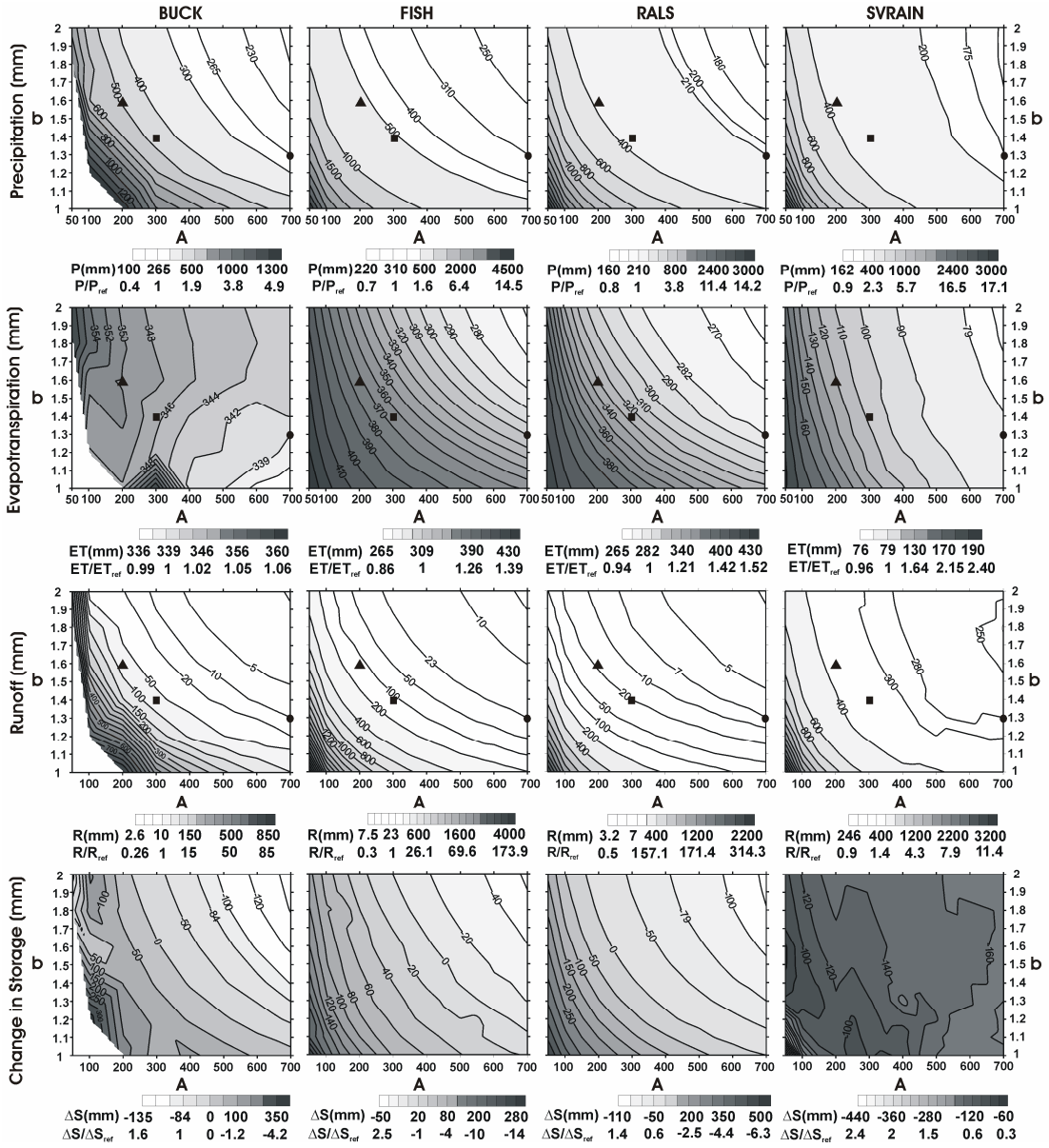

Figure 3.7. Contour lines of seasonal water balance components for different (*A*, *b*) combinations: precipitation (*P*), evapotranspiration (*ET*), runoff (*R*) and change in storage (Δ*S*). Two gray scales are provided: actual values (in mm) and fraction of the reference (ref) value (-). Contour lines are labeled with the actual values.

Consistently, values of R_{ref} show that, except by SVRAIN where snow melting processes prevail and R_{ref} exceeds P_{ref}, runoff production during the summer season is, in average, smaller than ET_{ref} by one order of magnitude.

Variations of P and R in the A and b space follow the patterns identified in the streamflow evaluation: (1) overestimation of P and R for low A and b, and (2) underestimation of P and R for high A and b. This is more clearly observed by inspecting the scale of P/P_{ref} and R/R_{ref}, where P_{ref} and R_{ref} are values for the reference relation. Overall P/P_{ref} ratios are one order of magnitude smaller than R/R_{ref} showing that changes in precipitation induced by different Z-R are significantly magnified by watershed changes in streamflow. Variations in ET exhibit different patterns for each basin and a lower range of difference (ET/ET_{ref} ranges from 0.86 to 2.40 across basins) in these mountain settings. As a result, ΔS is typically positive in areas of low A and b (water is accumulating in the subsurface during season) and negative in regions of high A and b (subsurface water is decreasing). SVRAIN has a different behavior, with relatively low ET, high R and negative ΔS, as this high-altitude basin has a strong snowmelt component during the summer (Moreno et al. 2012a), with typically cooler summer temperatures and, generally, a lower evaporative demand. An inspection of the operational Z-R relations indicates that WSR-57 and NEXRAD relations exhibit increased P that is seldom completely consumed by ET and whose remnant is converted into R and ΔS.

Radar Rainfall Error Propagation to Hydrologic Response

The propagation of errors introduced by the Z-R relation into the hydrologic response of each basin is assessed relative to the reference case. Fig. 3.8 presents the variation of a streamflow metric, q_r, obtained as the outlet discharge RMSE between each Z-R relation and the reference case with a rainfall

metric, m_r, defined in a similar fashion for the mean areal precipitation. Thus, each point represents the error of each *Z-R* relation with respect to the reference case, used here as a point of comparison since it was derived via calibration with rain gauges. For each basin, a power law regression of the form $q_r = Um_r^v$ is fitted to N points above a threshold in hydrologic uncertainty (q_r), represented by the dashed lines. Points excluded from the regression (below the threshold lines), whose q_r are smaller or equal than values provided by the reference *Z-R* relation, produce hydrographs that can be divided into two groups: (1) those with a small m_r, since A and b are close to the reference case, and (2) those with a larger m_r due to high A and b values, but whose streamflow errors are dampened by model parameters and initial conditions. For the remaining N points, a simple scaling regression that minimizes residual errors between adjusted line and raw data, indicates that rainfall uncertainties are logarithmically transmitted to streamflow errors. The slope of the relation between m_r and q_r has a limited range of v = 1.18 to 1.51 across all basins despite their different conditions. Values of v greater than unity indicate that hydrologic uncertainty (e.g., streamflow errors introduced by the *Z-R* relation) is amplified relative to the rainfall errors, with a greater nonlinearity above the threshold q_r present for the higher values of v in RALS and the lowest nonlinearity at SVRAIN.

Since hydrologic uncertainties are typically larger for flood events, it is useful to identify how streamflow errors vary with discharge magnitude.

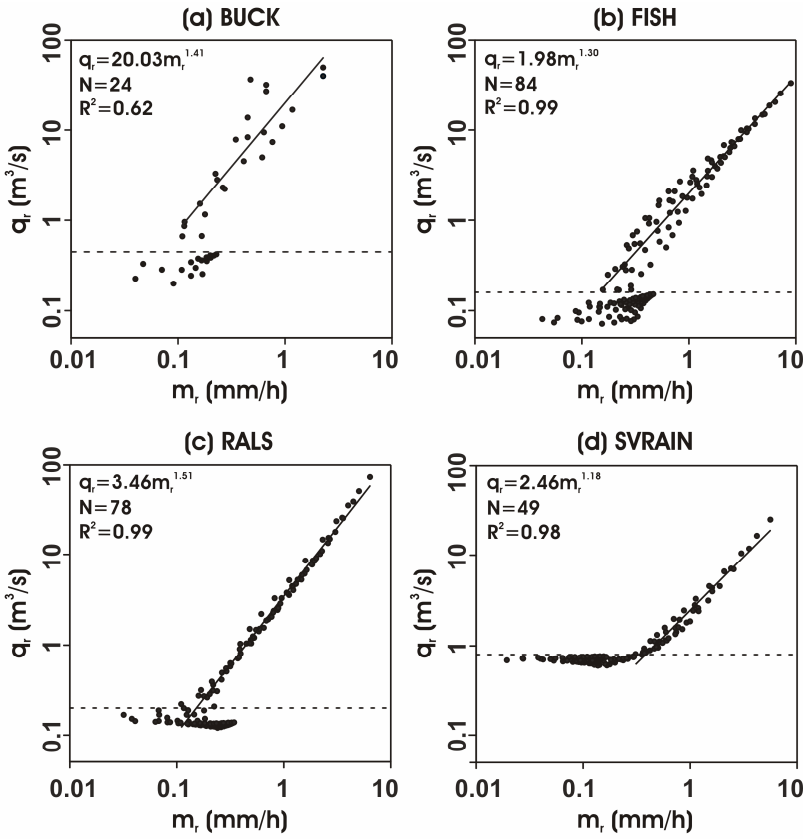

Figure 3.8. Scatterplots and power law regressions between RMSE of mean areal precipitation (m_r) relative to the reference case and RMSE of outlet streamflow (q_r) relative to the reference case for *A* and *b* combinations. Horizontal dashed lines are drawn to separate *Z-R* relations that do not represent large changes in streamflow errors. Values below that threshold are not considered.

Fig. 3.9 presents scatterplots of the daily (24-h) streamflow errors, q_{24r}, of three *Z-R* relations (WSR-57, NEXRAD and an extreme case of $Z=200R^{1.0}$ that overestimates precipitation) with respect to the reference case. Streamflow errors are organized as a function of the maximum daily discharge, q_m, such that each point represents a different day in the season. Several mathematical adjustments were tried but as data pairs (q_m, q_{24r}) span several orders of magnitude, power law regressions resulted in better performances to relate these two variables..

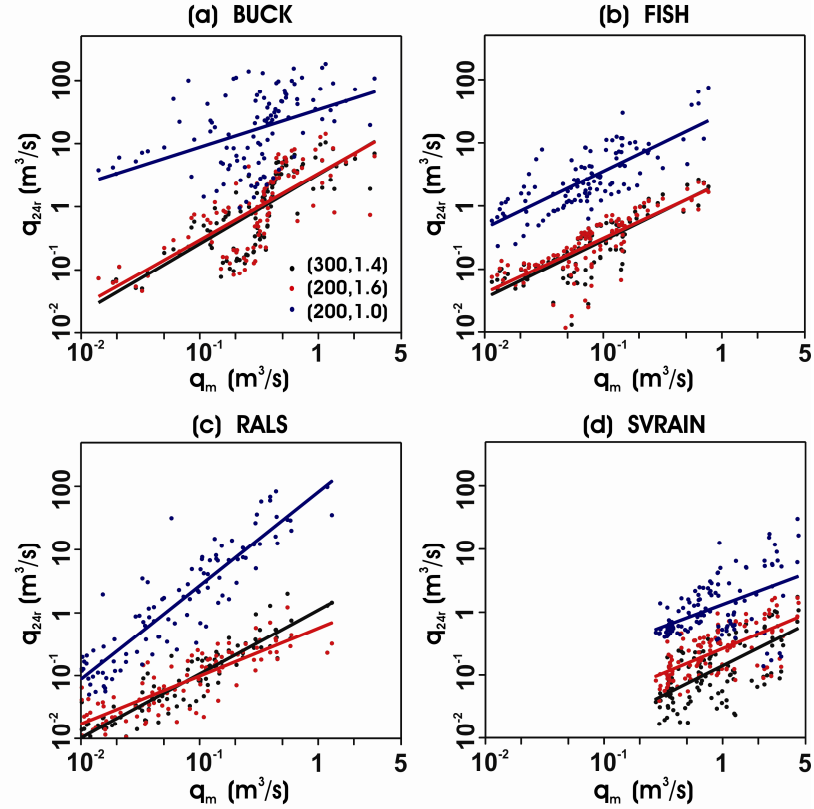

Figure 3.9. Scatterplots and power law regressions between the maximum daily discharge (q_m) and the daily RMSE of reference and simulated hydrographs (q_{24r}) using NEXRAD (black), WSR-57 (red) and an extreme case, $Z=200R^{1.0}$ (blue).

Parameters (λ,ϕ) of relations in the form $q_{24r} = \lambda q_m^{\phi}$ are found for each *Z-R* that minimize residual errors between data and adjusted regressions (see Table 3.4). The data suggest that the streamflow uncertainty introduced by the *Z-R* relations follows a power law regression with q_m, but whose R^2 evidence data dispersion and poor adjustments in several cases (except for FISH where q_m is a good predictor of daily errors consistently across *Z-R* relations). Overall, data distribution indicates that errors introduced by the *Z-R* relation increase when forecasting floods of higher magnitudes during the summer season.

Table 3.4. Coefficients (λ) and exponents (ϕ) of the power law regressions of the daily uncertainty and the maximum daily discharge ($q_{24r} = \lambda q_m^{\phi}$). The number of data points (N) and coefficient of determination of regression (R^2) are also reported.

	$q_{24r} = \lambda q_m^{\phi}$			
	λ	ϕ	N	R^2
BUCK				
A=300, b=1.4	3.245	1.099	110	0.37
A=200, b=1.6	3.355	1.053	110	0.27
A=200, b=1.0	34.32	0.594	110	0.17
FISH				
A=300, b=1.4	2.362	0.917	111	0.81
A=200, b=1.6	2.290	0.870	112	0.80
A=200, b=1.0	28.25	0.901	113	0.59
RALS				
A=300, b=1.4	1.103	1.017	92	0.67
A=200, b=1.6	0.570	0.764	99	0.41
A=200, b=1.0	81.08	1.483	104	0.47
SVRAIN				
A=300, b=1.4	0.140	0.942	121	0.50
A=200, b=1.6	0.263	0.784	121	0.45
A=200, b=1.0	1.324	0.696	121	0.35

Note that the WSR-57 and NEXRAD relations provide similar errors across the q_m range with exponents (ϕ) ranging narrowly from 0.78 to 1.1 in all basins (thus similar slopes). The extreme case ($Z=200R^{1.0}$) has the largest streamflow errors and most dissimilar exponents across the basins. Other *Z-R* relations that overestimate rainfall are expected to behave similar to the extreme case. These results support the notion that rainfall errors introduced by the *Z-R* relation propagate in a nonlinear fashion to the streamflow response, with higher impacts for larger flood events.

Distributed Hydrologic Response Errors at Seasonal and Event Scales

The spatiotemporal rainfall variability derived for each *Z-R* relation should also influence the distributed basin response which can be assessed in terms of the spatial patterns of runoff and the streamflow produced at internal locations. Fig. 3.10 shows correlation diagrams (ρ) of the spatial distribution of time-averaged runoff rate (mm/hr) between each *Z-R* relation and the reference case in each basin (Note that the lower number of points in BUCK is due to a sparser sampling of the *A* and *b* space due to computational limitations for the largest basin). The time-averaged runoff rate is obtained for periods when runoff is produced during the simulation (Ivanov et al. 2004). Positive correlations over the majority of the *A* and *b* space in all basins demonstrate that different *Z-R* relations produce similar time-averaged runoff patterns. High correlations ($\rho > 0.5$) tend to follow the patterns identified for the streamflow metrics (Fig. 3.5) with a better match in the upper left to the lower right portions of the *A* and *b* space. Weaker correlations ($0 < \rho < 0.2$) are found at low *A* and *b* for BUCK, RALS and SVRAIN indicating that spatial variations in runoff production occur for *Z-R* relations that overestimate rainfall. Similarly, FISH and RALS exhibit weaker correlations for high values of *A* and *b*, where rainfall is underestimated with respect to the reference case. Negative correlations in FISH denote severe changes in the presence of runoff patterns for low *A* and *b* as evidence of opposite spatial tends.

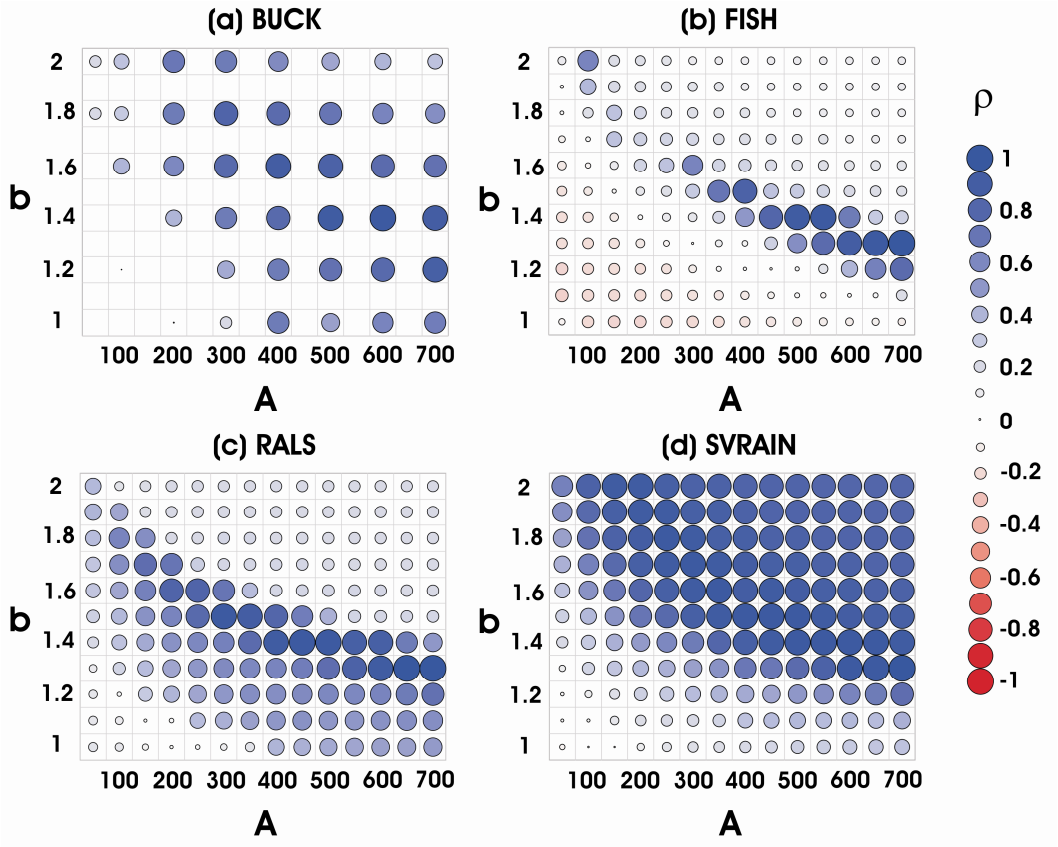

Figure 3.10. Correlation matrices between the spatial distributions of the time-averaged runoff rate from different combinations of *A* and *b* and the reference relation at the four study basins.

Discrepancies in the spatial runoff distribution may be due to either subtle variations in the geographic distribution of rainfall events for different *Z-R* relations or, more likely, changes in the rainfall magnitude for similar rainfall patterns. For example, the operational WSR-57 ($Z=200R^{1.6}$) and NEXRAD ($Z=300R^{1.4}$) relations show correlation values near unity, except in FISH where ρ is somewhat lower, while the extreme case ($Z=200R^{1.0}$) has large spatial differences in time-averaged runoff rate relative to the reference case.

Differences in runoff generation introduced by a *Z-R* relation can also lead to streamflow errors at internal channel locations that are characterized by an upstream basin area (Vivoni et al. 2007b). Fig. 3.11 presents streamflow differences, as a specific error (SE), in terms of an RMSE between simulated hydrographs of the NEXRAD relation (selected as an example) and those of the reference case, normalized by the basin area (A_c) and mean areal precipitation (MAP) as:

$$\mathrm{SE} = \frac{\mathrm{RMSE}}{A_c \mathrm{MAP}} \tag{3.4}$$

Selected sites have upstream areas ranging from 0.01 km^2 to the total basin area across a variety of different catchment properties. The scale dependence of SE reveals interesting patterns. At small A_c (0.01 to ~1% of total area), the low specific error is due to relatively large MAP that is unaffected by areal smoothing and a limited RMSE between the hydrographs forced by different *Z-R* relations. At intermediate A_c (up to ~10% of total area), increasing mean specific errors are observed along with larger variations that measure dispersion across basins of similar size. Intermediate-sized basins present a higher and more variable RMSE between the NEXRAD and reference *Z-R* relations, as well as a wider range of MAP as a result of areal smoothing of storms whose size typically does not cover the entire upstream area. At this scale, catchment properties play a determinant role in either amplifying or dampening precipitation errors (Mascaro et al. 2010b).

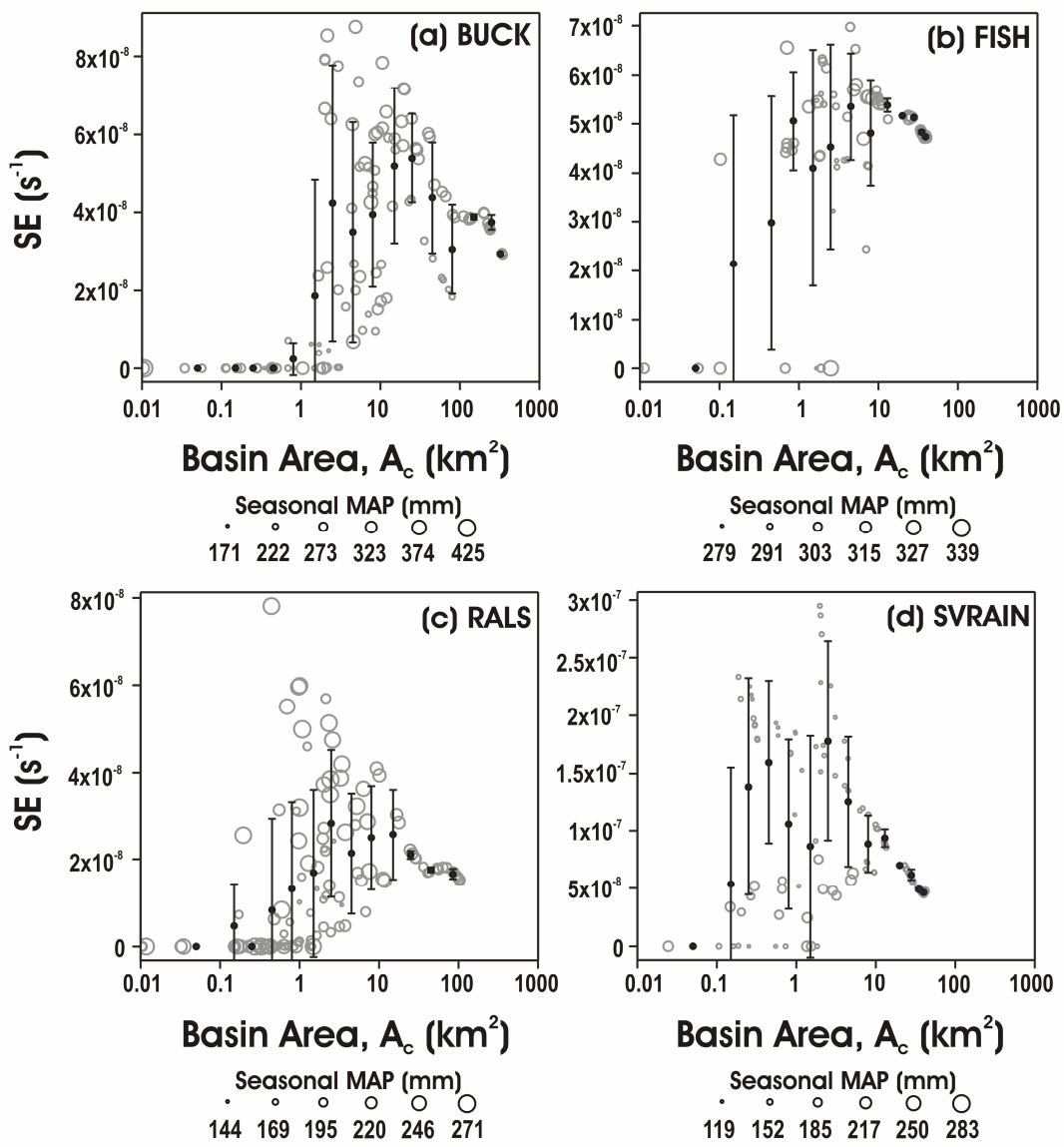

Figure 3.11. Seasonal relations between Specific Error and basin area in the four study basins. Raw data (gray circles) were bin-averaged (black dots and vertical bars as ±1 standard deviation). The symbol size indicates the seasonal mean areal precipitation (MAP).

At large A_c (10% to total area), low specific errors are caused primarily by how RMSEs are reduced due to the integration properties of large basins where the channel network transfer of the flood wave dominates the flood forecast skill

(Vivoni et al. 2006; Mascaro et al. 2010b). A similar outcome was obtained when comparing the WSR-57 and the reference case (not shown).

To further investigate the error scale dependence, Fig. 3.12 shows a comparison of rainfall and runoff distributions and streamflow hydrographs for a storm event on 18-19 August, 2004, in BUCK. Results are shown for the reference, NEXRAD, WSR-57 and extreme *Z-R* relations. For each case, spatial distributions correspond to the accumulations of 24-h rainfall and 87-h runoff production. In addition, hydrographs at four channel locations show internal variations associated with the mean areal precipitation in upstream areas, along with the basin outlet. Each *Z-R* relation produces comparable spatial rainfall patterns with maximum depths at storm cores on the western part of the watershed. Runoff production follows rainfall patterns well since BUCK has primarily infiltration-excess runoff (INF) with some contributions of saturation-excess runoff (SAT) along stream channels. Note that the flood forecasts at internal sites follow anticipated increases in streamflow for larger areas. Internal hydrographs are quite sensitive to the *Z-R* relation. For example, the NEXRAD relation exhibits 1.7 times more rainfall than the reference case, but 3 to 4 times greater streamflow for internal sites. Spatial differences in rainfall magnitudes introduced by the *Z-R* relation can be significant, as shown by the extreme case. These results indicate that, while sampling the *Z-R* relation may not fundamentally alter the spatial rainfall pattern, the variations in rainfall magnitude can generate large runoff differences that are amplified downstream in terms of their errors relative to the reference case.

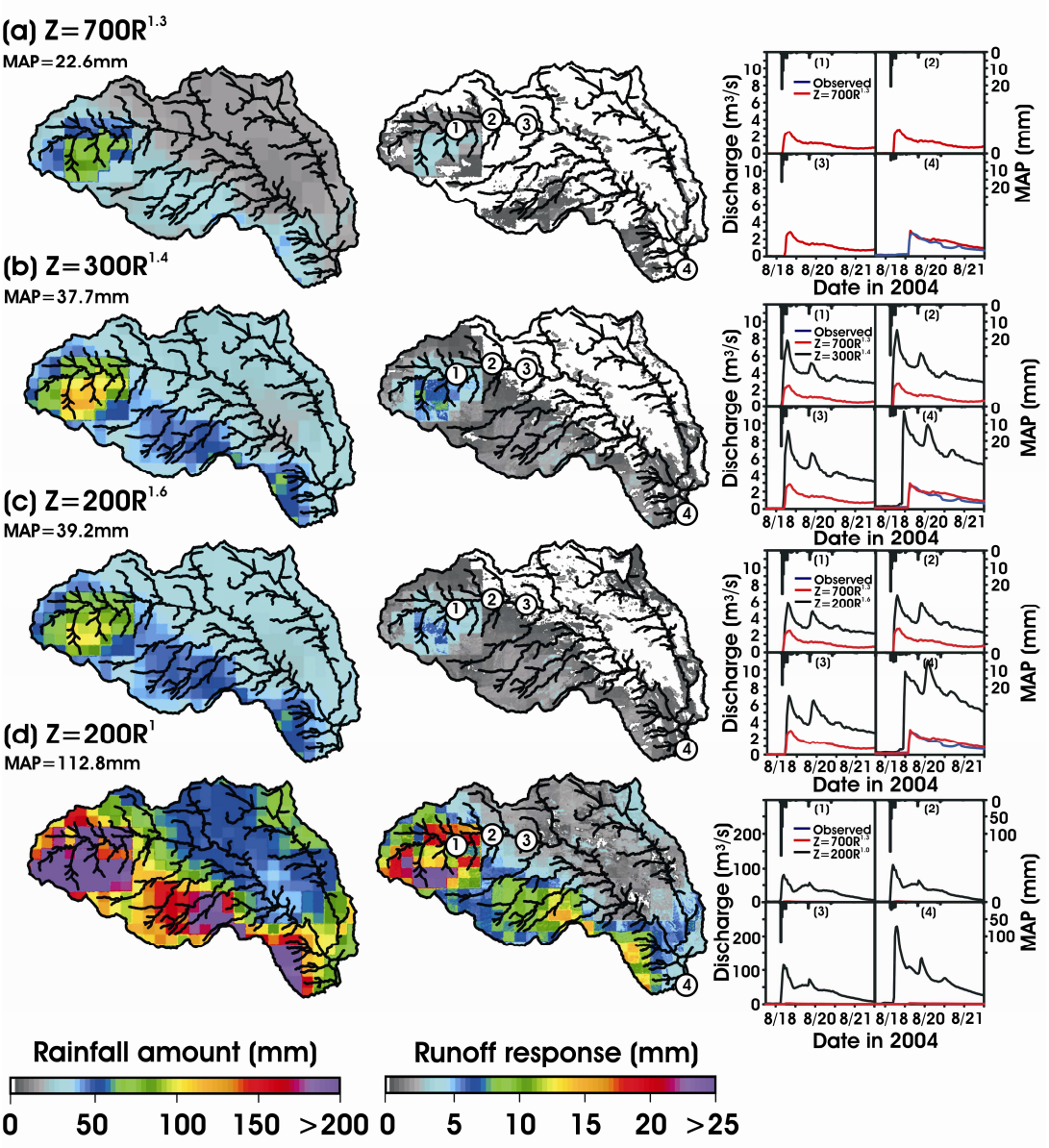

Figure 3.12. Spatial distribution of rainfall and runoff accumulations in BUCK for selected *Z-R* relations for 18-19 August, 2004 event. Mean areal precipitation and streamflow at three internal locations and the outlet are shown along with available observed hydrographs.

Lastly, Fig. 3.13 presents the variation of SE with basin area for the same storm event in BUCK.

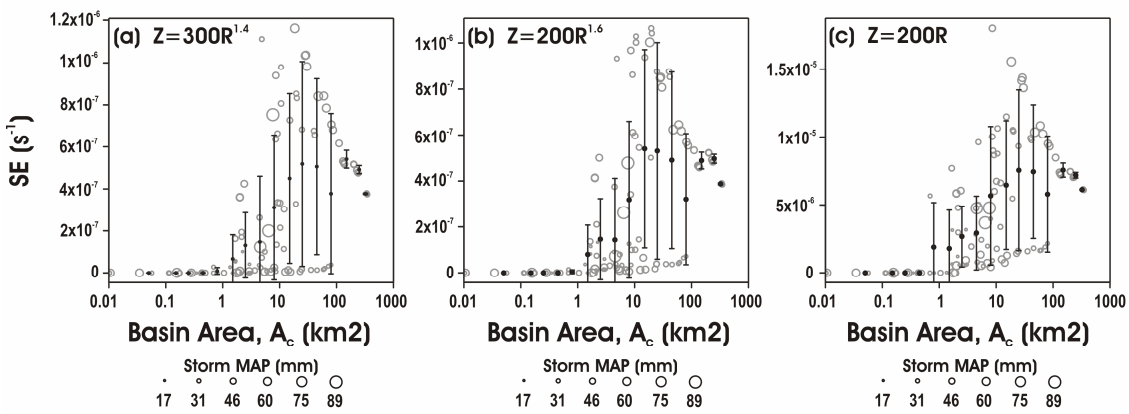

Figure 3.13. Storm relation between Specific Error and basin area for the August 18-19, 2004 event in BUCK. Raw data (gray circles) were bin-averaged (black dots and vertical bars as ±1 standard deviation). The symbol size indicates the storm mean seasonal precipitation (MAP).

Three selected *Z-R* relations are shown (NEXRAD, WSR-57 and extreme cases). At the event scale, the influence of MAP on SE is more clearly observed, as internal basins receive variable rainfall during the event, thus influencing the specific error. The characteristic patterns obtained for the seasonal case (Fig. 3.11) are replicated here, with higher SE for intermediate-sized basins and relatively lower SE for small and large areas. However, a separate type of scale dependence can be distinguished for a small cluster of sub-basins that retain a low SE over all areas. Thus, there are specific basin regions that not affected by the spatial rainfall distribution or have catchment properties that dampen the propagation of rainfall errors. Mascaro et al. (2010b) found a similar behavior in a different study site and attributed the effect to sub-basin properties that reduce peak runoffs such as high permeability, low slopes, and forested areas. When aggregated seasonally, however, the scale dependence of SE exhibits a smoother variation.

SUMMARY AND CONCLUSIONS

In this study, we investigated the propagation of errors from the specification of the *Z-R* relation to distributed flood forecasts in four mountain basins in the Colorado Front Range. The region is known to exert terrain controls on summer convection and possesses an appreciable number of flood events. Given the widespread use of radar-derived rainfall products by the hydrologic forecasting community, we postulated that use of an operational *Z-R* relation may introduce errors that decrease flood forecasting skill at outlet and internal locations. In evaluating the reflectivity-rainfall relations, we focused on the rainfall properties at rain gauge sites in the CFR; on the integrated hydrologic response, including the outlet discharge, runoff mechanisms and seasonal water balance; and on the distributed streamflow responses at internal locations. An emphasis was placed on identifying how distributed rainfall errors propagate to the distributed basin response by identifying the existence of relations with the mean areal precipitation, maximum daily discharge and catchment scale. This was performed to generalize our results beyond single polarization radar observations in the anticipation of new techniques or correction methodologies (e.g., dual-polarization radar). The results from the study indicate the following:

(1) Calibration of the reflectivity-rainfall relation using ground rain gauges resulted in an adequate rainfall performance over a range of *A* and *b* values. We found a seasonal *Z-R* relation, $Z=700R^{1.3}$, that is valid for summer convective events in the CFR over the three tested seasons.

(2) The rainfall properties of each *Z-R* relation impact the basin response in terms of the outlet streamflow, runoff mechanisms and the seasonal water balance. Rainfall differences in the WSR-57 and NEXRAD relations, relative to the reference case, result in higher streamflow errors, gradual transitions in runoff mechanisms, and large changes in the water balance. While calibrating the model to a different *Z-R* relation may mitigate this behavior to some degree, our analysis supports this finding since the reference *Z-R* case used was objectively selected.

(3) Errors in mean areal precipitation propagate to streamflow errors following a power law regression beyond a particular threshold. Similarly, streamflow uncertainty is described by a power law regression with discharge magnitude. Both relations indicate that errors introduced by the *Z-R* relation into the basin response are exacerbated for large rainfall or flooding events.

(4) The *Z-R* relation impacts the spatial distribution of the basin response, including time-averaged and event runoff patterns as well as the discharge at interior locations. Examples from the WSR-57, NEXRAD and extreme case relations indicate increased spatial runoff production and higher streamflow at both internal and outlet locations, relative to the reference case.

(5) A characteristic pattern was revealed for the scale dependence of specific errors in the three *Z-R* relations relative to the reference case for seasonal and event time scales. Intermediate-sized basins have higher and more variable SE due to the similar spatial storm scale and the influence of catchment properties on the propagation of rainfall errors into streamflow.

The results of this study are based on the use of a distributed hydrologic model calibrated during a summer season using a single-polarization Level II NEXRAD 1-km, hourly product with a reflectivity-rainfall relation obtained from comparisons to rain gauges. Since hydrologic differences exist between the study basins, model calibration was performed independently for each watershed. While the model calibration was conditioned on the reference *Z-R* relation, the sensitivity to precipitation forcing is sufficiently strong to outweigh the confounding effects of uncertainty in the model parameters and initial conditions. The distributed model was then used to study the propagation of errors introduced by sampling different *Z-R* relations relative to observed streamflows and a reference simulation considered as the spatially distributed "ground truth". Overall, the study illustrates that a distributed hydrologic model can serve as a useful verification tool of quantitative precipitation estimates (Moreno et al. 2012a), in this case focused on the appropriate *Z-R* relation for this mountain setting. We highlight that specific streamflow errors exhibit a pattern in scale dependence and that the use of an inappropriate *Z-R* relation primarily impacts intermediate-sized internal basins as compared with the spatial scale of the precipitation events. Such scaling behavior may change somewhat for different types of precipitation events in this and other regions, but presents insights into the prediction the flood forecast errors as a function of basin area. We conclude that flood forecasting efforts with radar forcing in mountain watersheds benefit from establishing a site-specific *Z-R* relation for the season of interest using comparisons with local observations. Use of a locally-calibrated *Z-R* relation,

even if derived from a few seasons of data, should significantly reduce the precipitation uncertainties associated with the *Z*-*R* relation and how these propagate to the basin response.

Chapter 4

SPATIOTEMPORAL LIMITS TO FLOOD FORECASTING IN MOUNTAIN CATCHMENTS UNDER SUMMER CONVECTION USING RADAR NOWCASTING AND A DISTRIBUTED HYDROLOGIC MODEL

INTRODUCTION

Flood predictability in mountain watersheds is challenging due to our limited capacity to accurately forecast precipitation in time and space, the short response time of watersheds, and the inherent uncertainties present in hydrologic modeling. Nevertheless, the use of Quantitative Precipitation Forecasts (QPFs) in hydrologic models of these settings can potentially improve streamflow predictions, as in other regions (Pessoa et al. 1993; Warner et al. 2000; Collier 2000; Berenguer et al. 2005; Vivoni et al. 2006; Chiang et al. 2007; Collier et al. 2007). When QPFs are unavailable, the maximum lead time for flood warnings is the basin response time, a value dependent on the watershed characteristics and antecedent soil moisture conditions. Nonetheless, the expected hydrologic gains in prediction time from QPFs are limited by the quality of forecasted fields. Under warm-season convection, the short life span and rapid evolution of these systems dictates the accuracy of rainfall forecasts at different lead times (e.g., Ganguly and Bras 2003; Lin et al. 2005; Sharif et al. 2004). Thus, uncertainty about future rainfall distribution could limit our ability for flood forecasting due to the sensitivity of runoff production to rapidly-changing precipitation fields (Vivoni et al. 2006; Reed et al. 2007; Moreno et al. 2012a).

For warm-season convective systems, radar nowcasts at short lead times (0 to 3 h) are often found to be the most skillful method for producing QPFs at high spatiotemporal resolutions (e.g., Collier 1991; Golding 2000; Ganguly and Bras 2003). The term radar nowcasting refers to a number of different algorithms that utilize sequences of rainfall fields to derive storm motion vectors applied to subsequent imagery (e.g., Dixon and Wiener 1993; Ganguly and Bras 2003; Bowler et al. 2004; Li and Lai 2004; Vivoni et al. 2006; Van Horne et al. 2006; Mass 2012). Several techniques are able to compute storm growth, movement and dissipation, while providing quantitative measures of precipitation amounts. The availability of weather radar networks has expanded the applications of nowcasting techniques, primarily for regions where the errors from Quantitative Precipitation Estimates (QPEs) are well understood (Berenguer et al. 2005; Sharif et al. 2006). In mountainous areas, however, challenges remain in the derivation of radar-based QPEs (e.g., Yates et al. 2001; Verbunt et al. 2007; Moreno et al. 2012a) and thus in the use of radar nowcasting techniques for predicting the timing, location and magnitude of precipitation as input to hydrologic models. Uncertainties inherent in QPFs are a consequence of the difficulty to forecast rainfall fields for extended periods given that extrapolation functions lose their correlation structures at large lead times (e.g., Sharif et al. 2006; Vivoni et al. 2007).

Distributed hydrologic models are designed to continually ingest high-quality rainfall estimates and forecasts, allowing for real-time flood forecasting using information about future rainfall (Garrote and Bras 1995; Liu et al. 2005;

Vivoni et al. 2006; Collier 2007). Evidently, as in any other type of model, prior calibration plays a fundamental role in maintaining hydrologic uncertainties small during a flood forecasting exercise. Thus, the distributed nature of these types of hydrologic models permits exploring the spatial properties of the basin response relative to the spatiotemporal evolution of precipitation forcing. For example, the streamflow properties can be assessed as a function of watershed area to understand the scale-dependence of the flood forecast skill (e.g., Vivoni et al. 2007a,b). In addition, distributed modeling offers an opportunity to quantify the propagation of rainfall errors into the spatial hydrologic response and how these interact with basin properties. As a result of available spatial data on topography, soil and land cover properties, differential basin responses to meteorological forcing can be assessed over a range of conditions in a region (Germann et al. 2009; Mascaro et al. 2010b; Schröter et al. 2011).

Previous studies have explored the limits to flood predictability through the use of distributed hydrologic models. For example, Berenguer et al. (2005), Vivoni et al. (2006) and Sharif et al. (2006) used varying rainfall-runoff models to evaluate radar nowcasting techniques in different settings. The authors coincide in finding a decrease in the flood forecasting skill with rainfall forecast lead time, in accordance with theoretical models (Lin et al. 2005). On the other hand, while flood scaling theory is advanced in hydrology (e.g., Ogden and Dawdy 2003; Gupta 2004), only a few attempts have been made at analyzing the scale-dependence of flood forecasting skill by inspecting results at a range of internal watershed sites. For example, Benoit et al. (2000) quantified hydrologic errors of

radar nowcasts at 23 nested sites for a major flood event, while Vivoni et al. (2006) investigated the flood forecast skill from radar nowcasts at 15 internal sites during two separate flood events. Both studies coincide in observing a reduction in the total forecasting error with increasing basin area as a result of the integration of different hydrologic processes in the watershed. Despite these prior efforts, the spatial and temporal limits to flood predictability in mountain catchments experiencing summer convection are currently unknown.

This study seeks to quantify flood predictability using the TIN-based Real-time Integrated Basin Simulator (tRIBS, Ivanov et al., 2004a, Vivoni et al. 2007a) as a tool to generate flood predictions using radar nowcasting QPFs. With these coupled simulation tools, we quantify the relation of flood forecasting skill with lead time in a set of mountain basins that span several orders of magnitude in catchment scale. We pose the following question: Are floods at certain catchment scales more predictable due to the integration of physical processes and rainfall errors with contributing area? If so, then differences in runoff production resulting from varying hydrologic processes at different scales determine flood predictability in mountain catchments. We conduct our work in a set of headwater basins in the Colorado Front Range (CFR) due to its physiographic complexities and recurrent warm-season convective storms and their associated flood hazards. We analyze the skill of ensemble precipitation forecasts in light of observed rainfall fields derived from a calibrated radar product for two storm events. Subsequently, we investigate the distributed flood forecasting skill and its dependence with lead time and catchment scale for the ensemble rainfall fields. In

addition, we investigate how precipitation errors are transmitted to streamflow uncertainty at internal nodes as a flood wave progresses downstream. We find characteristic patterns in flood predictability governed by the varying watershed characteristics in the CFR through an analysis of the scale-dependence of flood forecast errors. Finally, we discuss the limits of flood forecasting with radar nowcasting in mountain environments.

METHODS

Study Region and Watershed Characteristics

The Colorado Front Range in the north-central Colorado, U.S.A, was selected for its availability of hydrometeorological information and historical potential for floods during the summer season (e.g., Petersen et al. 1999; Ashley and Ashley 2008). Regional data include high resolution (sub-hourly to hourly) information from stream gauges (11 in total), rain gauges and meteorological stations (7 in total) and NEXRAD weather radars (3 in total), as shown in Figure 4.1. Large summer convective storms from May to early September in the CFR originate from air mass interactions with the mountain environment. Moisture for summer convection can have its source in the subtropical Atlantic, subtropical Pacific or from precipitation recycling (e.g., Jarret and Costa 1988; Collins et al. 1991). Storm events with larger intensities and areal extents are more likely to occur at mid and low elevations in CFR (Jarret and Tomlinson 2000).

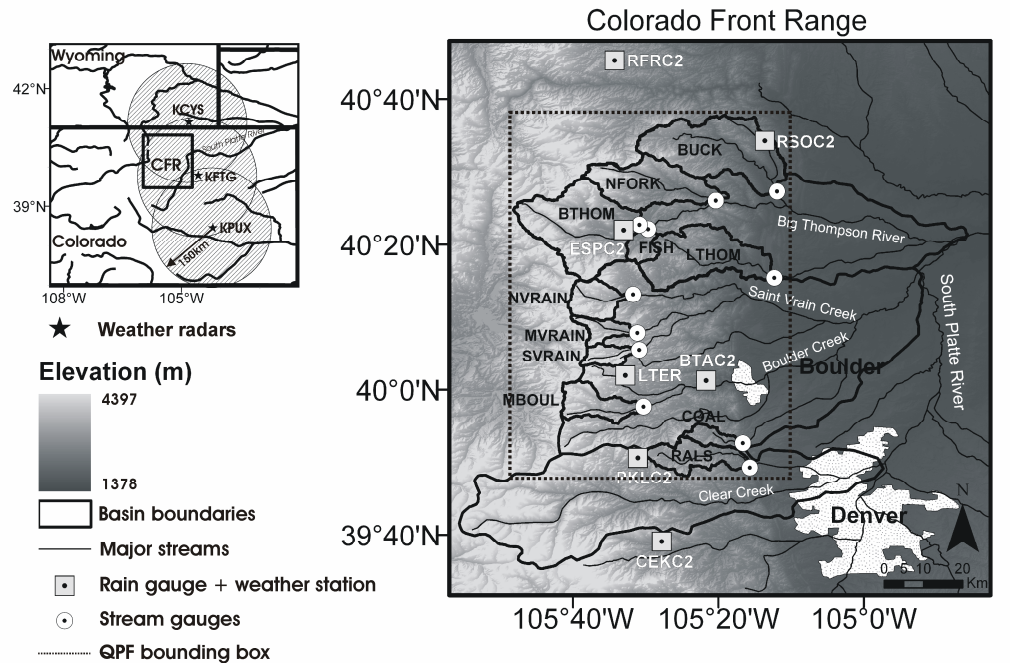

Figure 4.1. Colorado Front Range (CFR) location, elevation distribution and boundaries of eleven study watersheds: Buckhorn Creek (BUCK), North Fork Big Thompson River (NFORK), Big Thompson River (BTHOM), Fish Creek (FISH), Little Thompson River (LTHOM), North Saint Vrain Creek (NVRAIN), Middle Saint Vrain Creek (MVRAIN), South Saint Vrain Creek (SVRAIN), Middle Boulder Creek (MBOUL), Coal Creek (COAL) and Ralston Creek (RALS). 30-m Digital Elevation Model (DEM) was obtained from the National Elevation Dataset (Gesch et al. 2002). Seven hourly rain gauge and weather stations are shown: RFRC2, RSOC2, ESPC2, LTER, BTAC2, PKLC2 and CEKC2 with data from the AMERIFLUX and Mesowest networks (Steenburgh 2003). The associated geographic coverage of QPF products and the three weather radars (KCYS, KFTG, KPUX) and their 150 km coverage umbrellas are shown.

As a result, eleven headwater basins distributed on the east-facing slope of the CFR, northwest of the Denver urban corridor, were selected to quantify the flood forecasting skill obtained from radar nowcasting. Table 4.1 summarizes the major characteristics of the selected basins with drainage areas ranging between 37.2 and 359.5 km^2. The watersheds have considerable relief with mean elevations from 2287 to 3455 m.

Table 4.1. Topographic, soil and vegetation characteristics of the study watersheds.

Property	BUCK	NFORK	BTHOM	FISH	LTHOM	NVRAIN	MVRAIN	SVRAIN	MBOUL	COAL	RALS
Stream Gauge	BUCRMVCO	BTFDRCO	BTABESCO	FISHESCO	LTCANYCO	STALENCO	MIDSTECO	SSVWARCO	BOCMIDCO	COCREPCO	RALCRKCO
Total Area [km^2]	350.5	220.7	359.5	40.8	258.5	88.5	49.9	35.1	95.5	37.2	117.3
Length of main channel [km]	45.6	35.9	31.5	9.7	41	15.7	15.5	12.6	19.2	14.8	25.8
Slope of main channel [m/km]	26.2	48.4	67.2	70.5	27.8	59.7	53.9	42.3	48.4	49.0	32.1
Mean elevation [m]	2418	2774	3084	2858	2287	3302	3245	3455	3154	2509	2517
Minimum/maximum elevations [m]	1583/3268	1875/4120	2287/4343	2284/3473	1595/3460	2527/4344	2635/4225	2858/4087	2495/4075	1993/3183	1847/3204
Std. Elevation [m]	482	435.3	418	333	340	327	4029	344	337	187	387
Mean slope [%]	28.0	35.8	40.4	28.2	30.7	39.4	40.3	30.0	34.3	34.2	29.2
Std. Slope [%]	16.3	19.3	29.4	19.9	19.1	29.2	30.7	26.7	23.4	20.8	17.9
Major soil class 1 (% area)	Sandy loam (74.6)	Sandy loam (74.4)	Sandy loam (58.2)	Sandy loam (86.7)	Sandy loam (77.3)	Sandy loam (53.6)	Loam (38)	Sandy loam (44.1)	Sandy loam (45.2)	Sandy loam (39.9)	Loam (45.5)
Major soil class 2 (% area)	Loam (21.2)	Bedrock (16.1)	Bedrock (33.6)	Bedrock (6.9)	Loam (10.7)	Bedrock (30.4)	Sandy loam (36.7)	Loam (30.6)	Loam (41.9)	Loamy sand (34.2)	Sandy loam (34.4)
Major soil class 3 (% area)	Bedrock (3.1)	Loam (8.4)	Loam (4.8)	Loam (4.6)	Bedrock (8)	Loam (12.6)	Bedrock (25.3)	Bedrock (25.2)	Bedrock (12.4)	Bedrock (14.5)	Loamy sand (13.0)
Major vegetation class 1 (% area)	Forest (70.4)	Forest (77.7)	Forest (55.9)	Forest (76.2)	Grassland (50.1)	Forest (48.4)	Forest (40.8)	Forest (43.1)	Forest (51.8)	Forest (80.8)	Forest (77.8)
Major vegetation class 2 (% area)	Grassland (27)	Grassland (10.9)	Shrubland (19.7)	Shrubland (13.8)	Forest (48.9)	Grassland (26.1)	Grassland (27.3)	Grassland (22)	Shrubland (28.3)	Grassland (9.3)	Grassland (14.6)
Major vegetation class 3 (% area)	Agriculture (1.4)	Shrubland (10)	Grassland (17.1)	Grassland (5.1)	Shrubland (0.5)	Shrubland (14.0)	Shrubland (21.3)	Shrubland (19.4)	Grassland (9.7)	Shrubland (8.8)	Shrubland (7.1)
Time of concentration [h]	5.10	3.35	2.67	1.06	4.59	1.63	1.68	1.58	2.07	1.69	3.04

Given that some portions of their terrains are located at high altitude, six of the basins (NFORK, BTHOM, NVRAIN, MVRAIN, SVRAIN, MBOUL) have a direct influence of snowmelt processes in the summer season. The mean slopes vary between 28 and 40% with high standard deviations induced by the presence of vast areas of steep bedrock and the sudden changes in terrain features. Sharp slopes, narrow valleys and predominant dendritic patterns in the channel networks often lead to rapid runoff responses and short times of concentration (see Table 4.1). Figure 4.2 presents the spatial distribution of soils and vegetation types, elevation and stream channel networks in the watersheds. Overall, the watersheds are characterized by a heterogeneous mixture of soil and vegetation conditions. Dominant soils across the watersheds are sandy loam, loam and bedrock, while vegetation is characterized by the prevalence of upper montane, subalpine and alpine forest followed by lower montane grassland and shrubland.

Quantitative Precipitation Estimates and Event Characteristics

High resolution QPEs from volume scan reflectivity observations were obtained from the NEXRAD radars at Denver, CO (KFTG), Pueblo, CO (KPUX) and Cheyenne, WY (KCYS) over minimum and maximum volume scan altitudes of 3-km and 6-km, respectively. A power law of the form $Z = 700R^{1.3}$ was selected to convert reflectivity (Z) to 5-min, 1-km resolution rainfall rates (R) following an optimization procedure that minimizes errors with collocated pixels at seven rain gauges (Moreno et al. 2012b). Subsequently, the QPEs were time aggregated to 15-min, 1-km rainfall depths for the QPF bounding box region shown in Figure 4.1.

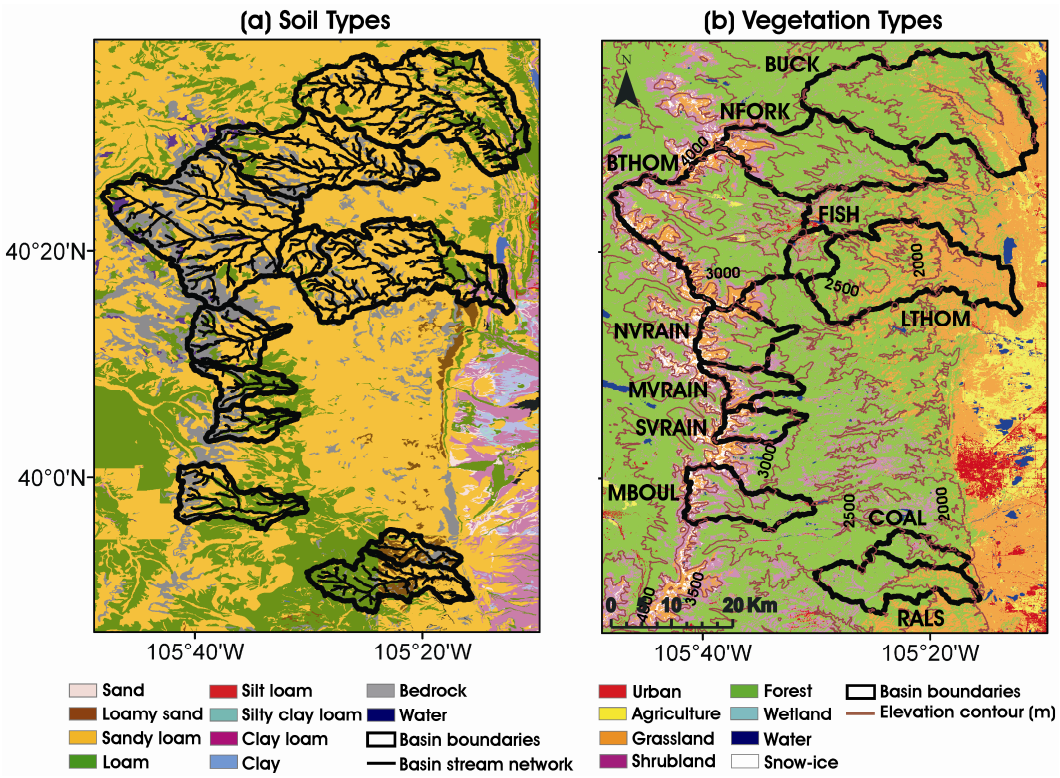

Figure 4.2. Spatial distributions of (a) soil types and (b) vegetation classes in the CFR. Elevation contours and basin stream networks for the selected watersheds are also shown. 30-m soil texture and vegetation type maps were obtained from the Soil Survey Geographic State Soil Geographic (Wang and Melesse 2006) and USGS National Landcover Dataset (Homer et al. 2004).

Two periods with warm-season precipitation in summers 2004 (17-22 August) and 2006 (6-14 July) were selected for conducting simulations using the radar nowcasting and distributed hydrologic modeling tools. These storm periods were chosen due to: (1) the simultaneous presence of observed streamflows across most of the watersheds, (2) the development and propagation of intense convective cells in different areas, (3) the presence of multiple rainfall events leading to superimposed basin responses, and (4) the relatively low contribution of the snowmelt to the streamflow response. The spatial distribution of cumulative rainfall depth for the two storm periods is shown in Figure 4.3.

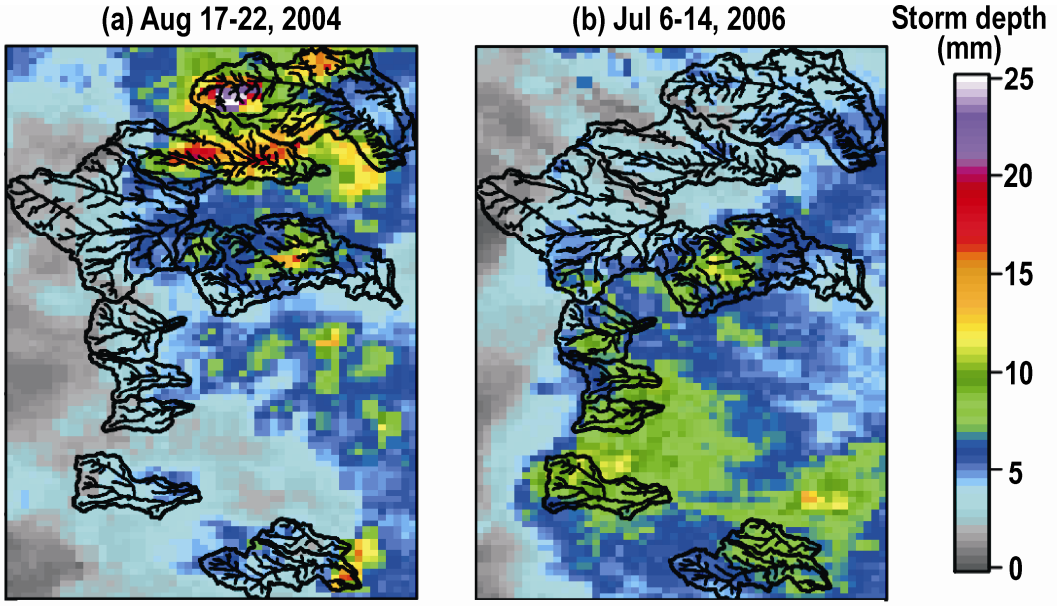

Figure 4.3. Spatial distribution of cumulative precipitation in (a) August 17-22, 2004 and (b) July 6-14, 2006, as measured by the Level II product at 5-min, 1-km resolution over the CFR.

The simulation windows were defined in a manner that the observed precipitation and hydrograph responses are fully captured across watersheds. The first period, henceforth called "Storm 2004", starts in Aug 17th, 2004, 09 LST and consists of several showers occurring during three consecutive days over different areas that triggered streamflow responses extending for nearly 125 hours in the largest watersheds. A series of thunderstorms moved from west to east and caused heavy precipitation during the afternoon hours (13 to 18 LST), while scattered convection was also observed in the lower zones of the northernmost basins independently of the main storm cores. Most of the heavy rainfall was concentrated in the northern basins (BUCK, NFORK, BTHOM, FISH, LTHOM), although observed hydrographs show responses in all catchments. The second storm period began on July 6th, 2006, 22 LST ("Storm 2006") and consisted of

three main cores of convection occurring during different days primarily in the afternoons and some rain extending into the evening hours. A prevalent storm motion direction was observed from the south. These storm sequences generated flood responses in most of the study basins extending up to 160 hours in some cases and were more evident in NVRAIN, MVRAIN, SVRAIN, MBOUL, COAL and RALS located in the southern region.

Quantitative Precipitation Forecasts and Radar Nowcasting Mode

The NCAR Thunderstorm Identification, Tracking, Analysis, and Nowcasting (TITAN; Dixon and Wiener 1993) algorithm was used to generate short-term radar nowcasting QPFs over the CFR. The algorithm allows for real-time automated identification, tracking, and short-term forecasting of thunderstorms based on volume-scan weather radar data. An optimization scheme was employed to match observed storms at one time instance with those at a following time, with geometric operations to deal with mergers and splits. The short-term forecasts of both position and size are based on a weighted linear fit to the storm track history data. This methodology provides the framework necessary to identify storms within three-dimensional radar data and to track them as physical entities (Dixon and Wiener 1993; Joe et al. 2004). Due to the number of parameters used in TITAN for controlling forecast properties, we generated a set of nowcasting ensembles consisting of 27 members per forecast lead time. Ensemble QPFs were produced at a fine resolution (1-km, 15-min) for lead times between 15 and 180 minutes (15, 30, 45, 60, 90, 120, 15 and 180 min). We varied the following TITAN model parameters within feasible ranges to generate each

ensemble for each lead time: (1) minimum storm size (10, 20, 30 km^2), (2) tracking forecast weight rates (0.1, 0.25, 0.5), and (3) reflectivity dual thresholds (5, 25, 45 dB).

The extended-lead forecast mode proposed by Vivoni et al. (2006) was used to generate QPFs using available radar observations. In this mode, we eliminate the assumption of no future rainfall by providing nowcasting fields at a single rainfall lead time (T_L) over a flood forecasting window defined between the start of observed precipitation, t_i, and $t_i + T_F$, the flood forecast end time. As shown in Figure 4.4, the forecasting time (T_F) is discretized into $T_F/\Delta t$ time steps, where Δt represents the time step at which forecasts are issued. As an example, Figure 4.4 shows $T_F = 2T_L$ for clarity. Normally, many T_L intervals are contained within T_F. Thus, a forecast starting at the time t_i for a lead time (T_L) uses the $T_L/\Delta t$ most recent historical data (QPEs) to extrapolate the precipitation field continuously for Δt steps until reaching T_F (Δt is 15-min here). Rainfall forecasts (QPFs) of the same lead time (T_L) are assembled in a continuous manner separated by Δt intervals. This ensures that each available QPE is extrapolated into a QPF with the same skill specified by an identical lead time (Vivoni et al. 2006). By increasing T_L, the time displacement between the QPEs and resulting QPFs is enlarged. Precipitation forecasts that change with lead time are expected to influence flood forecast skill at basin outlets and at internal watershed sites.

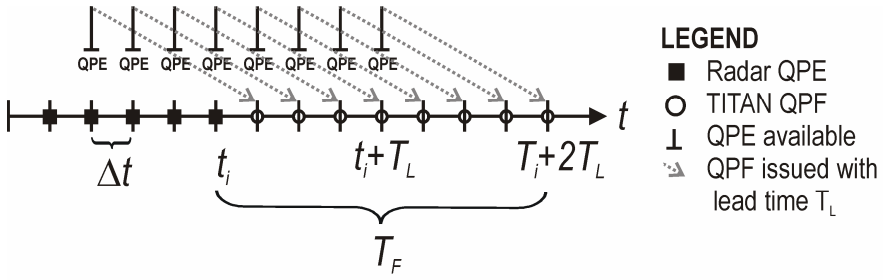

Figure 4.4. Schematic of radar nowcasting using the extended-lead forecast mode. Gridded QPFs are continuously available at each time step Δt over the forecast period T_F. In this example, nowcasts are issued with a lead time $T_L = 4\Delta t$ by using the $T_F/\Delta t$ most recent QPEs. Dashed arrows have horizontal length T_L.

Distributed Hydrologic Modeling and Numerical Experiments

Model overview

We apply the tRIBS model to investigate the impacts of radar nowcasting on the flood forecasting skill in the study watersheds in the Colorado Front Range. The distributed model was developed for flood forecasting using precipitation inputs at fine spatiotemporal resolutions and has been tested in different mountainous regions (e.g., Vivoni et al. 2007b, 2009; Nikolopoulus et al. 2011, Moreno et al. 2012a). tRIBS uses Voronoi polygons, derived from a Triangulated Irregular Network (TIN), to represent basin characteristics with a reduced number of nodes relative to the original data (Vivoni et al. 2004). Surface-subsurface moisture dynamics at each computational node are resolved by tracking infiltration fronts, water table fluctuations and lateral redistribution in the hillslope and channel system. Surface runoff during storm events is produced by infiltration-excess, saturation-excess, perched return flow and groundwater exfiltration mechanisms, while flood routing is performed through hydrologic

overland flow and hydraulic channel routing (e.g., Ivanov et al. 2004a). The kinematic wave approach is used to model water transport and dispersion in natural channels whose geometry is defined through geomorphic relationships. Water losses to the atmosphere occur through soil evaporation, plant transpiration and evaporation of intercepted water.

As a physically-based model, tRIBS is able to ingest spatially-varying terrain, soil and vegetation properties, as well as spatiotemporal meteorological forcing, to reproduce hydrologic process evolution at scales ranging from hillslopes to large river basins. tRIBS can utilize QPFs from radar nowcasting to generate streamflow forecasts at the basin outlet and at interior or nested sites. As a result, improvements in flood forecast skill should be expected as the rainfall nowcast lead time is added to the watershed response time, a convenient advantage for purposes of early flood warnings. Further gains in computational efficiency of ensemble simulations can be achieved through the use of parallel computations that assign interior sub-basins to different computer processors in a high performance computing cluster (Vivoni et al. 2011).

Model parameters and initialization

The distributed model requires parameters describing the surface, subsurface, vegetation and channel characteristics that control the hydrologic response to storm and interstorm periods. Soil parameters describe hydraulic and thermal properties at the soil surface and their variation with depth. Primary soil parameters are the saturated hydraulic conductivity (K_s) and its decay exponent with depth (f), the ratio of horizontal to vertical conductivities (A), soil moisture at

saturation (θ_s), residual soil moisture content (θ_r), pore-size distribution index (λ_0), air entry bubbling pressure (Ψ_b), thermal conductivity (K_T), volumetric heat capacity (C_s) and the depth to bedrock (B). In addition, vegetation parameters control interception and evapotranspiration processes for different land cover types. Characteristic vegetation parameters are free throughfall coefficient (p), canopy field capacity (S), drainage rate coefficient (K), drainage exponent (g), and average stomatal resistance (r_s), surface albedo (a), optical transmission coefficient (K_t), and vegetation height (H_v) and fraction (v). Model parameterization also includes specifying hillslope and channel properties controlling routing: Manning roughness coefficient (n_e), hillslope velocity coefficient (C_v) and exponent (r), and channel width-area coefficient (α_B) and exponent (β_B).

In addition, the model requires specification of spatially-distributed initial conditions that characterize the soil moisture state. These are particularly critical for flood forecasting as the effect of initialization is not dissipated in short simulation periods. An assumption of hydrostatic equilibrium allows inferring soil moisture profiles from the depth to the groundwater table (Ivanov et al. 2004a,b). This can be derived using a number of approaches. In this study, a long-term drainage experiment was conducted in each watershed following the procedure outlined by Vivoni et al. (2007a). Drainage experiments start with fully-saturated basins that are allowed to drain for a long period (10-years) without weather or rainfall forcing, leading to hydrographs that are uniquely controlled by soil, channel network and geomorphic characteristics of individual watersheds. As a

result, the simulated instantaneous outlet discharges (Q_b) are related to model-based estimates of the spatial mean depth to groundwater (N_{wt}) through rating curves relating those variables (e.g., Vivoni et al. 2008; Moreno et al. 2012a). The availability of multiple groundwater depth maps associated with specific outlet discharges allowed selecting a set of feasible scenarios (10 per basin from wet to dry conditions) for N_{wt} corresponding to percentiles of the exceedence probability of the observed discharge at each basin stream gauge for summers 2003-2006. The use of exceedence probability of the observed discharges offers a set of realistic streamflow values that are uniquely related to spatially distributed groundwater depths.

Model calibration and testing strategy

Hydrologic processes occurring in mountain catchments merit a careful analysis of model parameters and initial conditions at the storm event scale. The approach in this study first evaluated the relative importance of individual model parameters and initial condition during One-at-A-Time (OAT) analysis in several watersheds (Moreno et al. 2012a). Results indicated that outlet streamflow responses were principally controlled by a limited set of parameters including the initial conditions (Table 4.2). We found the initial depth to groundwater ($\mu(N_{wt})$) played an important role due to the relatively shallow aquifer (Birkeland et al. 2003) and the presence of snow processes in several basins.

Table 4.2. Calibrated parameters and initial conditions in each study watershed during the storm events in August 17-22, 2004. Calibration scores (RMSE and NS) are also shown.

Basin	Soil type	K_s [mm/h]	θ_s [-]	λ_0 [-]	ψ_b [mm]	f [mm^{-1}]	A[-]	r[-]	B [m]	$\mu(N_{wt})$ [m]	RMSE	N-S
BUCK	Sandy loam	7.96	0.32	0.81	-244.22	0.03336	223.00	0.45	1.26	1.17	0.46	0.61
	Loam	30.29	0.37	1.46	-704.46	0.02529	25.00					
NFORK	Sandy loam	35.83	0.36	1.38	-27.03	0.01309	274.70	0.42	1.42	0.39	1.44	-0.81
	Bedrock	1.28	0.07	0.25	-580.70	0.04833	1.55					
BTHOM	Sandy loam	30.69	0.58	1.18	-187.17	0.00542	234.63	0.36	0.96	0.59	1.44	-2.42
	Bedrock	3.18	0.02	0.19	-209.35	0.00678	1.00					
FISH	Sandy loam	0.41	0.6	1.59	-92.01	0.00927	649.07	0.43	1.02	1.092	0.09	0.29
	Bedrock	3.32	0.05	0.11	-489.46	0.00659	1.55					
LTHOM	Sandy loam	4.78	0.57	1.42	-172.46	0.04226	683.01	0.43	1.92	0.39	0.19	0.83
	Loam	7.16	0.37	0.29	-838.89	0.00105	110.38					
NVRAIN	Sandy loam	11.15	0.42	0.53	-29.68	0.00878	887.97	0.45	2.90	0.18	0.12	0.75
	Bedrock	0.69	0.02	0.29	-70.87	0.01066	1.87					
MVRAIN	Loam	13.09	0.58	1.01	-179.58	0.00699	752.14	0.45	0.92	0.26	0.24	-0.26
	Sandy loam	31.58	0.54	0.81	-342.81	0.01653	275.27					
SVRAIN	Sandy loam	10.55	0.34	1.62	-343.20	0.00170	743.76	0.45	0.67	0.49	0.15	0.63
	Loam	20.25	0.37	0.10	-444.64	0.01033	122.64					
MBOUL	Sandy loam	35.51	0.42	1.20	-75.36	0.04068	394.13	0.37	1.79	0.35	0.22	0.38
	Loam	6.49	0.34	1.19	-20.81	0.00543	647.22					
COAL	Sandy loam	22.28	0.38	1.66	-21.19	0.02350	691.23	0.37	0.26	0.39	0.37	0.01
	Loamy sand	84.30	0.36	0.61	-160.97	0.01318	791.19					
RALS	Loam	24.22	0.39	0.82	-680.26	0.00320	80.94	0.43	2.31	0.84	0.23	0.33
	Sandy loam	24.42	0.57	1.73	-387.27	0.02379	191.62					

Parameters, other than those listed in Table 4.2, were assigned to reference values from the literature (e.g., Chow 1959; Bear 1972; Rutter et al. 1977; Rawls et al. 1982; Shuttleworth 1988; Birkeland et al. 2003; Ivanov et al. 2004b; Mitchell et al. 2004; Todd and Mays 2005). The Shuffle Complex Evolution (SCE) algorithm (Duan et al. 1993) was then used to automatically find values for selected parameters and initial conditions within feasible ranges of variation reported in prior studies. Storm 2004 was selected to perform the calibration through objective functions that minimized the Root Mean Squared Error (RMSE) between the observed and simulated streamflow at each basin outlet over the defined period. Through the selection of Storm 2004 as a calibration event, the distributed model parameters are tailored for flood forecasting purposes under summer convective storms. Table 4.2 summarizes the values for the calibrated parameters at each basin during Storm 2004, along with the RMSE and Nash-Sutcliffe (NS) efficiency scores, relative to the observed streamflow. Calibrated parameter values differ among watersheds due to their unique terrain, soil and vegetation characteristics, and initial conditions and fall within realistic ranges. Unavoidably, parameters provide degrees of freedom to compensate for model uncertainties in a manner that differs from basin to basin. In addition to comparisons with streamflow data, flood forecasting skill was assessed with respect to the simulated hydrographs resulting from QPE forcings that contain no rainfall forecast errors.

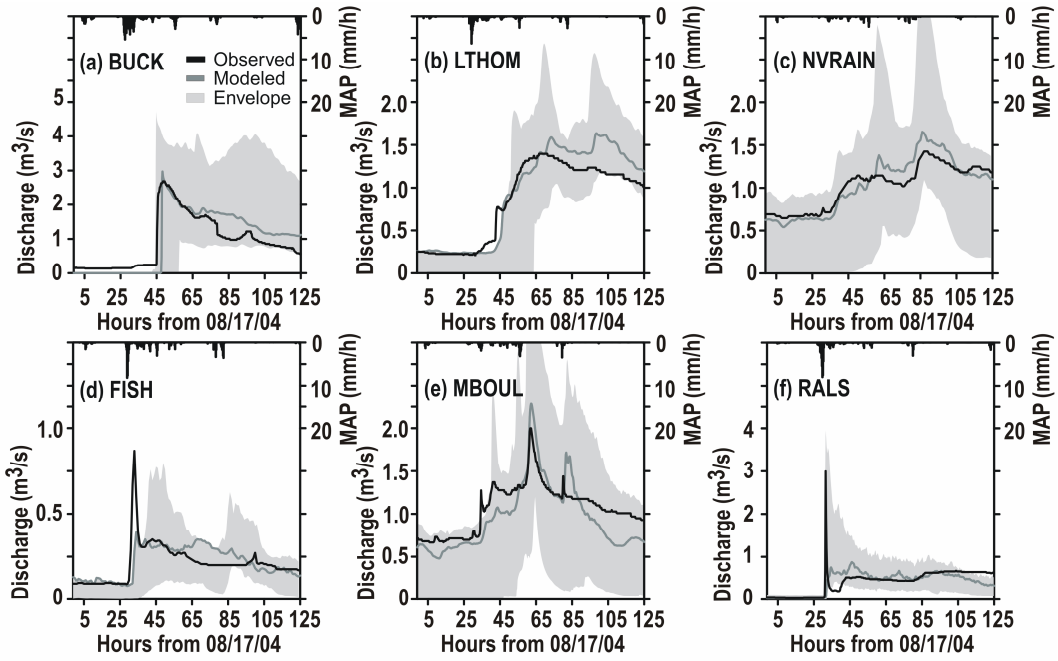

Figure 4.5. Observed (black lines) and simulated hydrographs (dark gray lines) resulting from the model calibration at six selected basins at 15-min intervals. Mean Areal Precipitation (MAP) in each basin is derived from the 15-min, 1-km Level II product. Uncertainty in parameter values and initial conditions is represented by the light gray envelopes.

Figure 4.5 presents the observed hydrographs and simulations derived from the calibration exercise at BUCK, LTHOM, NVRAIN, FISH, MBOUL and RALS as representative watersheds for both large (BUCK, LTHOM), medium (RALS) and small (FISH) basins and some with the influence of snow processes (NVRAIN, MBOUL). Similar results were obtained for the remainder of the basins. The top 10% of the parameters sets obtained through the SCE procedure for each basin are represented by the gray envelopes in the plots. Note that the model is able to reproduce the distinct hydrologic patterns resulting from the combination of rainfall forcing, watershed properties and initial conditions in each individual catchment. For example, compare the longer response times and

extended recessions at large basins (e.g. BUCK and LTHOM), with the faster time to peak discharge in small catchments (e.g. FISH and RALS). Furthermore, note the important role of wet initial conditions that amplify the total discharge and delay recession times in watersheds with a summer snowmelt signal (e.g. NVRAIN and MBOUL). Model calibration provides confidence to test the science hypothesis relative to QPE forcing. These results indicate that the distributed model is able to capture the different responses fairly well with RMSE ranging from 0.09 to 1.44 m^3/s, depending on the particular properties of individual watersheds. The largest streamflow errors are found in BTHOM and NFORK where the model is unable to replicate the high base flows from summer snowmelt processes not represented in this application (but, see Rinehart et al. 2008). The remaining discrepancies can be explained by model structural uncertainties, precipitation forcing and streamflow measurement errors. Flood forecasts for Storm 2006 constitute an independent verification exercise that tests the robustness of the calibrated parameters across the watersheds. During these experiments, no parameters will be calibrated and only the initial condition will be adjusted for the different year.

Nowcasting experiments

Rainfall and flood forecasts generated by the TITAN and tRIBS models in the extended-lead forecasting mode accounted for 216 model runs (8 lead times and 27 ensemble members) per storm period in each basin, for a total of 4752 forecasts. The duration of each forecasting period (T_F) was 125 and 170 hours, while the start (t_i) and end (t_i+T_F) times were August 17th 09 LST to August 22nd

14 LST, 2004 and July 6th 22 LST to July 14th 00 LST, 2006, respectively. A hydrologic restart mode, at hours 75 and 30 for Storms 2004 and 2006, was used in a manner that initial conditions and QPE forcings were preserved during the ensemble forecasting periods. In addition, efficient fully-distributed hydrologic modeling was achieved through the use of a high performance computing facility at Arizona State University. The parallel capabilities of tRIBS were used to assign a relative low number of processors to each basin (8 in total). For the largest watershed in this study, tRIBS issued flood forecasts at a rate of 2.5 forecasting hours per minute of computational processing. However, on average, the model issued flood forecasts for the next 24 hours in one minute of computational time. Thus, the parallel performance suggests that the model can be used in operational forecasting environments.

RESULTS AND DISCUSSION

Regional Evaluation of Quantitative Precipitation Forecasts

The spatiotemporal properties of nowcasting QPFs over the CFR are assessed using two types of grid-to-grid verification methods. These consider ensemble members for each lead time in categorical and quantitative analyses that help elucidate the regional properties of the QPFs with respect to radar QPEs. The first approach introduces a probabilistic analysis in terms of the Probability of Detection (POD), False Alarm Rate (FAR) and Critical Success Index (CSI) from contingency tables for distinct forecast thresholds (Ganguly and Bras 2003; Wilks 2006; Gochis et al. 2009).

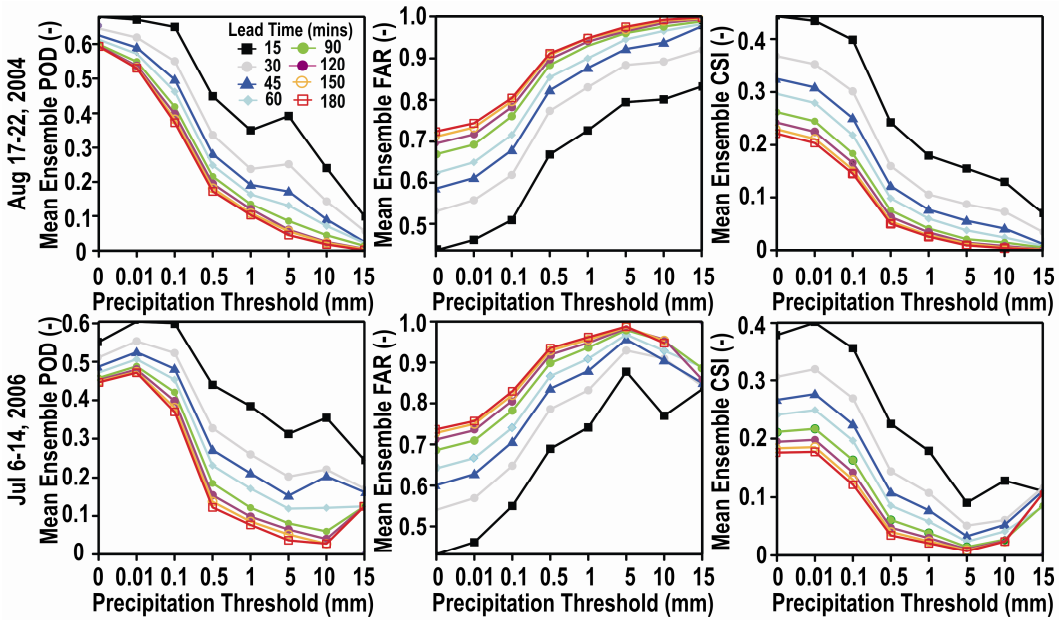

Figure 4.6. Radar nowcasting QPF skill as derived from contingency tables for storm periods in 2004 (top row) and 2006 (bottom row) over the CFR relative to the radar QPEs. Different precipitation threshold values (horizontal axis) were tested for various lead times (colored lines). Categorical verification metrics include the mean ensemble Probability of Detection (POD, left panels), False Alarm Ratio (FAR, middle panels) and Critical Success Index (CSI, right panels).

Figure 4.6 illustrates the different evaluation metrics for the storm periods in 2004 and 2006. A threshold of zero rainfall indicates the success or failure of the forecast given that rainfall is observed, independent of its magnitude. For subsequent thresholds, successes are only achieved if forecasted precipitation is greater or equal than the specified value. Both storm periods exhibit similar results with lower forecast skill (low POD, high FAR, low CSI) as lead time increases at all threshold values. Nowcasting skill deteriorates at a faster rate for short lead times (e.g., between 15 and 45-min) as compared to the performance change for longer T_L (e.g., from 120 to 180-min). The POD of rainfall occurrence (when the threshold equals zero) is 0.6 in 2004 and 0.5 in 2006, on average for all

lead times. However, a decrease in the forecast skill scores occurs for larger events. The magnitude of this decrease depends on lead time, but 5 mm appears to be the value after which no further decreases in skill are observed. The underlying cause for the rainfall forecast skill decreases with threshold value is the difficulty to accurately estimate high magnitude precipitation events that have less frequent occurrences in the region. The second approach is tailored to quantify the reduction in rainfall forecasting skill with lead time using the Root Mean Square Error (P_R), Correlation Coefficient (*CC*) and Mean Ensemble Difference (*DIFF*) between the QPF members and corresponding QPEs, defined as:

$$DIFF = \frac{1}{n}\sum_{i=1}^{n}\left(\overline{QPF}_{t,i} - \overline{QPE}_{t}\right) \quad \forall_i = \{1, 2, 3, \ldots, 27\}\ , \tag{4.1}$$

where overbars represent spatial means, *t* is the forecast time, *i* is the ensemble member and *n* is the total number of members. *DIFF* can be interpreted as the average difference representing under- or overestimation of precipitation over the region. Figure 4.7 presents these metrics as a function of lead time for the two storm periods in the form of boxplots that capture the ensemble distributions. A similar pattern in the variation of each metric with lead time is observed in the two storm periods, though differing magnitudes are present. With higher lead time, an asymptotic increase in forecast P_R and an asymptotic reduction in *CC* are found. In general, the spread among ensemble members is larger for smaller lead times for the P_R and *CC* metrics. This is not the case for *DIFF* where under- or overestimations can average out to small standard deviations at small lead times.

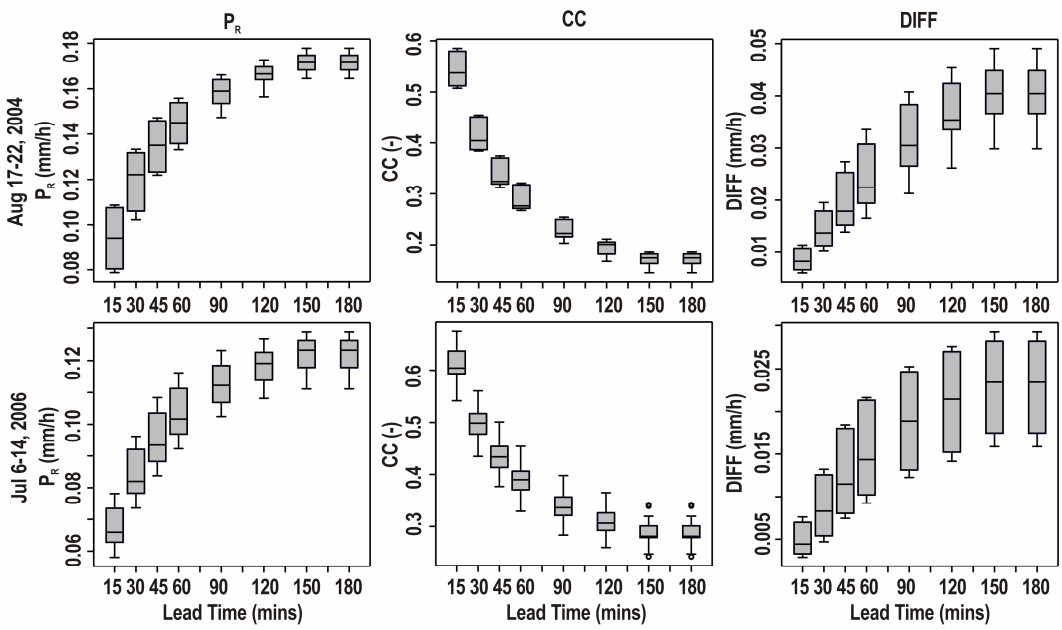

Figure 4.7. Boxplot diagrams of ensemble precipitation forecast skill as a function of lead time for the Storms 2004 and 2006 over the CFR. Metrics include the space-time averaged Root Mean Square Error (P_R), Correlation Coefficient (CC) and Mean Ensemble Difference (DIFF).

The most noticeable decrease in forecast skill occurs beyond the 30-min lead time, the limit at which forecasts become less useful. On the other hand, the limit at which predictions no longer worsen appears to be 150-min.The positive values of *DIFF* and their increase with lead time indicates that radar nowcasts tend to overestimate precipitation, thus increasing the number of false alarms, especially for large lead times. Precipitation forecasting uncertainties are expected to propagate into the hydrologic predictive skill, as explored in the following sections.

Lead Time Dependence of Flood Forecasting Skill

The rainfall error structures with nowcast lead time are expected to be reflected in the flood forecasting skill across individual watersheds. Watershed

characteristics, specified through the model domain, parameters and initial conditions, however, are anticipated to play a role in the hydrologic response so that rainfall errors are not transmitted identically to the streamflow forecasts across the different basins. Figure 4.8 presents the flood forecasting skill at four selected watershed and storm pairs through the Root Mean Square Error (Q_R), Nash-Sutcliffe coefficient (*NS*) and Mean Ensemble Difference ($DIFF_Q$), evaluated at basin outlets. $DIFF_Q$ is defined as:

$$DIFF_Q = \frac{1}{n}\sum_{t=1}^{n}\left(QSF_{t,i} - QSE_t\right) \quad \forall_i = \{1, 2, 3, \ldots, 27\}\ , \tag{4.2}$$

where *QSF* and *QSE* are the instantaneous forecasted and estimated outlet streamflows at the time step *t* for the i^{th} ensemble member; *n* is the total number of forecasted time steps. These watershed and storm pairs exhibit representative behaviors for other basins, whose patterns in Q_R, *NS* and $DIFF_Q$ will be discussed next. As a general rule, the flood forecasting skill decreases with lead time across the metrics, although an asymptotic behavior is not necessarily observed for all watersheds. This results from the variability in streamflow response for QPFs with different errors due to the basin effects on flood timing and magnitude. Q_R and *NS* illustrate similar patterns for the same watershed and storm, but a slightly different behavior is presented by $DIFF_Q$ with larger ensemble spreads at small lead times. Consistent with prior analyses, $DIFF_Q$ has positive values in all cases as a result of regional rainfall overestimation.

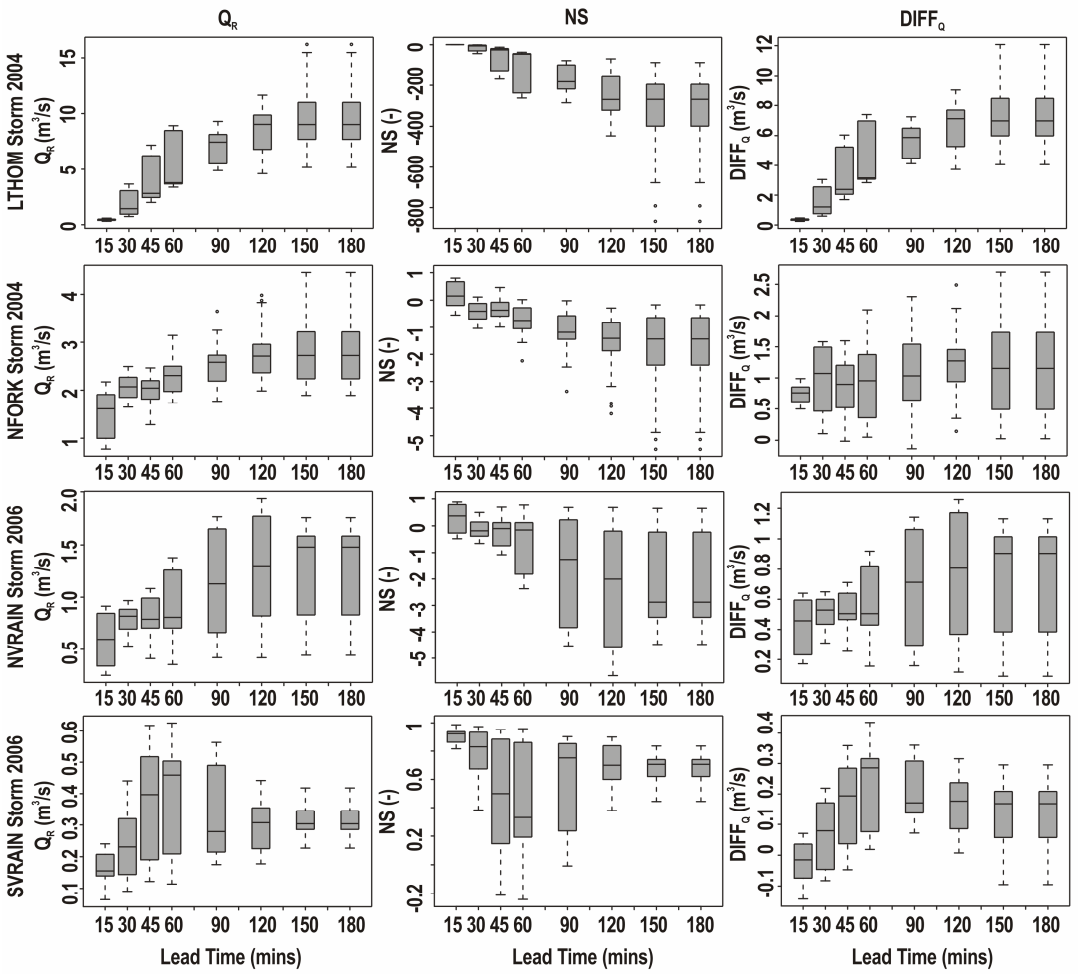

Figure 4.8. Boxplot diagrams of ensemble flood forecast skill as a function of lead time for four selected watersheds (LTHOM, NFORK, NVRAIN, SVRAIN) during the Storms 2004 and 2006. Metrics include the space-time averaged Root Mean Square Error (Q_R), Correlation Coefficient (CC) and Mean Ensemble Difference ($DIFF_Q$).

Both Q_R and *NS* indicate that flood forecasting skill is no better than the mean value as a forecast (*NS* < 0) for lead times greater than 30-min. This is consistent with the QPF skill dependence on lead time, indicating the critical role of nowcasting errors on flood forecast skill. Two exceptions are SVRAIN and MBOUL in Storm 2006 that present *NS* below zero after the 60-min lead time as a result of the snowmelt influence on streamflow. Three different patterns are

observed for the variation of streamflow Q_R, NS and $DIFF_Q$ with lead time. (1) The ensemble mean grows asymptotically and interquartile range increases with lead time as observed for LTHOM and NFORK in Storm 2004 and is replicated in 12 of the 22 studied cases. This behavior occurs when rainfall predictability exerts a clear influence on flood forecasting skill, thus preserving similar functional relations with lead time. Increases in ensemble dispersion are due to variations in streamflow responses induced when precipitation events exceed hydrologic thresholds, such as infiltration capacity. (2) In five of the studied cases, a similar overall pattern is observed as in (1), but after a particular lead time (e.g. 120-min for NVRAIN in Storm 2006), the interquartile range decreases slightly, possibly due to a reduction in rainfall ensemble spread at individual watersheds. (3) In the remaining cases, a similar pattern to (2) is observed, except that both the ensemble mean and interquartile ranges decrease after a certain lead time (e.g. 60-min in SVRAIN in Storm 2006). This case occurs for small catchments under low rainfall amounts or snowmelt-dominated basins where increases in lead time do not necessarily translate into streamflow error. In summary, QPF errors play a significant role on the functional relations between flood forecasting skill and lead time that translate into their limited utility beyond 30-min, except in basins where snowmelt is a major driver. However, watershed initial conditions and properties induce different ensemble responses that shape the functional relations for long lead times, no longer preserving the asymptotic behavior observed in rainfall only. In the next section, the flood forecast skill is assessed as a function of catchment area to identify potential spatial limits to predictability.

Scale Dependence of Flood Forecasting Skill

The impacts of warm-season rainfall variability in the CFR region are explored through distributed measures of runoff and internal channel discharges to elucidate the potential relation between flood predictability and basin scale. Figure 4.9 shows examples of the spatial distribution of total precipitation and runoff from the QPE forcing along with the mean ensemble differences from the QPF forcing at two lead times (60 and 180-min) for Storm 2004 in LTHOM. Note the location of storm cores in the north-central part of the basin might favor increased runoff, but the maximum runoff amounts do not necessarily overlap. This indicates that basin properties (e.g., terrain slope, soil hydraulic conductivity, initial soil wetness) play a critical role in the basin susceptibility to flooding. The mean ensemble differences in rainfall and runoff are primarily positive in the basin, indicating a general overestimation of precipitation and runoff amounts by the QPFs and the flood forecasts derived from these. As expected, larger positive differences in rainfall and runoff occur for larger lead times (180-min versus 60-min). More interestingly, the changes in the spatial distribution of forecasted precipitation (Figs. 4.9 c and e) with lead time are more dramatic than in runoff (Figs. 4.9 d and f), as watershed characteristics tend to dampen the rainfall forecast errors. Thus, while the spatial distribution and magnitude of QPFs show changes with lead time, the expected differences in basin response are mostly reflected in runoff magnitudes, while the spatial patterns remain constant in response to static basin properties.

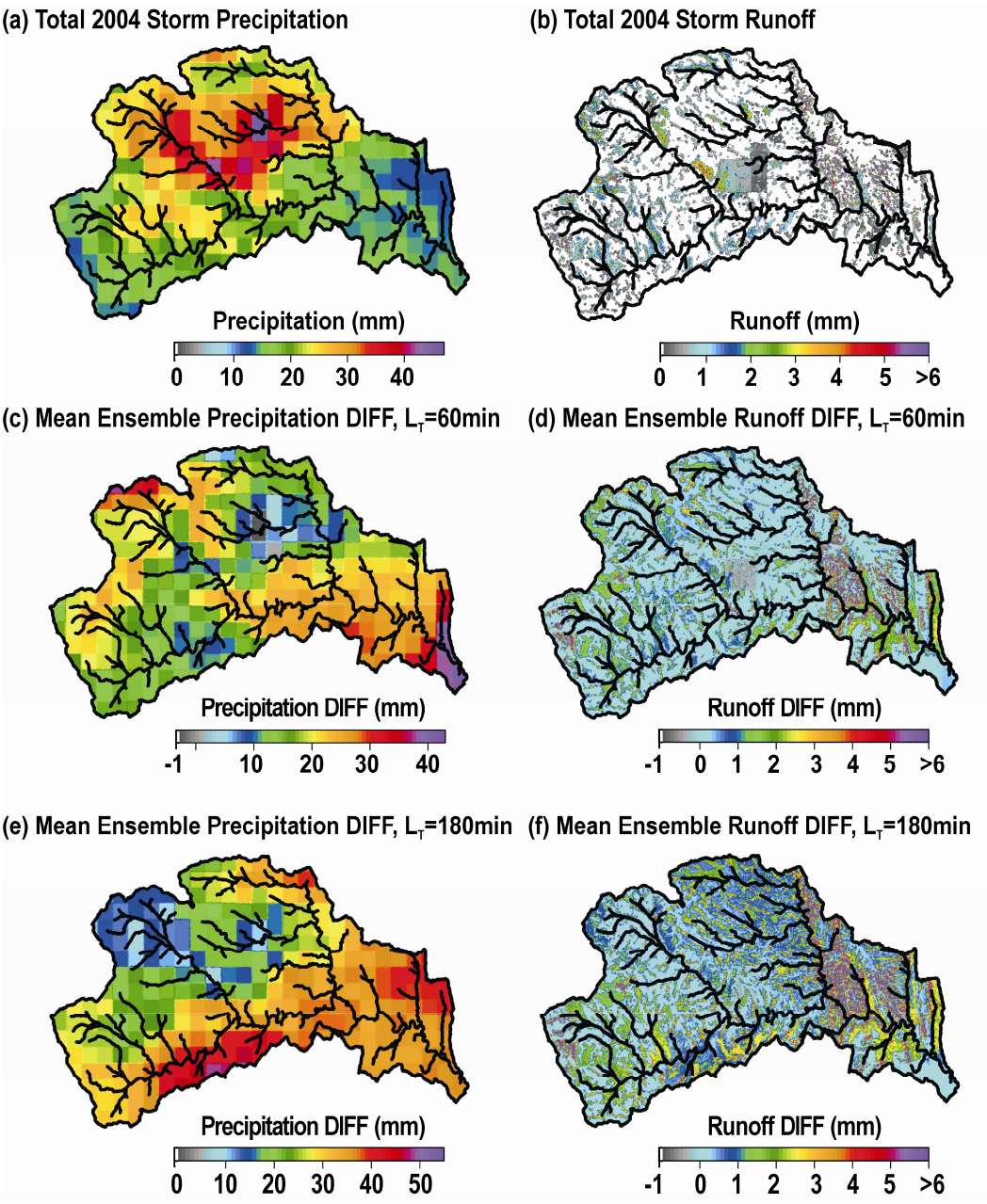

Figure 4.9. Spatial distribution of total (a) rainfall and (b) runoff at LTHOM during Storm 2004, using QPE forcing; mean ensemble difference of precipitation for (c) 60-min and (e) 180-min lead times; and mean ensemble differences of runoff for (d) 60-min and (f) 180-min lead times.

These results suggest that rainfall forecast errors are not the only driver of flood forecast skill across mountain watersheds for the same lead time. To investigate this issue further, we selected channel locations corresponding to different contributing areas within and downstream of the major storm cores in 2004 and 2006. Two basin groups were created corresponding to the major storm locations for each period: 2004 (BUCK, NFORK, BTHOM, FISH, LTHOM) and 2006 (NVRAIN, MVRAIN, SVRAIN, MBOUL, RALS, COAL). Figure 4.10 presents the spatial scale-dependence of RMSE in forecasted precipitation (P_R) and runoff (Q_R) relative to the QPE and its derived flood forecast. The symbols represent the ensemble mean, while the vertical bars depict the ensemble standard deviation. Three different basins (NFORK, LTHOM, SRVAIN) and two lead times (60 and 180-min) were selected as representative examples.

Results reveal that, although P_R and Q_R increase with lead time in most basins, a clear pattern is not present between P_R and catchment area (A_c) that can explain the growing dependence of the ensemble mean Q_R and its standard deviation (or ensemble spread) with A_c. Furthermore, no compensating or amplifying behaviors in the ensemble mean or spread are observed for P_R with basin area that supports the scale-dependence of Q_R. The growing trends in Q_R with A_c are instead due to the dependence of the streamflow forecast errors on flood magnitudes, which naturally increase with basin area, as noted by Moreno et al. (2012b).

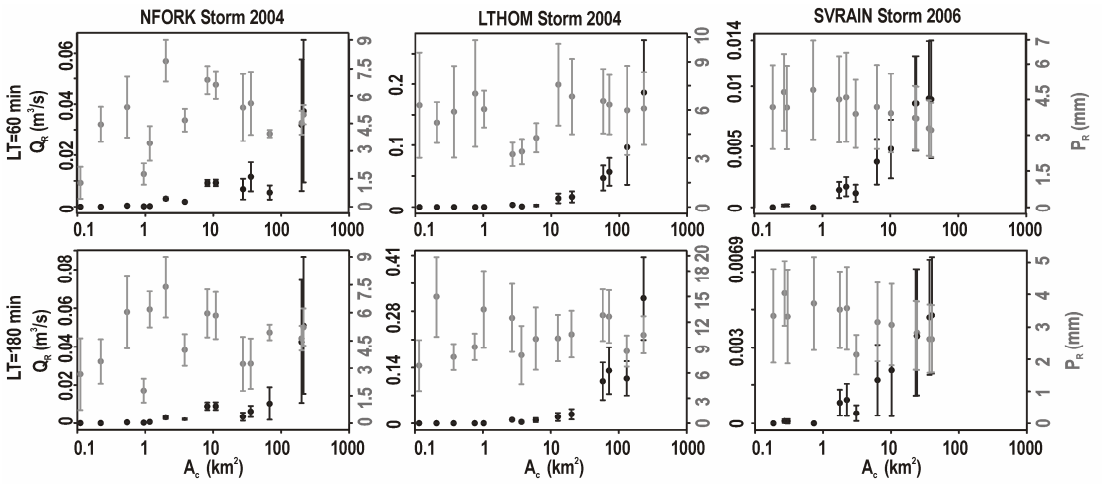

Figure 4.10. Rainfall and streamflow error propagation with basin area for three basins and two lead times (60 and 180-min) during Storms 2004 and 2006. Symbols represent the ensemble mean, while the vertical bars are the ensemble standard deviation.

This evidence points to the need to integrate the spatial characteristics of rainfall forecasts and the corresponding patterns in runoff production, that are linked to watershed properties, to obtain a full picture of the flood predictability in space.

Scale Dependence on Ensemble Properties of Streamflow Errors

Spatial differences in streamflow errors due to variations in rainfall and basin properties can be assessed through the Specific Error (*SE*), defined as (Moreno et al. 2012b):

$$SE = \frac{Q_R}{A_c MAP} \ , \tag{4.3}$$

where Q_R is the Root Mean Square Error in forecasted streamflow relative to QPE-forced simulation at internal channel sites characterized by an upstream area (A_c) and mean areal precipitation (*MAP*).

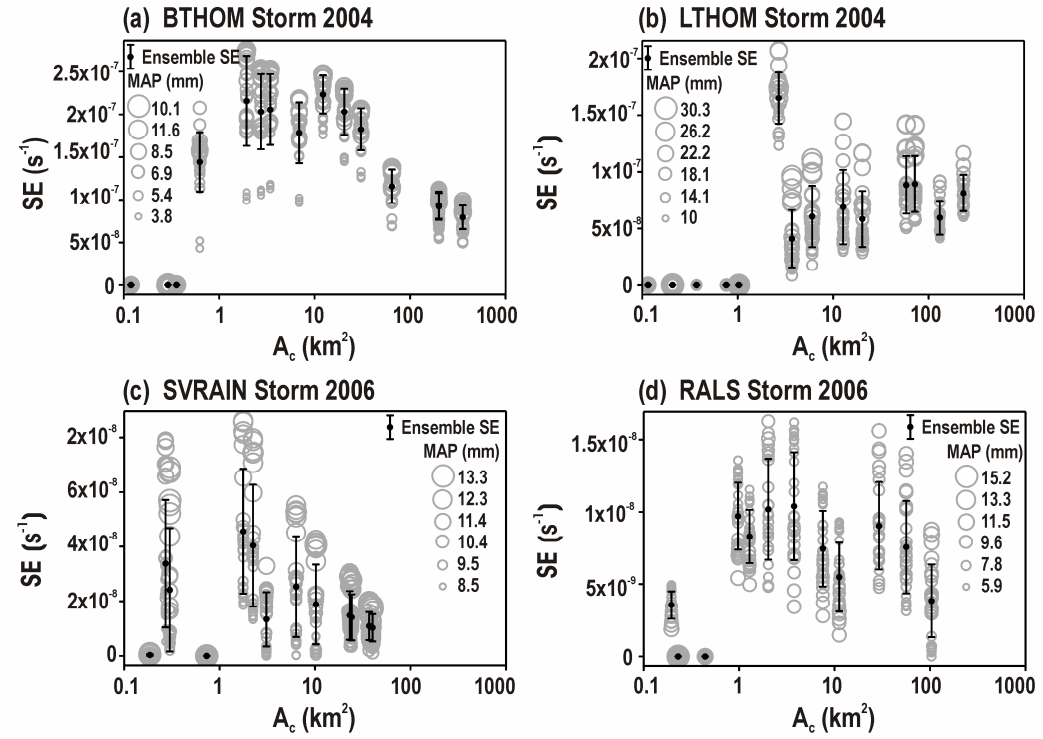

Figure 4.11. Relation between Specific Error (*SE*) and catchment area (A_c) in four selected basin and storm pairs for a lead time of 180-min. Gray circle size depicts *MAP*, while dots and vertical bars show the ensemble mean and ±1 standard deviation of SE at each location.

Figure 4.11 presents *SE* as a function of A_c at four representative watershed and storm pairs for a lead time of 180-min. The selection of this lead time enhances the visualization of the scale-dependency, though similar patterns are observed at other lead times. Selected internal channel locations span a range of catchment areas and are nested along a downstream path from the storm cores to the outlet in each basin. As illustrated in these cases, the scale dependence of *SE* reveals interesting patterns across all watersheds with a bell-shaped variation with A_c. This trend tends to be clearer in large basins (BTHOM, NFORK, LTHOM, BUCK), whose watershed area can entirely capture the occurrence of

typical convective storms. Note that *MAP* (gray circle size in Fig. 4.11) can have larger values at small and intermediate spatial scales, but decreases with basin area beyond approximately 100 km^2, as a result of the smoothing of precipitation fields when integrated over large areas. Results indicate the presence of reduced *SE* properties at small scales, subsequent increases in the mean and dispersion of *SE* at intermediate-sized basins and posterior reductions in *SE* at the basin outlets. We believe this pattern is intimately linked with the spatial distribution of runoff production within the watershed as dictated by the typical size of convective systems over the mountains and the underlying watershed properties (see Appendices E and F).

To help interpret these results, Figure 4.12 shows SE/SE_{max} and their corresponding ϕ/ϕ_{max} values, for the same watersheds in Fig. 4.11, with the different symbols representing distinct lead times. SE/SE_{max} is the ratio between the *SE* and the maximum *SE* (SE_{max}) across scales for the same lead time and watershed-storm pair. SE/SE_{max} values are normalized and preserve the patterns with A_c shown previously. The estimation of ϕ/ϕ_{max} follows an analogous description for each basin-storm pair and lead time. An interesting pattern is observed, which is in accordance with preliminary observations on runoff production areas and rainfall distribution. SE/SE_{max} has a proportional relation with ϕ/ϕ_{max} that is replicated for all lead times. Thus, areas in the watershed with ϕ/ϕ_{max} close to 1 that present high runoff productions tend to exhibit higher errors and more limited flood predictability.

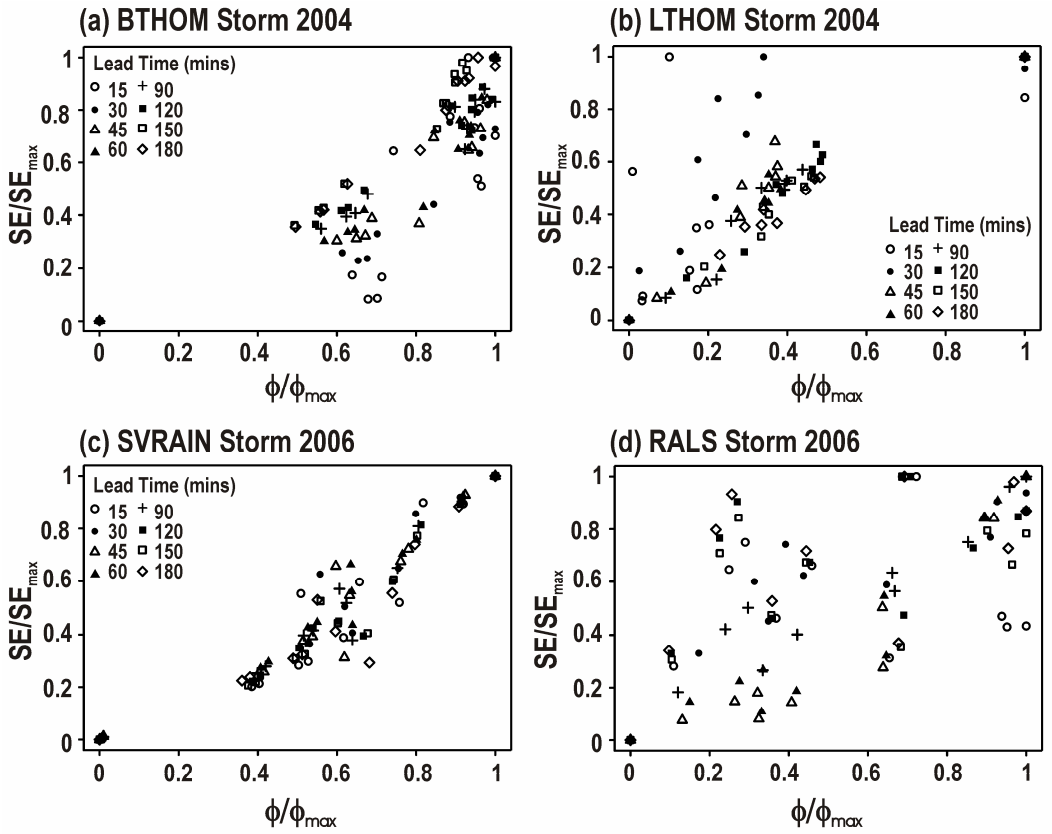

Figure 4.12. Normalized Specific Error (SE/SE_{max}) as a function of normalized runoff coefficient (ϕ/ϕ_{max}) for all lead times in four selected basin and storm pairs.

These cases occur for intermediate scales where the full geographic cover of the storms is superimposed on the basin areas (see Appendix E). Conversely, low and intermediate ϕ/ϕ_{max} values can be attributed to small and large basin areas, whose errors are smoothed by watershed characteristics, the spatial aggregation occurring in the mean areal precipitation and the more limited presence of runoff production in these areas. To generalize the patterns across watersheds, Figure 4.13 compiles the ensemble mean (μ) and standard deviation (σ) of normalized *SE* for three different basin groups organized by similar areas

for coincident storm periods. These results indicate that at small A_c (0.1 to 1% of total area) a low μ and σ are present. This is due to a relatively large *MAP* that is unaffected by areal smoothing and by the small Q_R as watershed characteristics mitigate the impact of QPF errors. At intermediate A_c (up to 5 or 10% of the total area, depending of the basin), increased μ and σ are observed as this scale range corresponds to the typical size of warm-season convective systems in the region that lead to intensified runoff production in these areas (see Appendices E and F). Sub-basins of this size present a higher and more variable Q_R under heavy precipitation. Under these conditions, watershed characteristics, such as areas of low permeability and high slopes, trigger variable runoff and streamflow responses. At large A_c (from 10% to total area), lower μ and σ are caused primarily by a significant reduction in Q_R due to the integration effects of the channel network as the flood wave propagates (Vivoni et al. 2006; Mascaro et al. 2010a), but also by the reduced fraction of runoff producing zones as a fraction of total area, which also decreases the total uncertainty. As a result, the typical size and organization of warm-season convection as well as the watershed runoff production characteristics play a fundamental role on the scale dependence of specific errors in streamflow. We might expect that other type of rainfall systems or basins have a different functional relation between these normalized quantities.

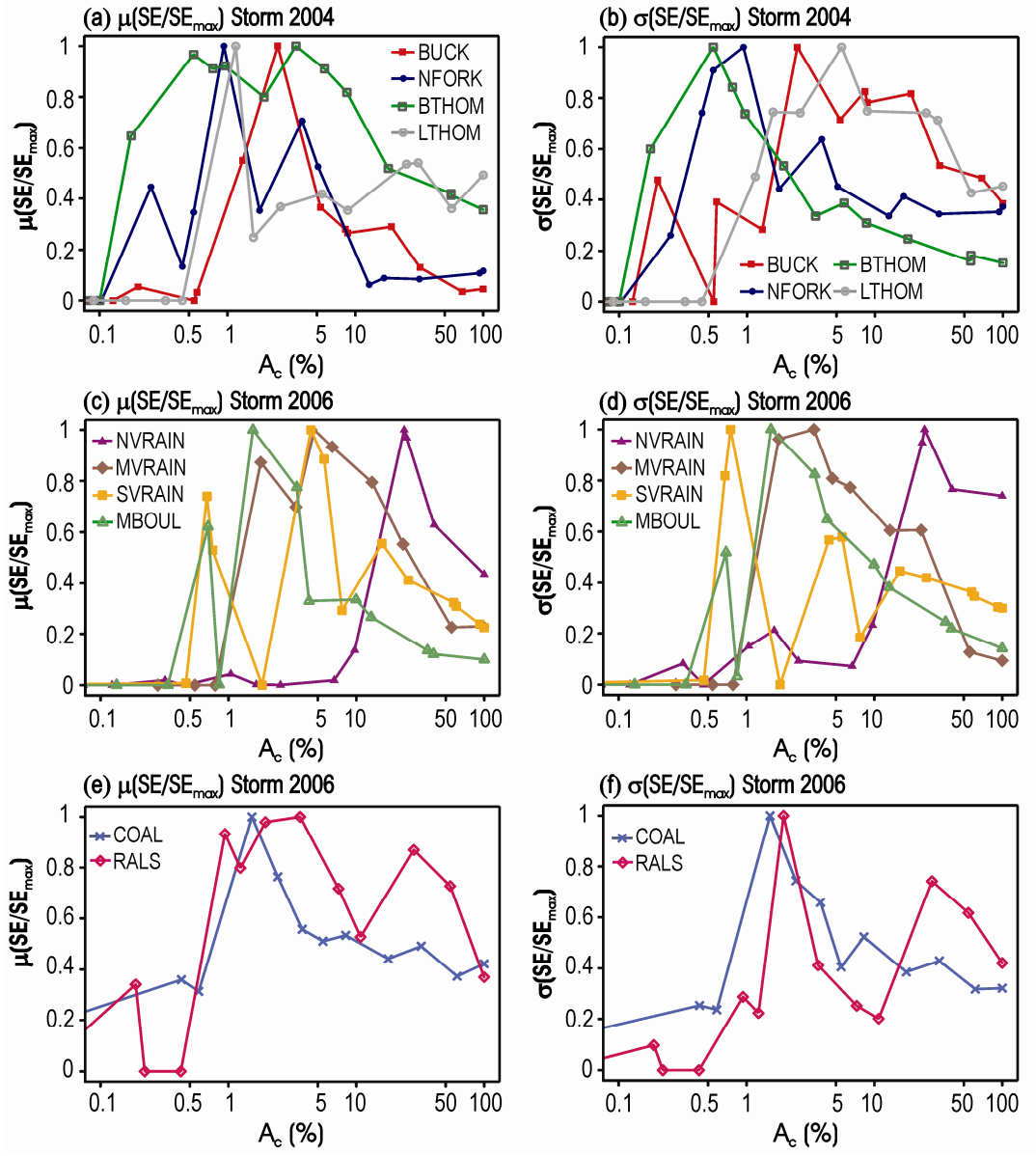

Figure 4.13. Relation between normalized Specific Error (SE/SE_{max}) properties (ensemble mean, μ, and ensemble standard deviation, σ) and the normalized catchment area (A_c in %) in three watershed groupings with similar sizes and behaviors.

Residual Errors from Model Structural and Parametric Uncertainty

While flood forecasting skill clearly decreases due to QPF errors, other sources of model uncertainties also affect the total forecast error with respect to

observed streamflows. Figure 4.14 presents the ensemble mean *RMSE* of the flood forecasts with (1) the model simulations driven with QPEs ($RMSE_{QPE}$, gray bars) and (2) the observed streamflows ($RMSE_{obs}$, black bars) at each basin outlet for two lead times (15 and 180-min). Clearly, the magnitude of both type of errors increases with lead time in all basins. As expected, $RMSE_{obs}$ are typically greater than or equal to $RMSE_{QPE}$. If we consider the total hydrologic uncertainty to be compound by three terms such that $X_1+X_2+X_3=100\%$ and whose terms represent the model parameter uncertainties (X_1), the model structural errors (X_2) and the rainfall input uncertainties (X_3), we can conduct an analysis of relative error contributions with lead time during both storms. For each basin and lead time, differences between $RMSE_{obs}$ and $RMSE_{QPE}$ can be considered as residual errors caused by model structural or parametric uncertainty (X_1+X_2) that we will call X_{12}. Residual errors (X_{12}) tend to be small for Storm 2004 as a result of the model calibration, but grow substantially for Storm 2006, reaching values that exceed the magnitude of $RMSE_{QPE}$ (X_3) in some basins (e.g. BUCK, BTHOM, LTHOM, NVRAIN, SVRAIN, MVRAIN, MBOUL, COAL, RALS, for a lead time of 15 minutes). Up to certain point we could consider residual errors in storm 2004 dominated by model structural uncertainties (X_2), while errors in 2006 are a consequence of model parameter, initial conditions and structural errors (X_{12}). During storm 2004, flood forecasting errors are primarily due to QPF uncertainty as evidenced by the reduction of X_{12} and the overall increase in X_3 between the 15 and 180-min lead times. In-depth analysis allowed concluding that $X_3>X_{12}$ for lead times beyond 30 to 45 minutes in Storm 2004 across all watersheds.

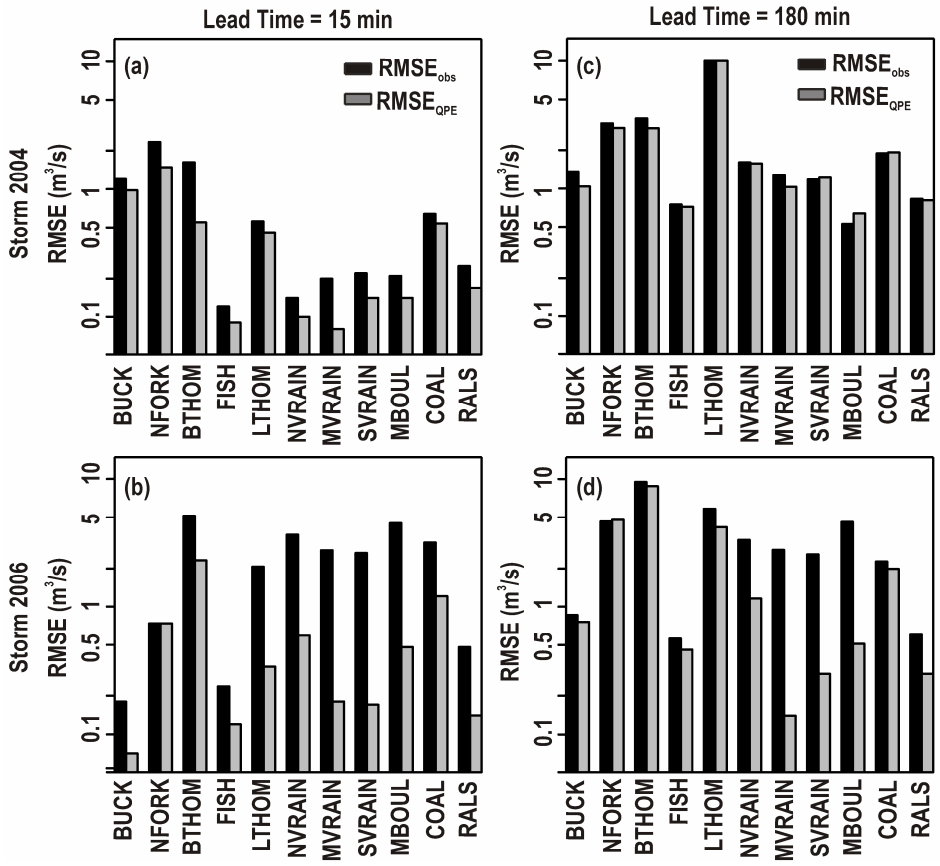

Figure 4.14. Comparison of streamflow errors at basin outlets derived from flood forecasts relative to observed hydrographs ($RMSE_{obs}$, black bars) and simulations using QPEs ($RMSE_{QPE}$, gray bars) for lead times of 15 and 180-min for each storm period.

Meanwhile, the verification period in Storm 2006 exhibits larger X_{12} at the 15-min lead time, as compared to the calibration period, due to the presence of model structural and parameter uncertainty for this event. Interestingly, residual errors are significantly reduced at a lead time of 180-min for Storm 2006 at the expense of an increase in uncertainty introduced by QPF errors (X_3) in some watersheds but at different threshold lead times. The watersheds and lead times at which $X_3 > X_{12}$ in Storm 2006 are presented next: BUCK(60 min), BTHOM(45 min), FISH(45 min), LTHOM(90 min), COAL(30 min) and RALS(45 min).

Conversely, snow dominated watersheds (NVRAIN, MVRAIN, SVRAIN, MBOUL) are consistent to show $X_{12}>X_3$ across all lead times as another demonstration of parameter and structural error dominance on the total hydrologic uncertainty.

As a result, we can conclude that uncertainty sources other than nowcasting errors can worsen flood forecast skill at small lead times for verification periods. Undoubtedly, these differences are less notable at larger lead times since precipitation forecasting errors increase. Nonetheless, in some basins, residual errors continue to be the largest contributor to total flood forecast errors during the verification exercise, suggesting that a single-event model calibration introduces additional sources of uncertainty even after the initial condition has been adjusted.

SUMMARY AND CONCLUSIONS

In this study, we investigated the propagation of radar nowcasting errors into distributed flood forecast skill in eleven mountain watersheds and their internal locations during two storm periods in 2004 and 2006 in the Colorado Front Range. This region is known for its propensity of summer convective precipitation that triggers significant floods in individual basins. We utilized high-resolution radar observations to produce nowcasts from the NCAR TITAN algorithm for lead times ranging from 15 to 180 minutes. Using the tRIBS model, we quantified the resulting flood forecast skill as a function of lead time and catchment area. The distributed model allowed depicting the spatial patterns in basin response that explain local differences in flood forecast skill introduced by

the distributions of rainfall and watershed properties. For this purpose, we evaluated regional QPF errors relative to the radar-based QPEs, quantified the dependence of flood forecasting skill on lead time at basin outlets, and identified the scale dependence of flood forecast errors at nested sub-basins with different upstream areas. An emphasis was placed on obtaining a detailed picture of the rainfall-runoff error propagation through normalized metrics that removed the effect of the basin area and mean areal precipitation. We also quantified how rainfall forecast errors interacted with parametric and structural uncertainty through comparisons of the calibration and verification periods. The results of the study indicate the following:

(1) Radar nowcasting skill decreases with lead time and rainfall magnitude across the CFR, with the most noticeable reduction in forecast skill occurring between 15 and 45-min lead times. For both storm periods, the radar nowcasts tend to overestimate precipitation values, increasing the number of false alarms, in particular for large forecast lead times.

(2) Flood forecasting skill also decreases with lead time, but the functional forms follow a different pattern as a result of the interaction with watershed properties, in particular when rainfall intensities exceed hydrologic thresholds. For these storm periods, flood forecasting skill is not better than the forecasted mean for lead times greater than 30-min. Snowmelt-dominated basins have a more limited impact of rainfall uncertainties on the predicted discharges.

(3) Watershed properties in conjunction with storm characteristics play a determinant role on the differential susceptibility to high runoff production and

flooding. Rainfall-runoff maps show that, despite changes in the spatial distribution of QPFs with lead time, only variations in runoff magnitude are triggered. Analyses of precipitation and streamflow errors also indicate a low correspondence between those variables across different scales, suggesting that the scale-dependence of streamflow errors is primarily due to increasing flood magnitudes.

(4) A characteristic pattern was revealed in the scale dependence of specific error (*SE*) at different lead times. Basin areas coinciding with the typical size of convective storms experience the highest flood forecast errors with the largest differences among ensemble members. Thus, intermediate-sized basins have more limited flood predictability. Watershed properties dictate the shape of the scale-dependence as they control rainfall error propagation downstream and modulate the ensemble dispersion across watersheds and lead times. Although *MAP* is removed from the analysis, precipitation patterns have a principal role in the differential runoff responses.

(5) In comparison to rainfall forecast errors, the uncertainties related to model parameters and structural errors can reach similar orders of magnitude in particular for small lead times. At large lead times, QPF errors tend to reduce flood forecasting skill more significantly in most watersheds, though residual errors can remain important in some cases when model structural and parametric uncertainties amplify the disparities in forecasted discharges.

The results of this study are based on the use of a distributed hydrologic model that was calibrated during a storm period in 2004, independently for each

basin using a Level II 1-km, 15-min radar product (Moreno et al. 2012b). Initial conditions were then adjusted for a verification period in 2006. While single-event model calibration is not ideal for operational settings, it offers the possibility to quantify the errors introduced by rainfall forecasts, independent of model structural and parametric uncertainty. Results are primarily shown relative to model simulations forced with QPEs that we consider as the ground truth. We demonstrated the benefits of using distributed hydrologic models to produce flood forecasts from radar nowcasting since these allow identifying spatial runoff errors and their scale dependence along the channel network. We found that the interaction of QPF and watershed characteristics lead to a distinct patterns in flood predictability with greatest errors in intermediate-sized basins. High mean areal precipitation and watershed features tend to reduce the flood forecast uncertainties in small catchments, while channel routing and the areal aggregation of storm systems are responsible for reduced errors in large basins. This scale dependence illustrates the spatiotemporal limits of flood predictability in mountain catchments under summer convection. Additional studies on this dependence in different environments and precipitation regimes are needed to generalize these findings.

Chapter 5

SYNTHESIS AND FUTURE WORK

This study presents quantitative analyses based on observed and modeled data, intended to improve the current body of knowledge on flood forecasting in mountain catchments undergoing summer convection. Research findings are applied to the Front Range region in Colorado at eleven watersheds, whose high availability of hydrologic and meteorological information provides opportunities for exploring gains and shortcomings of the current and future operational capabilities. Our efforts combined the collection, geo-referencing, and evaluation of ten QPEs (1 h, 4 km) from different sources (including rain gauges) for summer 2004, the mosaicking and production of regional (5-min, 1km) NEXRAD-Level II precipitation fields, whose *Z-R* relation was calibrated using hourly rain gauge time series at multiple sites within the CFR, and the production of ensemble precipitation fields for two storm systems in 2004 and 2006, for different lead times, using the NCAR- Thunderstorm Identification, Tracking, Analysis, and Nowcasting (TITAN; Dixon and Wiener 1993) algorithm. Through all the chapters, quantitative analyses of precipitation are accompanied by hydrologic simulations using the Triangulated Irregular Network (TIN)-based Real-time Integrated Basin Simulator (tRIBS; Ivanov et al. 2004), a physically based model that was calibrated to provide confidence in results. Use of a distributed model provided gains in tracking the spatio-temporal evolution of watershed responses, water balances, runoff mechanisms, rainfall error propagation, scale and land surface effects on forecasting uncertainties, and flood

wave propagation through the channel network. Here I summarize the main findings from this research and identify directions for further work.

UTILITY OF QPEs FOR FLOOD FORECASTING

The analysis presented in Chapter 2 constitutes an extensive inter-comparison effort, in terms of the number of gridded QPE products (ten) from different sources (e.g. satellites, radar, multisensor, rain gauges) with posterior hydrologic verification at multiple mountain watersheds. Both QPE and their distributed runoff responses presented critical differences that are linked to the inherent characteristics from the type of sensor and precipitation estimation methodology in a region of manifest complexity for hydrologic modeling purposes.

The hydrologic utility of the various QPEs was tested in terms of point rain gauges and hydrologic simulations based on a rain gauge calibrated NEXRAD product that we considered as “ground truth”. Results are definitive to outline the convenience of using distributed precipitation products into distributed hydrologic models, as the spatio-temporal variability of streamflow responses is adequately captured by this coupling. Relative to rain gauge forcing, radar and multisensor QPEs that capture intensity and spatial variability of precipitation, especially intense localized storms, show advantages in terms of runoff prediction. This capability is due to the fact that radar systems, the base for multisensor and NEXRAD data, scan vertical profiles that describe storm morphology, attaining better accuracies when estimating rainfall fields through *Z-R* relations. On the other hand, satellite products, whose cloud top temperature-

rainfall intensity relations are weak and do not retain reflectivity values at different atmospheric levels, tend to present small biases that translate in underestimation. Nonetheless, most satellite estimations capture relatively well the spatial distribution of rainfall, an important attribute for flash-flood forecasting purposes. This is reflected in the fact that despite that satellite QPEs, underestimate total discharge volume and introduce errors from their smoother and lower magnitude rainfall fields, they show better performance than rain gauges with respect to geographically localized streamflow responses, timing and volume for most cases, indicating their value for hydrologic forecasting in mountain areas. The reason why rain gauges do not attain the best hydrologic skills when used over vast areas of high spatial variability of precipitation is the assumption of uniform rainfall over the basin that originates false flood alarms in locations without much runoff but, most dangerously, underestimation of streamflows in areas where intense-localized storms are occurring. The described effect also influences the timing and magnitude of predicted hydrographs at the basin outlet, commonly overestimated by rain gauges. Other findings in this chapter reveal that QPEs preserve the seasonal spatial occurrences of different runoff mechanisms and the magnitude of the components of the water balance. A scaling relation between spatial rainfall and runoff production ($CV_{ratio} = c\phi^{a}$) across watersheds suggested its applicability across a wide range of basin conditions and illustrated the profound differences between distributed and rain gauge types of inputs for distributed hydrologic modeling. Although findings in

this study are clear for summer 2004, new studies are envisioned that include more summer seasons in the analysis.

IMPORTANCE OF USING SITE SPECIFIC Z-R RELATION IN RADAR NOWCASTING

Despite radar-based products are one of the most accurate sources of high resolution precipitation, constituting the basis of most nowcasting systems, they are still expected to carry significant uncertainty during the prediction of floods. This research section dealt with the quantification of uncertainties introduced in hydrological forecasts when using a radar product whose rainfall generating algorithm has not been adequately calibrated for a specific region. The reflectivity-rainfall relation (*Z-R*) is the fundamental expression to convert radar sensing into rainfall intensity, but that has been demonstrated to change between regions and storm types. We show the convenience of not using default operational relations and instead we propose a methodology based on seasonal rain gauge calibration (that includes periods of rainfall and no rainfall) during multiple summer seasons whose hydrologic results confirm its benefits for hydrologic forecasting. We conclude that flood forecasting efforts with radar forcing in mountain watersheds benefit from establishing a site-specific relation Z-R (e.g. $Z=700R^{1.3}$) for the season of interest using comparisons with local observations. We show that the use of an arbitrary *Z-R* relation impacts the basin response in terms of the outlet streamflow, runoff mechanisms and the seasonal water balance. As a consequence, rainfall differences in the WSR-57 and NEXRAD relations, relative to the reference case, result in higher streamflow

errors, gradual transitions in runoff mechanisms, and large changes in the water balance.

A distributed analysis of hourly simulations at four watersheds during summer 2004 demonstrated that the use of an incorrect *Z-R* generate profound changes in the estimation of rainfall intensities which lead to streamflow error generation at different zones in the basin. Differences in rainfall translate into uncertainties in streamflow that follow power law expressions beyond a particular threshold. Similarly, streamflow uncertainty is described by a power law regression with discharge magnitude. Both relations indicate that errors introduced by the *Z-R* relation into the basin response are exacerbated for large rainfall or flooding events. Another encouraging finding of this chapter relates to the behavior of specific streamflow errors (SE) whose magnitudes are exacerbated principally at intermediate-sized basins by the use of inappropriate *Z-R* relations. This finding coincides with the preliminary remarks on the importance of capturing the spatial distribution of localized but intense precipitation systems and its relevance for accurate flood forecasts.

SPATIOTEMPORAL LIMITS OF FLOOD FORECASTING IN MOUNTAIN BASINS

In Chapter 4, interesting results were found regarding the predictability of flash floods in multiple watersheds under heavy summer precipitation. The scale and lead time dependence of forecasting skill was investigated by means of ensemble radar nowcasts into a hydrologic modeling environment whose extended lead mode allowed having a continuous description of the rainfall-runoff

fields during consecutive storm systems, a critical aspect when predicting multiple peak or superimposed floods. The study of two storm systems in summers 2004 and 2006 allowed recognizing typical forecasting error patterns in precipitation and streamflows that are due to the incapacity of nowcasting models to correctly predict the evolution of rainfall in mountains and the added complexity of watershed properties in the re-distribution of runoff, determined by soils, vegetation, aquifer and channel routing characteristics.

Results indicate that using a physically-based hydrologic model with distributed rainfall predictions, provides a vantage point for recognizing spatial patterns that explain local susceptibility to floods and provide an opportunity to quantify error propagation from the occurrence of the storms and subsequent basin responses. An independent rainfall analysis allowed concluding that probability of predicting precipitation decreases with lead time and rainfall magnitude. Across the CFR region, the most noticeable decrease in prediction skill occurs between 15 and 45 min. Consistently, hydrologic simulations revealed that, except by some small-size, snow-dominated basins, flood forecasting skill is not better than forecasted mean for lead times greater than 30 minutes in most of the cases. Flood forecasting skill also decreases with lead time, but the functional forms follow a different pattern as a result of the interaction with watershed properties, in particular when rainfall intensities exceed hydrologic thresholds.

Storm scale characteristics play a determinant role on the differential susceptibility to high runoff production and flooding. Rainfall-runoff maps show that, despite changes in the spatial distribution of QPFs with lead time, only

variations in runoff magnitude are triggered. Analyses of precipitation and streamflow errors also indicate a low correspondence between those variables across different scales, whereas that the scale-dependence of streamflow errors is primarily due to increasing flood magnitudes.

The consideration of forecasted ensemble members at internal channel locations permitted the quantification of specific error (*SE*) and its dispersion that follow a characteristic pattern with basin area across watersheds at different lead times. We found that catchment areas that coincide with the typical size of convective storm systems experience the highest and more disperse values of *SE*, making predictability more dificult at these scales, principally due to an increase in runoff production that result in larger runoff coefficients. In addition, we attribute to soil hydraulic characteristics, topography, vegetation interception and channel routing processes the bell-shaped pattern of normalized *SE* in function of total area, as they control the propagation of the rainfall errors and moderate the forecasting dispersion across watersheds and lead times.

Overall, the unifying theme of this research "flood forecasting in mountain basins under summer convection" was developed through three independent but complementary analysis: (1) exploration of the utility of different QPE in multiple mountain basins by using hydrologic verifications through observed streamflows; (2) study of the influence of the reflectivity-rainfall relation on hydrologic simulations in multiple catchments; and (3) analysis of the scale and lead time dependence of flood forecasting skill during significant events in multiple mountain catchments. Consistently through the Chapters, results pointed out the

need for considering spatial variations in rainfall inputs for improving the accuracy, in time and magnitude, of the streamflow forecasts. Three examples of this are (1) the fact that satellite observations whose distributed nature might overcome the presence of volume biases for hydrologic simulations, (2) the need for regional calibration of the Z-R relation whose rainfall structures are determinant of the prediction error magnitudes, and (3) the fact that at large lead time QPF commonly distort the actual spatial distribution of precipitation leading to serious limitations in hydrologic forecasting at internal and outlet locations. Another important conclusion remarked the high temporal variability in the occurrence of rainfall that was linked to their high spatial intermittency as another limiting factor for prediction. As a result the nowcasting model was unable to issue accurate forecasts beyond 30 minutes in most watersheds, a demonstration of a chaotic evolved field with low persistency in time. Two final elements outcrop as common denominators in this analysis. One is the obvious influence of watershed characteristics in triggering different runoff mechanisms and differential runoff production that determines geographic flood susceptibility inside a watershed, which is more clearly explained in Chapter 4. The second is the scale of summer precipitation occurrence in the CFR determines the de degree of uncertainty of flash-flood forecasting at different basin scales. Two clear examples of this were presented in Chapters 3 and 4 through seasonal and event scale analyses of specific error functions (SE) across cumulative basin areas in multiple watersheds.

FUTURE WORK

Future work section is divided in elements for real-world applicability of discussed methodologies and further research opportunities. The procedures and approaches used through this research work can be applied in other applications to advance this field with the upcoming potential in computational (supercomputing) and sensing instruments (dual-polarization radars, NASA satellites).

First, QPE verification methodologies can be adopted not only to evaluate summer QPE products but also long-term time series that include winter and spring precipitation events that are equally significant in terms of the hydrologic responses. We encourage the testing of QPE in other regions over the globe whose propensity to flooding is year-long. One of the unavoidable prior steps before this type of verification is the existence of a relatively high number of rain gauges (at 1-hour time resolution or finer) permitting a fairly good representation of the spatial variability of rainfall over the region. Ideally, ground stations are expected to be installed at different elevations, landcover types and micro-topographic characteristics (e.g. windward or leeward faces) according to the general circulation patterns in the region. Selection of study watersheds must follow the presence of high resolution stream gauges (at least 1 hour time resolution), soils, landcover and aquifer characteristics. It is recommendable that the hydrologic verification is done in multiple size watersheds at different elevations, so that distinct hydrologic dynamics are taken into account. Outcomes from these analyses can lead to potential use of QPE products for areas with sparse rain gauge or no-rainfall information with hydrologic similarity. Some

drawbacks of this methodology involve the fact that areas of low rain gauge or streamflow coverage are very unlikely to support this type of studies as the high spatial variability of rainfall determines the overall accuracy of results.

Second, the methodology developed to determine a regional Z-R relation is straightforward to implement in areas whose high presence of rain gauge stations guarantees the capture the spatial variability of rainfall. As discussed before, for practical purposes, we recommend a seasonal calibration procedure so that both dry and wet periods are considered in the analysis. The approaches combine the use of available high resolution time series of precipitation and streamflow at multiple catchments within a same region with weather radar coverage. Benefits from the application of this methodology can be summarized in more accurate QPE from radar measurements that translates in improvement of QPF. This all translates in better hydrologic representations and predictions in terms of runoff and streamflow production at internal and outlet locations. Some of the limitations of this methodology are the fact that it is only possible in areas where multiple rain gauges are present, multiple watersheds are instrumented (streamflow gauges) and usage in areas of medium geographic coverage, depending on the rainfall variability and physiographic conditions (e.g. mountain block like the CFR, or a flat area with similar hydrologic characteristics).

Third, the applicability of coupled nowcasting techniques and distributed hydrologic models is a feasible task given (1) the new capabilities of supercomputing facilities that make computations fast and efficient, (2) the improvement of distributed hydrologic models and rainfall prediction algorithms,

(3) the availability of distributed ground data (e.g. soils, vegetation, channel networks, groundwater systems, etc), (4) the automatization of techniques to calibrate and quality control model outputs and (5) the new capabilities for real-time observations using telemetry and satellite data that help substantiate predictions. The cost of a coupled precipitation-distributed model setup like this one becomes insignificant if we take into account the benefits in preventing floods with billions in damages. Additionally, advantages like the knowledge of watershed dynamics at internal locations and the enhanced prediction capabilities at nested basins turn this system in a real beneficial alternative for issuing flood forecasts. As in lumped models, questions dealing with parameter calibration and adjustment of the initial condition will need to be considered by the appropriate personnel operating the system. Some of the drawbacks or opportunities for improvement can be the design of techniques to simplify model overparameterization, the need of supercomputing systems and the mounting of an expert platform and team that deals with hydrologic issues of model uncertainties and real-time issuing of watches.

The results obtained in this study encourage the development of new research topics in seek of generalization of findings, exploration of new particular cases and the modeling of future flood forecasting scenarios under climate and land cover changes. I summarize eleven possible new avenues of work, although many more can be foreseen by other researchers:

1. As the availability of precipitation data from satellites is dramatically increasing and will continue to do so with the new platforms such as the Global

Precipitation Mission (GPM) and the National Polar-Orbiting Environmental Satellite System (NPOESS), new hydrological verification studies will be needed, at different types of watersheds (e.g. subtropical mountains and plains, tropical forests, agricultural, urban areas, etc) so that operational communities get directions on the value of using those products for accurate hydrologic estimations.

2. Due to its coarse space-time resolutions, some current and upcoming satellite QPE show a lack of spatial structures which reduces the accuracy of hydrologic simulations in medium to small-size catchments. An approach to overcome this limitation is the use of statistical downscaling models that are able to reproduce the statistical properties of fine-scale rainfall fields with minimal parameterization. Downscaling techniques have been recognized to reproduce rainfall variability in different regions (Deidda et al. 1999; 2004; Badas et al. 2006; Mascaro et al., 2008; Forman et al. 2008). The use of orographic modulating functions to distribute rainfall according to elevation gradients controlled by the diurnal cycle of precipitation, introduces a topographic-diurnal organization framework to the downscaled rainfall in a similar manner as shown by Badas et al. (2006). Hydrologic model can be used as a verification of downscaled fields.

3. This study showed the value of multisensor and satellite products for high resolution hydrologic simulations. However, more effort is needed in new techniques to correct local biases that improve their suitability for flood forecasting in mountain areas. This task can be done by utilizing current ground

information (or rain gauge calibrated radar fields) that serve to correct QPE at collocated pixels to extract elevation and diurnal cycle dependence functions that allow correcting for systematic volume biases. This will make satellite products applicable to areas of no other information.

4. The type of approach used for deriving the Z-R relation constitutes one feasible method to obtain it at the seasonal scale, based on the optimization of one objective function composed of two weighted error and skill metrics. An opportunity to test many more types of objective functions and preference structures (weighting) could be adopted to test the robustness of its derivation. Also, a sensitivity analysis can be conducted to test the influence of considering different number of rain gauges on the ground, so that a panoramic of Z-R sensitivity is revealed in terms of both readily available information and type of optimization function.

5. Flood forecasting skill functional relationship with lead time should be tested for other types of precipitation (e.g. winter stratiform) at the study basins. In this case we demonstrated that forecasting skill does not have further worsening beyond 120 minutes lead time. So, National Weather Prediction (NWP) models like WRF, whose smaller lead time is 6 hours are expected to have low utility for the case of flood forecasting. However, in other geographic regions, where precipitation fields show larger persistency (Great Plains under winter precipitation), NWP models can be tested to reveal their validity for high resolution rainfall forecasts.

6. Residual errors in the forecasting chain (those provided by model structure and parameters) need to be separated and quantified by their compounding fractions through model inter-comparison experiments with the same setup in terms of forcing, basin characteristics, observed streamflows, and calibration procedures. In the end, if models have been correctly calibrated they are able to issue flood forecasts with a good degree of accuracy, but only those whose conceptual framework is solid will be introducing smaller amount of uncertainty in the simulation of floods. A subsequent step will test the model uncertainty introduced by behavioral parameterization, by taking the top 10% of best parameter sets. In other words, introduction of the uncertainties by the presence of non-uniqueness of solutions through different combination of parameter sets will allow quantifying its error contribution. Total error is thus the combination of both parameter uncertainty and model structural errors. Having both types of uncertainties computed, the difference between the two errors (from the behavioral analysis and calibration) can be estimated in both models to estimate the effect of parameter uncertainties alone.

7. Recent forest fires in the north CFR (in June 2012) envision a change in the hydrologic patterns that might involve an increased propensity to floods. Given that this study provides a base simulation platform, new studies are envisioned on the effect of this land cover change on the hydrologic response to significant summer storm events. Objectives can address topics like the importance of land cover to mitigate floods, the switch in runoff mechanisms,

changes in the partitioning of the water balance and the forecasting dispersion introduced by drastic cover changes in mountain areas.

8. We foresee more research on the specific error function (*SE*) and its possible presence in geographically distinct watersheds under different rainfall types. Additionally, we expect interesting *SE* trending patterns under heavier precipitation scenarios and landcover changes. We expect that this relation increase in magnitude as large storms and urbanization take place in future scenarios.

9. For larger watersheds involving reservoirs, tRIBS has great challenges to improve its current modeling capabilities by including operation schemes and lake routing when floods occur in large-scale basins (e.g. Verde, Salt, Grande, Colorado or Mississippi Rivers). In doing so, dam operators will play a significant role in mitigating flood avenues by following the simulations projected by the hydrologic model.

10. In urban areas the coupling of nowcasting and hydrologic models is possible by including the details of artificially created channel networks (e.g. streets, waysides and storm retention structures) as well as the hydrologic complexities that determine timing and magnitude of total response. Exhaustive work on feasible values for land cover and soil parameterization in urban environments is needed. Challenges for the rainfall forecasts might not be as difficult as in mountain systems. However urban meteorology, including urban island effects on precipitation can impose limitations to the correct prediction of rainfall distribution.

11. Distributed values of rainfall, soil types, vegetation coverage and coupled vadose-saturated zone interactions for soil moisture development are a great opportunity to landslide forecasting. Distributed hydrologic models can now be seen as platforms for development of associated risks. However, significant amount of work is envisioned in testing the model in experimental steep slope watersheds under slide vulnerability particularly during persistent rainfall periods.

12. Floods have demonstrated to be one of the most important producers of erosion and sediment transport in rivers. Changes in the fluvial geomorphology are expected to affect the ecosystem dynamics and hydrologic responses themselves. So, coupling of tRIBS with distributed sediment transport models are envisioned to predict changes in the channel network morphology and sediment equilibrium induced by significant streamflow values.

REFERENCES

Alfieri, L., Claps, P., Laio, F., 2010. Time-dependent *Z-R* relationships for estimating rainfall fields from radar measurements. *Nat. Hazards Earth Syst. Sci.* 10, 149-158.

Arduino, G., Reggiani, P., Todini, E., 2005. Recent advances in flood forecasting and flood risk assessment. *Hydrol. Earth Syst. Sci.* 9, 280-284.

Arnaud, P., Bouvier, C., Cisneros, L., Dominguez, R., 2002. Influence of rainfall spatial variability on flood prediction. *J. Hydrol.* 260, 216-230.

Ashley, S.T., Ashley W.S., 2008. Flood fatalities in the United States. *J. Appl. Meteorol. Clim.* 47(3), 805-818.

Ba, M., Gruber, A., 2001. GOES multispectral rainfall algorithm (GMSRA). *J. Appl. Meteorol.* 40, 1500-1514.

Baek, M.L., Smith, J.A., 1998. Rainfall estimation by the WSR-88D for heavy rainfall events. *Weather Forecast.*, 13, 416-436.

Bartholomes C., Todini, E., 2005. Coupling meteorological and hydrological models for flood forecasting. *Hydrol. Earth Syst. Sci.* 9, 333-346.

Bear, J., 1972. *Dynamics of Fluids in Porous Media*. New York: Elsevier.

Benoit, R., Pellerin, P., Kouwen, N., Ritchie, H., Donaldson, N., Joe, P., Soulis, E. D., 2000. Toward the use of coupled atmospheric and hydrologic models at regional scale. *Mon. Wea. Rev.* 128, 1681–1706.

Berenguer, M., Corral, C., Sánchez-Diezma, R., Sempere-Torres, D., 2005. Hydrological validation of a radar-based nowcasting technique. *J. Hydrometeorol.*, 6, 532-549.

Beven, K.J., 1982. On subsurface stormflow: An analysis of response times. *Hydrol. Sci. J.* 27, 505-521.

Birkeland, P., Shroba, R., Burns S., Price A., Tonkin, P.J., 2003. Integrating soils and geomorphology in mountains: an example from the Front Range Colorado. *Geomorphology* 55, 329-344.

Bongioannini, P.C., Emanuel, K.A., Todini, E., 2005. Orographic effects on convective precipitation and space-time rainfall variability: preliminary results. *Hydrol. Earth Syst. Sci. 9,285-299.*

Bouilloud, L., Delrieu, G., Boudevillain, B., Borga, M., Zanon, F., 2009. Radar rainfall estimation for the post-event analysis of a Slovenian flash-flood case: application of the mountain reference technique at C-band frequency. *Hydrol. Earth Syst. Sci.* 13, 1349-1360.

Boushaki, F., Hsu, K.L., Sorooshian, S., Park, G., Mahani, S., Shi, W., 2009. Bias adjustment of satellite precipitation estimation using ground-based measurement: A case study evaluation over the southwestern United States. *J. Hydrometeor*. 10, 1231–1242.

Bowler, N.E.H., Pierce, C.E., Seed, A., 2004. Development of a precipitation nowcasting algorithm based upon optical flow techniques. *J. Hydrol.* 288, 74-91.

Cabral, M. C., Garrote, L., Bras, R.L., Entekhabi, D., 1992. A kinematic model of infiltration and runoff generation in layered and sloped soils. *Adv. Water Resour*. 15, 311–324.

Carpenter, T., Georgakakos, K., 2004. Impacts of parametric and radar rainfall uncertainty on the ensemble streamflow simulations of a distributed hydrologic model. *J. Hydrol.* 29, 202-221.

Castillo, V., Gomezplaza, A., Martinezmena, M., 2003. The role of antecedent soil water content in the runoff response of semiarid catchments: a simulation approach. *J. Hydrol.* 284, 114-130.

Chen, F., Warner, T., Manning, K., 2001. Sensitivity of orographic moist convection to landscape variability: a study of the Buffalo Creek, Colorado, Flash Flood case of 1996. *Journal of Atmos. Sci*. 58, 3204-3223.

Chiang, Y.M., Hsu, K.L., Chang, F.J., Hong, Y., Sorooshian, S., 2007. Merging multiple precipitation sources for flash flood forecasting. *J. Hydrol.* 340, 183-196.

Chow, V.T., 1959. *Open Channel Hydraulics*. New York: McGraw-Hill.

Collier, C.G., 1991. The combined use of weather radar and mesoscale numerical model data for short-period rainfall forecasting. *Hydrological Application of Weather Radar.* E. Horwood: I.D. Cluckie and C.G. Collier Eds.

Collier, C.G., 1996. Weather radar precipitation data and their use in hydrological modeling. *Distributed Hydrological Modeling*. Dordretch: Kluwer Academic Publishers 143-163.

Collier, C.G., 2007. Flash flood forecasting: what are the limits of predictability?.

Q. J. Roy. Meteor. Soc. 133, 3-23.

Collier, C.G., Krzysztofowicz, R., 2000. Quantitative precipitation forecasting (Editorial). *J. Hydrol.* 239(1–4), 1–2.

Collins, D.L., Doesken, N.J., Stanton, W.P., 1991. Colorado floods and droughts. *U.S. Geological Survey Water Supply Paper* 2375, 207–214.

Delrieu, G., Andieu, H., Creutin, J.D., 2000. Quantification of path integrated attenuation of X- and C-band weather radar systems operating in Mediterranean heavy rainfall. *J. Appl. Meteorol.* 39, 840-850.

Dixon, M., Wiener, G., 1993. TITAN. Thunderstorm identification, tracking, analysis and nowcasting – A radar-based methodology. *J. Atmos. Ocean. Tech.* 10, 785-795.

Droegemeier, K. K., Smith, J. D., Businger, S., Doswell, III, C., Doyle, J., Duffy, C., Foufoula-Georgiou, E., Graziano, T., James, L. D., Krajewski, V., LeMone, M., Lettenmaier, D., Mass, C., Pielke, Sr. , R., Ray, P., Rutledge, S., Schaake, J., Zipser, E., 2000. Hydrological aspects of weather prediction and flood warnings: Report of the ninth prospectus development team of the U.S. Weather Research Program. *B. Am. Meteorol. Soc.* 81, 2665-2680.

Duan, Q., Gupta, V.K., Sorooshian, S., 1993. A shuffled complex evolution approach for effective and efficient optimization. *J. Optimiz. Theory Appl.* 76, 501-521.

Fread, D.L., Shedd, R.C., Smith, G.F., Farnsworth, R., Hoffeditz, C.N., Wenzel, L.A., Wiele, S.M., Smith, J.A., Day, G.N., 1995. Modernization in the National Weather Service River and Flood Program. *Weather Forecast.* 10,477-484.

Fulton, R.A., Breidenbach, J.P., Seo, D., Miller, D.A., O'Banon, T., 1998. The WSR-88D rainfall algorithm. *Weather Forecast.* 13, 377-395.

Furey, P.R., Gupta,V.K. 2005. Effects of excess rainfall on the temporal variability of observed peak-discharge power laws. *Adv. Water Resour.* 28, 1240-1253.

Ganguly, A. R., Bras, R.L 2003. Distributed quantitative precipitation forecasting using information from radar and numerical weather prediction models. *J. Hydrometeor.* 4, 1168–1180.

Garrote, L., Bras, R.L., 1995. A distributed model for real-time flood forecasting using digital elevation models. *J. Hydrol.* 167, 279–306.

Germann, U., Berenguer, M., Sempere-Torres, D., Zappa, M., 2009. REAL - Ensemble radar precipitation estimation for hydrology in a mountainous region. *Q. J. Roy. Meteor. Soc.* 135, 445-456.

Gesch, D., Oimoen, M., Greenlee, S., Nelson, C., Steuck, M., Tyler, D., 2002. The national elevation dataset. *Photogramm. Eng. Rem. Sen.* 68, 5-11.

Gochis, D.J., Nesbitt, S., Yu, W., Williams, S.F., 2009. Assessment of quantitative precipitation estimates from space-borne platforms during the 2004 North American Monsoon Experiment. *Atmosfera* 22, 69-98.

Golding, B.W., 2000. Quantitative precipitation forecasting in the UK. *J. Hydrol.* 239, 286-305.

Goodrich, D. C., Schmugge, T. J., Jackson, T. J., Unkrich, C. L., Keefer, T. O., Parry, R., Bach, L. B., Amer, S. A., 1994. Runoff simulation sensitivity to remotely sensed initial soil water content. *Water Resour. Res.* 30(5), 1393–1405.

Gourley, J., Vieux, B.E., 2005. A method for evaluating the accuracy of quantitative precipitation estimates from a hydrologic modeling perspective. *J. Hydrometeorol.* 6, 115-133.

Grayson, R.B., Bloschl, G., Western, A.W., McMahon, T.A., 2002. Advances in the use of observed spatial patterns of catchment hydrologic response. *Adv. Water Resour.* 25, 1313-1334.

Grassotti, C., Hoffman, R.N., Vivoni, E.R., Entekhabi, D., 2003. Multiple timescale intercomparison of two radar products and rain gauge observations over the Arkansas-Red river basin. *Weather Forecast.* 18 (6), 1207-1229.

Gupta, V.K., 2004. Emergence of statistical scaling in floods on channel networks from complex runoff dynamics. *Chaos Soliton Fract.* 19(2), 357-365.

Habib, E., Malakpet, C., Tokay, A., Kucera, P., 2008. Sensitivity of streamflow simulations to temporal variability and estimation of *Z-R* relationships. *J. Hydrol. Eng.* 13 (12), 1177-1186.

Herschy, R.W., 1995. *Streamflow Measurement*, Second Edition, London, UK.

Higgins, R.W., Gochis, D.J., 2007. Synthesis of results from the North American Monsoon Experiment (NAME) Process Study. *J. Climate* 20 (9), 1601-1607.

Homer, C., Huang, C., Yang, L., Wylie, B., Coan, M., 2004. Development of a

2001 National Landcover Database for the United States. *Photogramm. Eng. Rem. Sens.* 70 (7), 829-840.

Hong, Y., Gochis, D.J., Cheng, J., Hsu, K.L., Sorooshian, S., 2007. Evaluation of PERSIANN-CCS rainfall measurement using the NAME Event Rain Gauge Network. *J. Hydrometeor.* 8, 469–482.

Hong, Y., Hsu, K.L., Sorooshian, S., Gao, X., 2004. Precipitation estimation from remotely sensed imagery using an artificial neural network cloud classification system. *J. Appl. Meteor.* 43, 1834–1853.

Horel, J., Splitt, M., Dunn, L., Pechmann, J., White, B., Ciliberti, C., Lazarus, S., Zaff, D., Burks, J., 2002. Mesowest: Cooperative mesonets in the western United States. *Bull. Am. Meteorol. Soc.* 83 (2), 211-225.

Ivanov, V.Y., Vivoni, E.R., Bras, R.L., Entekhabi, D., 2004a.Catchment hydrologic response with a fully-distributed triangulated irregular network model. *Water Resour. Res*. 40(11), W11102, 10.1029/2004WR003218.

Ivanov, V.Y., Vivoni, E.R., Bras, R.L., Entekhabi, D., 2004b. Preserving high-resolution surface and rainfall data in operational-scale basin hydrology: a fully- distributed physically-based approach. *J. Hydrol.* 298, 80-111.

Jarret, R.D., Costa, J.E., 1988. *Evaluation of the flood hydrology in the Colorado Front Range using precipitation, streamflow, and paleoflood data for the Big Thompson River basin.* US Geological Survey, Water Resources Investigations Report 87-4117.

Jarret, R.D., Tomlinson, E., 2000. Regional interdisciplinary paleoflood approach to assess extreme flood potential. *Water Resour. Res.* 36(10), 2957-2984.

Joe, P., Burgess, D., Potts, R., Keenan, T., Stumpf G., Treloar, A. 2004. The S2K Severe weather detection algorithms and their performance. *Weather Forecast.* 19(1), 43-63.

Joss, J., Waldvogel, A., 1970. A method to improve the accuracy of radar-measured amounts of precipitation. *Preprints, 14th Radar Meteorology Conf., Tucson, AZ,* 237-238.

Kang, B., Ramirez, J., 2007. Response of streamflow to weather variability under climate change in the Colorado Rockies. *J. Hydrol. Eng.* 12, 63-72.

Karypis, G., Kumar, V., 1999. Parallel multilevel k-way partitioning scheme for irregular graphs. *Soc. Appl. Math.* 41, 278-300.

Kelleher, K., Droegemeir, K., Levit, J., Sinclar, C., Jahn, D., Hill, S. D., Mueller, L., Qualley, G., Crum, T. D., Smith, S. D., Del Greco, S. A., Lakshmivarahan, S., Miller, L., Ramamurthy, M., Domenico, B., Fulker, D., 2007. PROJECT CRAFT - A real-time delivery system for NEXRAD Level II data via the Internet. *Bull. Am. Meteorol. Soc.* 88 (7), 1045-1057.

Koren, V.I., Finnerty, B.D., Schaake, J.C., Smith, M.B., Seo, D.J., Duan, Q.Y., 1999. Scaledependencies of hydrologic models to spatial variability of precipitation. *J. Hydrol.* 217, 285-302.

Krajewski, W.F., Villarini G., Smith, J.A., 2010. Radar-rainfall uncertainties: where are we after thirty years of efforts?. *B. Am. Meteorol. Soc*. 91(1), 87-94.

Le Lay, M., G.M. Saulnier, 2007. Exploring the signature of climate and landscape spatial variabilities in flash-flood events: Case of the 8-9 September 2002 Cevennes-Vivaris catastrophic event. *Geophys. Res. Lett.* 34, 1-5.

Lazarus, S.M., Ciliberti, C.M., Horel, J.D., Brewster, K.A., 2002. Near-real-time applications of a mesoscale analysis system to complex terrain. *Weather Forecast*. 17 (5), 971-1000.

Lee, G.W., Zawadski, I., 2005. Modeling the variability of drop size distributions in space and time. *J. Appl. Meteorol.* 44, 241-255.

Legates, D.R., McCabe, G.J., 1999. Evaluating the use of "goodness-of-fit" measures in hydrologic and hydroclimatic model validation. *Water Resour. Res.* 35, 233-241.

Li, P.W., Lai, E.S.T., 2004. Short-range quantitative precipitation forecasting in Hong Kong. *J. Hydrol.* 288**,** 189-209.

Lin, C., Vasić, S., Kilambi, A., Turner, B., Zawadzki, I., 2005. Precipitation forecast skill of numerical weather prediction models and radar nowcasts. *Geophys. Res. Lett.* 32, L14801, doi:10.1029/2005GL023451.

Liu, Z., Martina, M.L.V., Todini, E., 2005. Flood forecasting using a fully distributed model: application of the TOPKAPI model to the upper Xixian catchment. *Hydrol. Earth Syst. Sci.* 9,347-364.

Mahmood, T.H. and Vivoni, E.R. 2008. Evaluation of distributed soil moisture simulations through field observations during the North American monsoon in Redondo Creek, New Mexico. *Ecohydrol.* 1(3), 271-287.

Mapiam, P.P., Sriwongsitanon, N., 2009. Effects of rain gauge temporal resolution on the specification of a Z-R relationship. *J. Atmos. Ocean. Tech.*

26, 1302-1314.

Marshall, J.S., Palmer, W.M., 1948. The distribution of raindrops with size. *J. Meteorol*. 5, 165-166.

Mascaro, G., Vivoni, E.R., Deidda, R., 2010a. Implications of ensemble quantitative precipitation forecast errors on distributed streamflow forecasting. *J. Hydrometeorol.* 11, 69-86.

Mascaro, G., Vivoni, E.R., Deidda, R., 2010b. Physical controls on the scale-dependence of ensemble streamflow forecast dispersion. *Nat. Hazards Earth Syst. Sci*. 10, 1605-1615.

McMillan, H., Jackson, B., Clark, M., Kavetski, D., Woods, R., 2011. Rainfall uncertainty in hydrological modelling: An evaluation of multiplicative error models. *J. Hydrol.* 400, 83-94.

Menabde, M., Seed, A., Austin, G., 1996. Multifractal characterization of rain fields with a strong orographic influence. *J. Geophys. Res.* 101, 26405-26414.

Mitchell, K.E., Lohmann, D., Houser, P.R., Wood, E.F., Schaake, J.C., Robock, A., Cosgrove, B.A., Sheffield, J., Duan, Q., Luo, L., Higgins, R.W., Pinker, R.T., Tarpley, J.D., Lettenmaier, D.P., Marshall, C.H., Entin, J.K., Pan, M., Shi, W., Koren, V., Meng, J., Ramsay, B.H., Bailey, A.A., 2004. The multi-institution North American Land Data Assimilation System (NLDAS): Utilizing multiple GCIP products and partners in a continental distributed hydrological modeling system. *J. Geophys. Res.* 109, 1-32.

Moreno, H.A., Vivoni, E.R., Gochis, D., 2012a. Utility of quantitative precipitation estimates for high resolution hydrologic forecasts in mountain watersheds of the Colorado Front Range. *J. Hydrol.* 438-439, 66-83.

Moreno, H.A., Vivoni, E.R., Gochis, D.J., 2012b. Propagation of errors from the reflectivity-rainfall relation into simulated streamflows in mountain watersheds during summer convection. *Hydrol Process.* (submitted).

Moreno, H.A., Vivoni, E.R., Gochis, D.J., 2012c. Spatiotemporal limits to flood forecasting in mountain catchments under summer convection using radar nowcasting and a distributed hydrologic model. *J. Hydrometeorol.*, (in preparation).

Morin, E., Madox, R., Goodrich, D., Sorooshian, S., 2005. Radar Z-R relationship for summer monsoon storms in Arizona. *Weather Forecast.* 20 (4), 672-679.

Moulin, L., Gaume, E., Obled, C., 2009. Uncertainties on mean areal precipitation: assessment and impact on streamflow simulations. *Hydrol. Earth Syst. Sci.* 13 (2), 99-114.

Nykanen, D. K., 2008. Linkages between orographic forcing and the scaling properties of convective rainfall in mountainous regions. *J. Hydrometeorol.* 9, 327-347.

Nikolopoulus, E., Anagnostou, E., Borga, M., Vivoni, E.R., Papadopoulus, A. 2011. Sensitivity of a mountain basin flash flood to initial wetness condition and rainfall variability. *J. Hydrol.* 402, 165-178.

O'Callagan, J.F., Mark, D.M., 1984. The extraction of drainage networks from digital elevation data. Comput. *Vis. Graph. Image Process.* 28, 323-344.

Ogden, F.L., Dawdy, D.R., 2003. Peak discharge scaling in a small hortonian watershed. *J. Hydrol. Eng.,* 123, 386-393.

Pessoa, M. L., Bras, R.L., Williams, E.R., 1993. Use of weather radar for flood forecasting in the Sieve river basin: A sensitivity analysis. *J. Appl. Meteorol.* 32(3), 462-475.

Petersen, W.A., Lawrence, D.C., Rutledge, S., Knievel, J., Johnson, R.H., Nolan J.D., Thomas B. M., Thomas, V.H., Weaver, J.F., 1999. Mesoscale and radar observations of the Fort Collins flash flood of 28 July 1997. *Bull. Am. Meteorol. Soc.* 80, 191-216.

Prat, O. P., Barros, A. P., 2009. Exploring the transient behavior of Z-R relationships: implications for radar rainfall estimation. *J. Appl. Meteorol Clim.* 48(10), 2127-2143.

Rawls, W.J., Brakensiek, D.L., Saxton, K.E., 1982. Estimation of soil water properties. *T. ASABE* 25, 1316-1320.

Reed, S., Koren, V., Smith, M., Zhang, Z., Moreda, F, Seo, D.J., and DMIP Participants, 2004. Overall distributed model intercomparison project results. *J. Hydrol.* 298, 27-60.

Reed S., Schaake, J., Zhang, Z., 2007. A distributed hydrologic model and threshold frequency-based method for flash flood forecasting at ungauged locations. *J. Hydrol.* 337 (3-4), 402-420.

Rinehart, A.J., Vivoni, E.R., Brooks, P.D., 2008. Effects of vegetation, albedo and solar radiation sheltering on the distribution of snow in the Valles Caldera, New Mexico. *Ecohydrology* 1 (3), 253-270.

Rutter, A.J., Morton, A.J., 1977. A predictive model of rainfall interception in forests: Sensitivity of the model to stand parameters and meteorological variables. *J. Appl. Ecol.* 14, 567-588.

Sapiano, M., Arkin, P., 2009. An intercomparison and validation of high-resolution satellite precipitation estimates with 3-hourly gauge data. *J. Hydrometeorol.* 10, 149-166.

Saulnier, G.M., Beven, K., Obled, C., 1997. Including spatially-variable effective soil depths in TOPMODEL. *J. Hydrol.* 202-158-172.

Schröter, K., Llort, X., Velasco-Forero, C., Ostrowski, M., Sempere-Torres, D., 2011. Implications of radar rainfall estimates uncertainty on distributed hydrological model predictions. *Atmos. Res.* 100, 237-425.

Scofield, R., Kuligowski, R., 2003. Status and outlook of the operational satellite precipitation algorithms for extreme-precipitation events. *Weather Forecast.* 18, 1037-1051.

Seo, D., Breidenbach J., Johnson, E., 1999. Real-time estimation of mean field bias in radar rainfall data. *J. Hydrol.* 223, 131-147.

Sharif, H.O., Ogden, F.L., Krajewski, W.F., Xue, M., 2004. Statistical analysis of radar-rainfall error propagation. *J. Hydrometeorol.* 5, 199-212.

Sharif, H.O., Yates, D., Roberts, R., Mueller, C., 2006. The use of an automated nowcasting system to forecast flash floods in an urban watershed. *J. Hydrometeorol.* 7 (1), 190-202.

Shuttleworth, W.J., 1988. Evaporation from Amazonian rainforest. *Proc. Roy. Soc. London* 323, 321-346.

Skaugen, T., Vringstad, T., 2005. A methodology for regional flood frequency estimation based on scaling properties. *Hydrol Process.* 19, 1481-1495.

Smith, M.B., Seo, D.J., Koren, V.I., Reed, S.M., Zhang, Z., Duan, Q., Moreda, F., Cong, S., 2004. The distributed model intercomparison project (DMIP): motivation and experiment design. *J. Hydrol.* 298, 4-26.

Smith, T.M., Arkin, P.A., Bates, J.J., Huffman, G., 2006. Estimating bias of satellite-based precipitation estimates. *J. Hydrometeorol*. 7, 841–856.

Steenburgh, J.W., 2003. One hundred inches in one hundred hours: evolution of a wasatch mountain winter storm cycle. *Weather Forecast.* 18 (6), 1018-1036.

Tarboton, D.G., Bras, R.L., Rodriguez-Iturbe, I., 1991. On the extraction of channel networks from digital elevation data. *Hydrol. Process.* 5 (1), 81-100.

Tobin, K., Bennett, M., 2009. Using SWAT to model streamflow in two river basins with two ground and satellite precipitation data. *J. Am. Water Resour. Assoc.* 45, 253-271.

Todd, D.K., Mays, L.W., 2005. *Groundwater Hydrology, 3rd Edition.* New York: Wiley & Sons.

Turk, F.J., Miller, S.D., 2005. Towards improved characterization of remotely-sensed precipitation regimes with MODIS/AMSR-E blended data techniques. IEEE Trans. *Geosci. Rem. Sens.* 43, 1059-1069.

Van Horne, M.P., Vivoni, E.R., Entekhabi, D., Hoffman, R.N., Grassotti, C. 2006. Evaluating the effects of image filtering in short-term radar rainfall forecasting for hydrological applications. *Meteorol Appl.* 13(3), 289-303.

Verbunt, M., Walser, A., Gurtz, J., Montani, A., Schär, C., 2007. Probabilistic flood forecasting with a limited-area ensemble prediction system: selected case studies. *J. Hydrometeorol.* 8, 897-909.

Vicente, G., Davenport, J., Scofield, R., 2002. The role of orographic and parallax correction on real time high resolution satellite rainfall rate distribution. *Int. J. Remote Sens.* 23, 221-230.

Vicente, G., Scofield, R., Menzel, W., 1998. The operational GOES infrared rainfall estimation technique. *Bull. Am. Meteorol. Soc.* 79, 1883-1898.

Vieux, B.E., Bedient, P.B., 2004. Estimation of rainfall for flood prediction from WSR-88D reflectivity: A case study, 17-18 October 1994. *Weather Forecast.* 13(2), 407-415.

Vieux, B.E, Park, J., Kang, B., 2009. Distributed hydrologic prediction: Sensitivity to accuracy of initial soil moisture conditions and radar rainfall input. *J. Hydrol. Eng.* 9, 288-302.

Vivoni, E.R., Di Benedetto, F., Grimaldi, S., Eltahir, E.A.B., 2008. Hypsometric control on surface and subsurface runoff. *Water Resour. Res.* 44, W12502.

Vivoni, E.R., Entekhabi, D., Bras, R.L., Ivanov, V.Y., 2007a. Controls on runoff generation and scale-dependence in a distributed hydrologic model. *Hydrol. Earth Syst. Sci.* 11, 1683-1701.

Vivoni, E.R., Entekhabi, D., Hoffman, R.N., 2007b. Error propagation of radar rainfall nowcasting fields through a fully-distributed flood forecasting model. *J. App. Meteorol. Clim.* 46, 932-940.

Vivoni, E. R., Entekhabi, D., Bras, R.L., Ivanov, V.Y., Van Horne, M.P., Grassotti, C., Hoffman, R.N., 2006. Extending the predictability of hydrometeorological flood events using radar rainfall nowcasting. *J. Hydrometeorol.* 7, 660-677.

Vivoni, E. R., Ivanov, V.Y., Bras, R.L., Entekhabi, D., 2004. Generation of triangulated irregular networks based on hydrological similarity. *J. Hydrol. Eng.* 9, 288-302.

Vivoni, E.R., Mascaro, G., Mniszewski, S., Fasel, P., Springer, E.P., Ivanov, V.Y., Bras, R.L., 2011. Real-world hydrologic assessment of a fully-distributed hydrological model in a parallel computing environment. *J. Hydrol.* 409, 483-496.

Vivoni, E.R., Tai, K. and Gochis, D.J. 2009. Effects of initial soil moisture on rainfall generation and subsequent hydrologic response during the North American monsoon. *J. Hydrometeorol.* 10(3), 644-664.

Wang, X., Melesse, A., 2006. Effects of STATSGO and SSURGO as inputs on SWAT model's snowmelt simulation. *J. Am. Water Resour. Assoc.* 42(5), 1217-1236.

Wang, X., Xie, H., Sharif, H., Zeitler, J., 2008. Validating NEXRAD MPE and stage III precipitation products for uniform rainfall on the upper Guadalupe River Basin of the Texas Hill Country. *J. Hydrol.* 348, 73-86.

Warner, T. T., Brandes, E. A., Sun, J., Yates, D.N., Mueller, C.K., 2000. Prediction of a flash flood in complex terrain. Part I: A Comparison of rainfall estimates from radar, and very short range rainfall simulations from a dynamic model and an automated algorithmic system. *J. Appl. Meteor.* 39, 797–814.

Wilks, D.S., 2006. *Statistical Methods in Atmospheric Sciences*. Academic Press, 627 pp.

Winchell, M., Gupta, H.V., Sorooshian, S., 1998. On the simulation of infiltration-and saturation-excess runoff using radar-based rainfall estimates: Effects of algorithm uncertainty and pixel aggregation. *Water Resour. Res.* 34, 2655-2670.

Xie, H.J., Zhou, X.B., Vivoni, E.R., Hendrickx, J.M.H., Small, E.E., 2005. GIS-based NEXRAD Stage III precipitation database: automated approaches for

data-processing and visualization. *Comput. Geosci.* 31, 65-76.

Yates, D., Warner, T., Brandes, E.A., Leavesley, G.H., Sun, J., Mueller, C.K., 2001. Evaluation of flash-flood discharge forecasts in complex terrain using precipitation. *J. Hydrol. Eng*. 6, 265-274.

Yates, D., Warner, T., Leavesley, G.H., 2000. Prediction of a flash flood in complex terrain. Part II: A comparison of flood discharge simulations using rainfall input from radar, a dynamic model, and an automated algorithmic system. *J. Appl. Meteor.* 39, 815–825.

Yilmaz, K., Hogue, T., Sorooshian, S., Hsu, K., Gupta, H., Wagener, T., 2005. Hydrological aspects of meteorological verification. *J. Hydrometeorol.* 6, 497-517.

Yoo, C., Kim, K., Choi, J., Ha, E., 2010. Importance of no-rain measurements on the comparison of radar and rain gauge rain rate. *Hydrol. Process.* 24(7), 924-933.

Young, C.B., Bradley, A.A., Krajewski, W.F., Kruger, A., Morrisey, L., 2000. Evaluating NEXRAD multisensor precipitation estimates for operational hydrologic forecasting. *J. Hydrometeorol.* 1, 241-254.

Yucel, I., Kuligowski, R. J., Gochis, D. J., 2011. Evaluating the hydro-estimator satellite rainfall algorithm over a mountainous region. *International Journal of Remote Sensing* 32(22), 7315-7342.

Zangl, G., Aulehnera, D., Wastl, C., Pfeiffera, A., 2008. Small-scale precipitation variability in the Alps: Climatology in comparison with semi-idealized numerical simulations. *Q. J. Roy. Meteor. Soc.* 134, 1865-1880.

Zappa, M., Jaun, S., Germann, U., Walser, A., Fundel, F., 2011. Superposition of three sources of uncertainties in operational flood forecasting chains. *Atmos. Res.* 100, 246-262.

Zehe, E., Becker, R., Bardossy, A., Plate, E., 2005. Uncertainty of simulated catchment runoff response in the presence of threshold processes: Role of initial soil moisture and precipitation. *J. Hydrol.* 315, 183-202.

APPENDIX A

HYDROMETEOROLOGICAL DATASET

This appendix compiles the full sets of hydrometeorological data either observed or forecasted that was used in this doctoral thesis. The Table A.1 briefly describes the types of data and the main characteristics in terms of digital format, coverage and spatiotemporal resolution.

Table A.1 Hydrometeorological dataset.

Type	Folder name	Description
Quantitative Precipitation Estimations	QPE	QPE folder contains information for the 10 QPE products considered in Chapter 2 with the following characteristics: - Temporal coverage: From May 15 to September 30, 2004. Gaps were filled with Level II 4km data. - Spatial resolution: 4 km. Level II-1km that has 1 km resolution. - Temporal resolution: 1h - File format: ASCII
Quantitative Precipitation Forecasts	QPF	QPF ensemble members after running TITAN for the two storm events described in Chapter 4. The following is the description of each folder. - Folders of interest: Clipped_QPF_2004 and Clipped_QPF_2006 - Prototype subfolders: "M.S.S_10_L.T_0.1_D.T_5-1000m_FT_15min_LeadTime_15min". Where M.S.S, L.T. and D.T. are the three parameters in TITAN to produce ensemble members. LeadTime_15min is the lead time used for each simulation, in this example 15 min. Each of the ensemble members contains ASCII matrices from the start to the end of each storm system, with the following characteristics: - Temporal resolution: 15min - Saptial resolution: 1km - Coverage: CFR - Lead times:{15, 30, 45, 60, 75, 90, 120, 150, 180 min} QPE comparative datasets are contained in two folders: - Folders of interest: clipped_QPE_2004 and clipped_QPE_2006. - Spatial resolution: 1km - Temporal resolution: 15min - Coverage: CFR

Streamflow time series	Streamflow	Stream flow time series of discharge stations within the CFR. The acronyms correspond to the following watersheds: Big Thompson River at Estes Park: BTABESCO Fish Creek Near Estes Park: FISHESCO North Fork Big Thompson River at Drake: BTFDRCO Little Thompson River Near Berthoud: LTCANYCO Buckhorn Creek Near Masonville: BUCRMVCO North Saint Vrain Creek Near Allens Park: STALENCO Middle Saint Vrain Creek Paceful Valley: MIDSTECO South Saint Vrain Creek Near Ward: SSVWARCO Middle Boulder Creek at Nederland: BOCMIDCO Coal Creek Near Plainview: COCREPCO Ralston Creek ab. Reservoir near Golden: RALCRKCO - Time resolution: 15 minutes. For NVRAIN and FISH it is1 hour. - Columns correspond to Year, Month, Day, Hour, Min, Stage(ft), Discharge (cfs). - Data commonly start in May of each year. - Years reported are 2003, 2004, 2005, 2006.
Weather time series	Weather	Weather folder contains information for the seven meteorological stations used in this thesis. - Temporal Coverage: Summers 2004 and 2006. - Temporal resolution: 1 hour - Variables or columns: Y, M, D, H, PA, TD, XC, US, TA,IS YEAR, MONTH, DAY, HOUR, ATMOSPHERIC PRESSURE, DEW POINT TEMPERATURE, CLOUD COVER, WIND SPEED, AIR TEMPERATURE, INCOMMING SOLAR RADIATION - Temporal coverage: From June to September 2004 and 2006. - File format: ASCII
Level II data for different Z-R relations	Z-R data	Level II hourly precipitation data as a result of the different Z-R relations for the entire CFR. Each folder contains 3250 matrices with rainfall values. - Temporal coverage: May 15 to September 30, 2004 - Temporal resolution: 1 hour - Spatial resolution: 1 km

APPENDIX B

GIS DATASET

This appendix compiles the main sets of GIS data that was used in this doctoral thesis. The Table B.1 briefly describes the metadata and file format for each geo-spatial layer.

Table B.1 GIS dataset.

Type	Folder name	Description*
Landsat image	Landsat	False color Landsat image of the CFR taken in June 2004 with 30 m resolution.
Landcover data	National_Landcover_2001	Original landcover data from National Landcover Dataset in 2001. Inside this folder, a folder named "Definitive_map" contains the 30m-ASCII with the definitive classes studied in the thesis.
Digital Elevation Model	NED_DEM	Digital Elevation Model from the National Elevation Dataset at 30m resolution for CFR that was used to generate the TINs.
Hydrography	North American Atlas Water	Regional hydrography of the CFR extracted from the North American Atlas Water at high resolution.
Radar stations	Radar location	Shape files with the geographic location of radars within CFR.
Rain Gauges	Rain gauge stations	Locations of daily and hourly rain gauge stations within CFR.
Soil types	Soils	SSURGO and STATSGO databases. Inside this folder, a folder named "Definitive_map" contains the 30m-ASCII with the definitive classes studied in the thesis.
Stream gauges	Streamgauge_stations	Shape files with the location of the eleven stream gauges.
Divides and channel network	Water_divides_UTM13	Shape files with the watershed divides and channel networks at each basin. As in soils and vegetation, UTM13 is the default coordinate system.
Divides and channel network	Watershed_divides_automatic	Shape files with the watershed divides and channel networks at each basin. WSG84 if the coordinates system.

* All data layers geo-referenced to same coordinate system UTM13

APPENDIX C

MODEL SIMULATIONS

This appendix compiles the entire set of simulations and outputs obtained with different QPE and QPF forcing. Additionally tRIBS source code has been added and need to be compiled in specific Linux machine. The Table C.1 briefly describes the type of information inside each folder. The directories are organized so that the tRIBS model can be run from the hard disk with any major changes.

Table C.1 Model simulations.

Type	Folder names	Description
QPE setup	Seasonal_calibration	This folder contains the model setups for runs in Chapters 2 and 3 of thesis. Calibrated soil and input parameters are located in each of the subfolders corresponding to each watershed (BUCK, SVRAIN, FISH or RALS). The traditional directory order including GWinit, Input, Weather, Output, etc., is present in each folder. Metis partitioning files are attached to each folder. Additionally, jobscript files (sh) are included within each subfolder to run each basin in an independent manner in the Saguaro Supercomputer at ASU.
QPF setup	Event_calibration Event_validation	These folders contain the model setups for runs in Chapter 4 of thesis regarding the storm 2004 (event_calibration) and storm 2006 (event_validation). Event calibrated soil and input parameters are located in each of the subfolders corresponding to each watershed. The traditional directory order including GWinit, Input, Weather, Output, etc. is present in each folder. Metis partitioning and restart files are attached to each subdirectory. Additionally, jobscript files (sh) are included within each subfolder to run each basin in an independent manner in the Saguaro Supercomputer at ASU.
QPE Outputs	Outputs_QPE	This folder contains the model outputs when forced with the different types of QPEs at the seasonal scale. Subfolders are organized in a manner that the four study basins contain Input information and a folder called "Output_QPEs" that contains the outputs of each calibrated basin when forced with the QPEs.

QPF Outputs	Outputs_QPF	This folder contains the model outputs when forced with the different QPF and corresponding QPE for the two storm systems in 2004 and 2006. Below is a short description of the folders: - QPE2004 and QPE2006: Contain hydrologic OUTPUTS at each basin when forced with 15-min, 1km Level II data. - QPF2004 and QPF2006: Contain hydrologic OUTPUTS at each basin by forcing the model with the different QPF described in Appendix A. Ensemble results are organized in a similar manner to QPF (e.g. M.S.S_10_L.T_0.1_D.T_5-1000m_FT_15min_LeadTime_15min), where, in this case, LeadTime_15min means the hydrologic simulation was conducted for one member whose lead time is 15min.
tRIBS Code	tRIBS	This folder contains tRIBS source code and compiled versions of tRIBS and ptRIBS. Also METIS and MESHBUILDER utilities have been added in case parallelization of the model domain is needed.

Calibrated soil parameters for each of the simulations are added next. Tables C.2 to C.5 compile the .sdt files at the four seasonally calibrated basins used in Chapters 2 and 3. Tables, C.6 to C.16 compile the soil parameters for the eleven basins as calibrated for Chapter 4.

Table C.2 Calibrated soil parameters for BUCK for summer 2004.

20 12
1 117.8 0.417 0.020 0.694 -72.6 0.007 65 140 0.437 1.93 2595825
2 29.9 0.401 0.035 0.553 -86.9 0.007 65 140 0.436 1.75 2637693
3 7.9569 0.31892 0.041 0.806842 -244.21824 0.033364 223 223 0.453 1.65 2721430
4 30.29011 0.372754 0.027 1.459604 -704.4577 0.025288 25 25 0.461 1.42 2826100
5 6.5 0.486 0.015 0.234 -207.9 0.00650 65 140 0.501 1.26 2805166
6 6.5 0.486 0.015 0.234 -207.9 0.00700 65 140 0.501 1.34 2742364
7 1.0 0.432 0.040 0.177 -325.6 0.00680 50 140 0.472 1.09 2951705
8 1.0 0.390 0.075 0.242 -258.9 0.00700 50 140 0.465 1.13 2909836
9 1.5 0.330 0.068 0.319 -280.8 0.00670 25 125 0.398 1.26 2826100
10 0.6 0.321 0.109 0.223 -291.7 0.00700 50 140 0.430 1.17 2847034
11 0.5 0.423 0.056 0.15 -341.9 0.00700 50 140 0.479 1 3035441
12 0.3 0.385 0.090 0.165 -373 0.00700 50 140 0.475 1 3014507
13 0.35 0.01 0.005 0.165 -1.0 0.006884 227 227 0.015 1.7 3516925
14 3.7 0.385 0.090 0.165 -373 0.00700 65 140 0.475 1 3014507
15 0.35 0.01 0.005 0.165 -1.0 0.006884 227 227 0.015 1.7 3516925
16 7.9569 0.31892 0.041 0.806842 -244.21824 0.033364 223 223 0.453 1.65 2721430
17 7.9569 0.31892 0.041 0.806842 -244.21824 0.033364 223 223 0.453 1.65 2721430
18 7.9569 0.31892 0.041 0.806842 -244.21824 0.033364 223 223 0.453 1.65 2721430
19 0.35 0.01 0.005 0.165 -1.0 0.006884 227 227 0.015 1.7 3516925
20 0.35 0.01 0.005 0.165 -1.0 0.006884 227 227 0.015 1.7 3516925

Table C.3 Calibrated soil parameters for FISH for summer 2004.

20 12
1 117.8 0.417 0.020 0.694 -72.6 0.007 65 140 0.437 1.93 2595825
2 29.9 0.401 0.035 0.553 -86.9 0.007 65 140 0.436 1.75 2637693
3 17.1765 0.3479 0.041 1.4681 -84.3614 0.00222 223 223 0.453 1.65 2721430
4 3.4 0.434 0.027 0.252 -111.5 0.00625 25 125 0.461 1.42 2826100
5 6.5 0.486 0.015 0.234 -207.9 0.00650 65 140 0.501 1.26 2805166
6 6.5 0.486 0.015 0.234 -207.9 0.00700 65 140 0.501 1.34 2742364
7 1.0 0.432 0.040 0.177 -325.6 0.00680 50 140 0.472 1.09 2951705
8 1.0 0.390 0.075 0.242 -258.9 0.00700 50 140 0.465 1.13 2909836
9 1.5 0.330 0.068 0.319 -280.8 0.00670 25 125 0.398 1.26 2826100
10 0.6 0.321 0.109 0.223 -291.7 0.00700 50 140 0.430 1.17 2847034
11 0.5 0.423 0.056 0.15 -341.9 0.00700 50 140 0.479 1 3035441
12 0.3 0.385 0.090 0.165 -373 0.00700 50 140 0.475 1 3014507
13 2.0449 0.0692 0.005 0.0638 -221.8953 0.03063 227 227 0.015 1.7 3516925
14 3.7 0.385 0.090 0.165 -373 0.00700 65 140 0.475 1 3014507
15 2.0449 0.0692 0.005 0.0638 -221.8953 0.03063 227 227 0.015 1.7 3516925
16 17.1765 0.3479 0.041 1.4681 -84.3614 0.00222 223 223 0.453 1.65 2721430
17 17.1765 0.3479 0.041 1.4681 -84.3614 0.00222 223 223 0.453 1.65 2721430
18 17.1765 0.3479 0.041 1.4681 -84.3614 0.00222 223 223 0.453 1.65 2721430
19 2.0449 0.0692 0.005 0.0638 -221.8953 0.03063 227 227 0.015 1.7 3516925
20 2.0449 0.0692 0.005 0.0638 -221.8953 0.03063 227 227 0.015 1.7 3516925

Table C.4 Calibrated soil parameters for RALS for summer 2004.

20 12
1 117.8 0.417 0.020 0.694 -72.6 0.007 65 140 0.437 1.93 2595825
2 29.9 0.401 0.035 0.553 -86.9 0.007 65 140 0.436 1.75 2637693
3 18.6430 0.585587 0.041 1.1940 -324.3684 0.008452 220.9145 220.9145 0.453 1.65 2721430
4 25.7587 0.521075 0.027 1.6689 -385.3706 0.036551 690.9287 690.9287 0.461 1.42 2826100
5 6.5 0.486 0.015 0.234 -207.9 0.00650 65 140 0.501 1.26 2805166
6 6.5 0.486 0.015 0.234 -207.9 0.00700 65 140 0.501 1.34 2742364
7 1.0 0.432 0.040 0.177 -325.6 0.00680 50 140 0.472 1.09 2951705
8 1.0 0.390 0.075 0.242 -258.9 0.00700 50 140 0.465 1.13 2909836
9 1.5 0.330 0.068 0.319 -280.8 0.00670 25 125 0.398 1.26 2826100
10 0.6 0.321 0.109 0.223 -291.7 0.00700 50 140 0.430 1.17 2847034
11 0.5 0.423 0.056 0.15 -341.9 0.00700 50 140 0.479 1 3035441
12 0.3 0.385 0.090 0.165 -373 0.00700 50 140 0.475 1 3014507
13 0.35 0.01 0.005 0.165 -1.0 0.006884 227 227 0.015 1.7 3516925
14 3.7 0.385 0.090 0.165 -373 0.00700 65 140 0.475 1 3014507
15 0.35 0.01 0.005 0.165 -1.0 0.006884 227 227 0.015 1.7 3516925
16 18.6430 0.585587 0.041 1.1940 -324.3684 0.008452 220.9145 220.9145 0.453 1.65 2721430
17 18.6430 0.585587 0.041 1.1940 -324.3684 0.008452 220.9145 220.9145 0.453 1.65 2721430
18 18.6430 0.585587 0.041 1.1940 -324.3684 0.008452 220.9145 220.9145 0.453 1.65 2721430
19 0.35 0.01 0.005 0.165 -1.0 0.006884 227 227 0.015 1.7 3516925
20 0.35 0.01 0.005 0.165 -1.0 0.006884 227 227 0.015 1.7 3516925

Table C.5 Calibrated soil parameters for SVRAIN for summer 2004.

20 12
1 117.8 0.417 0.020 0.694 -72.6 0.007 65 140 0.437 1.93 2595825
2 29.9 0.401 0.035 0.553 -86.9 0.007 65 140 0.436 1.75 2637693
3 8.165027 0.567575 0.041 1.481371 -21.706406 0.000364 223 223 0.453 1.65 2721430
4 22.377413 0.55928 0.027 0.575623 -804.967404 0.000956 25 25 0.461 1.42 2826100
5 6.5 0.486 0.015 0.234 -207.9 0.00650 65 140 0.501 1.26 2805166
6 6.5 0.486 0.015 0.234 -207.9 0.00700 65 140 0.501 1.34 2742364
7 1.0 0.432 0.040 0.177 -325.6 0.00680 50 140 0.472 1.09 2951705
8 1.0 0.390 0.075 0.242 -258.9 0.00700 50 140 0.465 1.13 2909836
9 1.5 0.330 0.068 0.319 -280.8 0.00670 25 125 0.398 1.26 2826100
10 0.6 0.321 0.109 0.223 -291.7 0.00700 50 140 0.430 1.17 2847034
11 0.5 0.423 0.056 0.15 -341.9 0.00700 50 140 0.479 1 3035441
12 0.3 0.385 0.090 0.165 -373 0.00700 50 140 0.475 1 3014507
13 0.35 0.01 0.005 0.165 -1.0 0.006884 227 227 0.015 1.7 3516925
14 3.7 0.385 0.090 0.165 -373 0.00700 65 140 0.475 1 3014507
15 0.35 0.01 0.005 0.165 -1.0 0.006884 227 227 0.015 1.7 3516925
16 8.165027 0.567575 0.041 1.481371 -21.706406 0.000364 223 223 0.453 1.65 2721430
17 8.165027 0.567575 0.041 1.481371 -21.706406 0.000364 223 223 0.453 1.65 2721430
18 8.165027 0.567575 0.041 1.481371 -21.706406 0.000364 223 223 0.453 1.65 2721430
19 0.35 0.01 0.005 0.165 -1.0 0.006884 227 227 0.015 1.7 3516925
20 0.35 0.01 0.005 0.165 -1.0 0.006884 227 227 0.015 1.7 3516925

Table C.6 Calibrated soil parameters for BTHOM for Storm 2004.

20 12
1 117.8 0.417 0.020 0.694 -72.6 0.007 65 140 0.437 1.93 2595825
2 29.9 0.401 0.035 0.553 -86.9 0.007 65 140 0.436 1.75 2637693
3 30.688503 0.584432 0.041 1.185196 -187.174416 0.00542 234.629 234.629 0.453 1.65 2721430
4 3.4 0.434 0.027 0.252 -111.5 0.00625 25 125 0.461 1.42 2826100
5 6.5 0.486 0.015 0.234 -207.9 0.00650 65 140 0.501 1.26 2805166
6 6.5 0.486 0.015 0.234 -207.9 0.00700 65 140 0.501 1.34 2742364
7 1.0 0.432 0.040 0.177 -325.6 0.00680 50 140 0.472 1.09 2951705
8 1.0 0.390 0.075 0.242 -258.9 0.00700 50 140 0.465 1.13 2909836
9 1.5 0.330 0.068 0.319 -280.8 0.00670 25 125 0.398 1.26 2826100
10 0.6 0.321 0.109 0.223 -291.7 0.00700 50 140 0.430 1.17 2847034
11 0.5 0.423 0.056 0.15 -341.9 0.00700 50 140 0.479 1 3035441
12 0.3 0.385 0.090 0.165 -373 0.00700 50 140 0.475 1 3014507
13 3.181246 0.02284 0.005 0.190892 -209.354548 0.00678 1.001168 1.001168 0.015 1.7 3516925
14 3.7 0.385 0.090 0.165 -373 0.00700 65 140 0.475 1 3014507
15 3.181246 0.02284 0.005 0.190892 -209.354548 0.00678 1.001168 1.001168 0.015 1.7 3516925
16 30.688503 0.584432 0.041 1.18519 -187.174416 0.00542 234.629 234.629 0.453 1.65 2721430
17 30.688503 0.584432 0.041 1.18519 -187.174416 0.00542 234.629 234.629 0.453 1.65 2721430
18 30.688503 0.584432 0.041 1.185196 -187.17441 0.00542 234.629 234.629 0.453 1.65 2721430
19 3.181246 0.02284 0.005 0.190892 -209.354548 0.00678 1.001168 1.001168 0.015 1.7 3516925
20 3.181246 0.02284 0.005 0.190892 -209.354548 0.00678 1.001168 1.001168 0.015 1.7 3516925

Table C.7 Calibrated soil parameters for BUCK for Storm 2004.

20 12
1 117.8 0.417 0.020 0.694 -72.6 0.007 65 140 0.437 1.93 2595825
2 29.9 0.401 0.035 0.553 -86.9 0.007 65 140 0.436 1.75 2637693
3 7.9569 0.31892 0.041 0.806842 -244.21824 0.033364 223 223 0.453 1.65 2721430
4 30.29011 0.372754 0.027 1.459604 -704.4577 0.025288 25 25 0.461 1.42 2826100
5 6.5 0.486 0.015 0.234 -207.9 0.00650 65 140 0.501 1.26 2805166
6 6.5 0.486 0.015 0.234 -207.9 0.00700 65 140 0.501 1.34 2742364
7 1.0 0.432 0.040 0.177 -325.6 0.00680 50 140 0.472 1.09 2951705
8 1.0 0.390 0.075 0.242 -258.9 0.00700 50 140 0.465 1.13 2909836
9 1.5 0.330 0.068 0.319 -280.8 0.00670 25 125 0.398 1.26 2826100
10 0.6 0.321 0.109 0.223 -291.7 0.00700 50 140 0.430 1.17 2847034
11 0.5 0.423 0.056 0.15 -341.9 0.00700 50 140 0.479 1 3035441
12 0.3 0.385 0.090 0.165 -373 0.00700 50 140 0.475 1 3014507
13 0.35 0.01 0.005 0.165 -1.0 0.006884 227 227 0.015 1.7 3516925
14 3.7 0.385 0.090 0.165 -373 0.00700 65 140 0.475 1 3014507
15 0.35 0.01 0.005 0.165 -1.0 0.006884 227 227 0.015 1.7 3516925
16 7.9569 0.31892 0.041 0.806842 -244.21824 0.033364 223 223 0.453 1.65 2721430
17 7.9569 0.31892 0.041 0.806842 -244.21824 0.033364 223 223 0.453 1.65 2721430
18 7.9569 0.31892 0.041 0.806842 -244.21824 0.033364 223 223 0.453 1.65 2721430
19 0.35 0.01 0.005 0.165 -1.0 0.006884 227 227 0.015 1.7 3516925
20 0.35 0.01 0.005 0.165 -1.0 0.006884 227 227 0.015 1.7 3516925

Table C.8 Calibrated soil parameters for COAL for Storm 2004.

20 12
1 117.8 0.417 0.020 0.694 -72.6 0.007 65 140 0.437 1.93 2595825
2 84.295979 0.362755 0.035 0.6143 -160.969 0.013177 791.185221 791.1852 0.436 1.75 2637693
3 22.275336 0.380271 0.041 1.65553 -21.188365 0.02350 691.2306 691.2306 0.453 1.65 2721430
4 3.4 0.434 0.027 0.252 -111.5 0.00625 25 125 0.461 1.42 2826100
5 6.5 0.486 0.015 0.234 -207.9 0.00650 65 140 0.501 1.26 2805166
6 6.5 0.486 0.015 0.234 -207.9 0.00700 65 140 0.501 1.34 2742364
7 1.0 0.432 0.040 0.177 -325.6 0.00680 50 140 0.472 1.09 2951705
8 1.0 0.390 0.075 0.242 -258.9 0.00700 50 140 0.465 1.13 2909836
9 1.5 0.330 0.068 0.319 -280.8 0.00670 25 125 0.398 1.26 2826100
10 0.6 0.321 0.109 0.223 -291.7 0.00700 50 140 0.430 1.17 2847034
11 0.5 0.423 0.056 0.15 -341.9 0.00700 50 140 0.479 1 3035441
12 0.3 0.385 0.090 0.165 -373 0.00700 50 140 0.475 1 3014507
13 0.35 0.01 0.005 0.165 -1.0 0.006884 227 227 0.015 1.7 3516925
14 3.7 0.385 0.090 0.165 -373 0.00700 65 140 0.475 1 3014507
15 0.35 0.01 0.005 0.165 -1.0 0.006884 227 227 0.015 1.7 3516925
16 22.275336 0.380271 0.041 1.65553 -21.1883 0.0235 691.2306 691.2306 0.453 1.65 2721430
17 22.275336 0.380271 0.041 1.65553 -21.1883 0.0235 691.2306 691.2306 0.453 1.65 2721430
18 22.275336 0.380271 0.041 1.65553 -21.1883 0.0235 691.230653 691.2306 0.453 1.65 2721430
19 0.35 0.01 0.005 0.165 -1.0 0.006884 227 227 0.015 1.7 3516925
20 0.35 0.01 0.005 0.165 -1.0 0.006884 227 227 0.015 1.7 3516925

Table C.9 Calibrated soil parameters for FISH for Storm 2004.

20 12
1 117.8 0.417 0.020 0.694 -72.6 0.007 65 140 0.437 1.93 2595825
2 29.9 0.401 0.035 0.553 -86.9 0.007 65 140 0.436 1.75 2637693
3 0.411234 0.605368 0.041 1.590181 -92.009039 0.009268 649.071695 649.071695 0.453 1.65 2721430
4 3.4 0.434 0.027 0.252 -111.5 0.00625 25 125 0.461 1.42 2826100
5 6.5 0.486 0.015 0.234 -207.9 0.00650 65 140 0.501 1.26 2805166
6 6.5 0.486 0.015 0.234 -207.9 0.00700 65 140 0.501 1.34 2742364
7 1.0 0.432 0.040 0.177 -325.6 0.00680 50 140 0.472 1.09 2951705
8 1.0 0.390 0.075 0.242 -258.9 0.00700 50 140 0.465 1.13 2909836
9 1.5 0.330 0.068 0.319 -280.8 0.00670 25 125 0.398 1.26 2826100
10 0.6 0.321 0.109 0.223 -291.7 0.00700 50 140 0.430 1.17 2847034
11 0.5 0.423 0.056 0.15 -341.9 0.00700 50 140 0.479 1 3035441
12 0.3 0.385 0.090 0.165 -373 0.00700 50 140 0.475 1 3014507
13 3.318567 0.054697 0.005 0.109262 -489.463342 0.006586 1.551745 1.5517 0.015 1.7 3516925
14 3.7 0.385 0.090 0.165 -373 0.00700 65 140 0.475 1 3014507
15 3.318567 0.054697 0.005 0.109262 -489.463342 0.006586 1.551745 1.5517 0.015 1.7 3516925
16 0.411234 0.605368 0.041 1.590181 -92.009039 0.0092 649.0716 649.0716 0.453 1.65 2721430
17 0.411234 0.605368 0.041 1.590181 -92.009039 0.0092 649.0716 649.0716 0.453 1.65 2721430
18 0.411234 0.605368 0.041 1.590181 -92.009039 0.0092 649.0716 649.0716 0.453 1.65 2721430
19 3.318567 0.054697 0.005 0.109262 -489.463342 0.0065 1.551745 1.551745 0.015 1.7 3516925
20 3.318567 0.054697 0.005 0.109262 -489.463342 0.0065 1.551745 1.551745 0.015 1.7 3516925

Table C.10 Calibrated soil parameters for LTHOM for Storm 2004.

20 12
1 117.8 0.417 0.020 0.694 -72.6 0.007 65 140 0.437 1.93 2595825
2 29.9 0.401 0.035 0.553 -86.9 0.007 65 140 0.436 1.75 2637693
3 4.779431 0.571403 0.041 1.42123 -172.458864 0.042258 683.006 683.006 0.453 1.65 2721430
4 7.164652 0.371416 0.027 0.292137 -838.8864 0.001048 110.3839 110.3839 0.461 1.42 2826100
5 6.5 0.486 0.015 0.234 -207.9 0.00650 65 140 0.501 1.26 2805166
6 6.5 0.486 0.015 0.234 -207.9 0.00700 65 140 0.501 1.34 2742364
7 1.0 0.432 0.040 0.177 -325.6 0.00680 50 140 0.472 1.09 2951705
8 1.0 0.390 0.075 0.242 -258.9 0.00700 50 140 0.465 1.13 2909836
9 1.5 0.330 0.068 0.319 -280.8 0.00670 25 125 0.398 1.26 2826100
10 0.6 0.321 0.109 0.223 -291.7 0.00700 50 140 0.430 1.17 2847034
11 0.5 0.423 0.056 0.15 -341.9 0.00700 50 140 0.479 1 3035441
12 0.3 0.385 0.090 0.165 -373 0.00700 50 140 0.475 1 3014507
13 0.35 0.01 0.005 0.165 -1.0 0.006884 227 227 0.015 1.7 3516925
14 3.7 0.385 0.090 0.165 -373 0.00700 65 140 0.475 1 3014507
15 0.35 0.01 0.005 0.165 -1.0 0.006884 227 227 0.015 1.7 3516925
16 4.779431 0.571403 0.041 1.42123 -172.458864 0.042258 683.006 683.006 0.453 1.65 2721430
17 4.779431 0.571403 0.041 1.42123 -172.458864 0.042258 683.006 683.006 0.453 1.65 2721430
18 4.779431 0.571403 0.041 1.42123 -172.458864 0.042258 683.006 683.006 0.453 1.65 2721430
19 0.35 0.01 0.005 0.165 -1.0 0.006884 227 227 0.015 1.7 3516925
20 0.35 0.01 0.005 0.165 -1.0 0.006884 227 227 0.015 1.7 3516925

Table C.11 Calibrated soil parameters for MBOUL for Storm 2004.

20 12
1 117.8 0.417 0.020 0.694 -72.6 0.007 65 140 0.437 1.93 2595825
2 29.9 0.401 0.035 0.553 -86.9 0.007 65 140 0.436 1.75 2637693
3 35.508438 0.415959 0.041 1.195471 -75.355071 0.0406 394.1260 394.1260 0.453 1.65 2721430
4 6.490654 0.343446 0.027 1.186388 -20.813372 0.00543 647.2150 647.2150 0.461 1.42 2826100
5 6.5 0.486 0.015 0.234 -207.9 0.00650 65 140 0.501 1.26 2805166
6 6.5 0.486 0.015 0.234 -207.9 0.00700 65 140 0.501 1.34 2742364
7 1.0 0.432 0.040 0.177 -325.6 0.00680 50 140 0.472 1.09 2951705
8 1.0 0.390 0.075 0.242 -258.9 0.00700 50 140 0.465 1.13 2909836
9 1.5 0.330 0.068 0.319 -280.8 0.00670 25 125 0.398 1.26 2826100
10 0.6 0.321 0.109 0.223 -291.7 0.00700 50 140 0.430 1.17 2847034
11 0.5 0.423 0.056 0.15 -341.9 0.00700 50 140 0.479 1 3035441
12 0.3 0.385 0.090 0.165 -373 0.00700 50 140 0.475 1 3014507
13 0.35 0.01 0.005 0.165 -1.0 0.006884 227 227 0.015 1.7 3516925
14 3.7 0.385 0.090 0.165 -373 0.00700 65 140 0.475 1 3014507
15 0.35 0.01 0.005 0.165 -1.0 0.006884 227 227 0.015 1.7 3516925
16 35.508438 0.415959 0.041 1.195471 -75.355071 0.04068 394.126 394.126 0.453 1.65 2721430
17 35.508438 0.415959 0.041 1.195471 -75.355071 0.04068 394.126 394.126 0.453 1.65 2721430
18 35.508438 0.415959 0.041 1.195471 -75.355071 0.04068 394.126 394.126 0.453 1.65 2721430
19 0.35 0.01 0.005 0.165 -1.0 0.006884 227 227 0.015 1.7 3516925
20 0.35 0.01 0.005 0.165 -1.0 0.006884 227 227 0.015 1.7 3516925

Table C.12 Calibrated soil parameters for MVRAIN for Storm 2004.

20 12
1 117.8 0.417 0.020 0.694 -72.6 0.007 65 140 0.437 1.93 2595825
2 29.9 0.401 0.035 0.553 -86.9 0.007 65 140 0.436 1.75 2637693
3 31.580143 0.537309 0.041 0.811409 -342.805928 0.01652 275.271 275.271 0.453 1.65 2721430
4 13.086015 0.578902 0.027 1.008146 -179.578379 0.00698 752.136 752.136 0.461 1.42 2826100
5 6.5 0.486 0.015 0.234 -207.9 0.00650 65 140 0.501 1.26 2805166
6 6.5 0.486 0.015 0.234 -207.9 0.00700 65 140 0.501 1.34 2742364
7 1.0 0.432 0.040 0.177 -325.6 0.00680 50 140 0.472 1.09 2951705
8 1.0 0.390 0.075 0.242 -258.9 0.00700 50 140 0.465 1.13 2909836
9 1.5 0.330 0.068 0.319 -280.8 0.00670 25 125 0.398 1.26 2826100
10 0.6 0.321 0.109 0.223 -291.7 0.00700 50 140 0.430 1.17 2847034
11 0.5 0.423 0.056 0.15 -341.9 0.00700 50 140 0.479 1 3035441
12 0.3 0.385 0.090 0.165 -373 0.00700 50 140 0.475 1 3014507
13 0.35 0.01 0.005 0.165 -1.0 0.006884 227 227 0.015 1.7 3516925
14 3.7 0.385 0.090 0.165 -373 0.00700 65 140 0.475 1 3014507
15 0.35 0.01 0.005 0.165 -1.0 0.006884 227 227 0.015 1.7 3516925
16 31.580143 0.537309 0.041 0.811409 -342.8059 0.016525 275.271 275.271 0.453 1.65 2721430
17 31.580143 0.537309 0.041 0.811409 -342.8059 0.016525 275.271 275.271 0.453 1.65 2721430
18 31.580143 0.537309 0.041 0.811409 -342.8059 0.016525 275.271 275.271 0.453 1.65 2721430
19 0.35 0.01 0.005 0.165 -1.0 0.006884 227 227 0.015 1.7 3516925
20 0.35 0.01 0.005 0.165 -1.0 0.006884 227 227 0.015 1.7 3516925

Table C.13 Calibrated soil parameters for NFORK for Storm 2004.

20 12
1 117.8 0.417 0.020 0.694 -72.6 0.007 65 140 0.437 1.93 2595825
2 29.9 0.401 0.035 0.553 -86.9 0.007 65 140 0.436 1.75 2637693
3 35.829778 0.364747 0.041 1.380734 -27.033417 0.013087 274.661 274.661 0.453 1.65 2721430
4 3.4 0.434 0.027 0.252 -111.5 0.00625 25 125 0.461 1.42 2826100
5 6.5 0.486 0.015 0.234 -207.9 0.00650 65 140 0.501 1.26 2805166
6 6.5 0.486 0.015 0.234 -207.9 0.00700 65 140 0.501 1.34 2742364
7 1.0 0.432 0.040 0.177 -325.6 0.00680 50 140 0.472 1.09 2951705
8 1.0 0.390 0.075 0.242 -258.9 0.00700 50 140 0.465 1.13 2909836
9 1.5 0.330 0.068 0.319 -280.8 0.00670 25 125 0.398 1.26 2826100
10 0.6 0.321 0.109 0.223 -291.7 0.00700 50 140 0.430 1.17 2847034
11 0.5 0.423 0.056 0.15 -341.9 0.00700 50 140 0.479 1 3035441
12 0.3 0.385 0.090 0.165 -373 0.00700 50 140 0.475 1 3014507
13 1.275242 0.067312 0.005 0.248532 -580.697481 0.048326 1.5495 1.5495 0.015 1.7 3516925
14 3.7 0.385 0.090 0.165 -373 0.00700 65 140 0.475 1 3014507
15 1.275242 0.067312 0.005 0.248532 -580.697481 0.048326 1.5495 1.5495 0.015 1.7 3516925
16 35.829778 0.364747 0.041 1.380734 -27.033417 0.01308 274.661 274.661 0.453 1.65 2721430
17 35.829778 0.364747 0.041 1.380734 -27.033417 0.01308 274.661 274.661 0.453 1.65 2721430
18 35.829778 0.364747 0.041 1.380734 -27.033417 0.013087 274.66 274.66 0.453 1.65 2721430
19 1.275242 0.067312 0.005 0.248532 -580.697481 0.048326 1.5495 1.5495 0.015 1.7 3516925
20 1.275242 0.067312 0.005 0.248532 -580.697481 0.048326 1.549 1.549 0.015 1.7 3516925

Table C.14 Calibrated soil parameters for NVRAIN for Storm 2004.

20 12
1 117.8 0.417 0.020 0.694 -72.6 0.007 65 140 0.437 1.93 2595825
2 29.9 0.401 0.035 0.553 -86.9 0.007 65 140 0.436 1.75 2637693
3 11.146845 0.41770 0.041 0.5319 -29.68379 0.00877 887.97120 887.97120 0.453 1.65 2721430
4 3.4 0.434 0.027 0.252 -111.5 0.00625 25 125 0.461 1.42 2826100
5 6.5 0.486 0.015 0.234 -207.9 0.00650 65 140 0.501 1.26 2805166
6 6.5 0.486 0.015 0.234 -207.9 0.00700 65 140 0.501 1.34 2742364
7 1.0 0.432 0.040 0.177 -325.6 0.00680 50 140 0.472 1.09 2951705
8 1.0 0.390 0.075 0.242 -258.9 0.00700 50 140 0.465 1.13 2909836
9 1.5 0.330 0.068 0.319 -280.8 0.00670 25 125 0.398 1.26 2826100
10 0.6 0.321 0.109 0.223 -291.7 0.00700 50 140 0.430 1.17 2847034
11 0.5 0.423 0.056 0.15 -341.9 0.00700 50 140 0.479 1 3035441
12 0.3 0.385 0.090 0.165 -373 0.00700 50 140 0.475 1 3014507
13 0.687778 0.023478 0.005 0.287777 -70.865252 0.01066 1.870805 1.870805 0.015 1.7 3516925
14 3.7 0.385 0.090 0.165 -373 0.00700 65 140 0.475 1 3014507
15 0.687778 0.023478 0.005 0.287777 -70.865252 0.01066 1.870805 1.870805 0.015 1.7 3516925
16 11.146845 0.417708 0.041 0.53139 -29.683794 0.008776 887.971 887.971 0.453 1.65 2721430
17 11.146845 0.417708 0.041 0.53139 -29.683794 0.008776 887.971 887.971 0.453 1.65 2721430
18 11.146845 0.417708 0.041 0.53139 -29.683794 0.008776 887.971 887.971 0.453 1.65 2721430
19 0.687778 0.023478 0.005 0.287777 -70.865252 0.01066 1.870805 1.870805 0.015 1.7 3516925
20 0.687778 0.023478 0.005 0.287777 -70.865252 0.01066 1.870805 1.870805 0.015 1.7 3516925

Table C.15 Calibrated soil parameters for RALS for Storm 2004.

20 12
1 117.8 0.417 0.020 0.694 -72.6 0.007 65 140 0.437 1.93 2595825
2 29.9 0.401 0.035 0.553 -86.9 0.007 65 140 0.436 1.75 2637693
3 24.418749 0.570053 0.041 1.732439 -387.27021 0.0237 191.6214 191.6214 0.453 1.65 2721430
4 24.219558 0.398956 0.027 0.824442 -680.255162 0.0032 80.9402 80.9402 0.461 1.42 2826100
5 6.5 0.486 0.015 0.234 -207.9 0.00650 65 140 0.501 1.26 2805166
6 6.5 0.486 0.015 0.234 -207.9 0.00700 65 140 0.501 1.34 2742364
7 1.0 0.432 0.040 0.177 -325.6 0.00680 50 140 0.472 1.09 2951705
8 1.0 0.390 0.075 0.242 -258.9 0.00700 50 140 0.465 1.13 2909836
9 1.5 0.330 0.068 0.319 -280.8 0.00670 25 125 0.398 1.26 2826100
10 0.6 0.321 0.109 0.223 -291.7 0.00700 50 140 0.430 1.17 2847034
11 0.5 0.423 0.056 0.15 -341.9 0.00700 50 140 0.479 1 3035441
12 0.3 0.385 0.090 0.165 -373 0.00700 50 140 0.475 1 3014507
13 0.35 0.01 0.005 0.165 -1.0 0.006884 227 227 0.015 1.7 3516925
14 3.7 0.385 0.090 0.165 -373 0.00700 65 140 0.475 1 3014507
15 0.35 0.01 0.005 0.165 -1.0 0.006884 227 227 0.015 1.7 3516925
16 24.418749 0.570053 0.041 1.732439 -387.27021 0.02379 191.621 191.621 0.453 1.65 2721430
17 24.418749 0.570053 0.041 1.732439 -387.27021 0.02379 191.621 191.621 0.453 1.65 2721430
18 24.418749 0.570053 0.041 1.732439 -387.270219 0.0237 191.621 191.621 0.453 1.65 2721430
19 0.35 0.01 0.005 0.165 -1.0 0.006884 227 227 0.015 1.7 3516925
20 0.35 0.01 0.005 0.165 -1.0 0.006884 227 227 0.015 1.7 3516925

Table C.16 Calibrated soil parameters for SVRAIN for Storm 2004.

20 12
1 117.8 0.417 0.020 0.694 -72.6 0.007 65 140 0.437 1.93 2595825
2 29.9 0.401 0.035 0.553 -86.9 0.007 65 140 0.436 1.75 2637693
3 10.553752 0.340788 0.041 1.622464 -343.198011 0.00168 743.762 743.762 0.453 1.65 2721430
4 20.253409 0.37092 0.027 0.099609 -444.638144 0.0103 122.641 122.641 0.461 1.42 2826100
5 6.5 0.486 0.015 0.234 -207.9 0.00650 65 140 0.501 1.26 2805166
6 6.5 0.486 0.015 0.234 -207.9 0.00700 65 140 0.501 1.34 2742364
7 1.0 0.432 0.040 0.177 -325.6 0.00680 50 140 0.472 1.09 2951705
8 1.0 0.390 0.075 0.242 -258.9 0.00700 50 140 0.465 1.13 2909836
9 1.5 0.330 0.068 0.319 -280.8 0.00670 25 125 0.398 1.26 2826100
10 0.6 0.321 0.109 0.223 -291.7 0.00700 50 140 0.430 1.17 2847034
11 0.5 0.423 0.056 0.15 -341.9 0.00700 50 140 0.479 1 3035441
12 0.3 0.385 0.090 0.165 -373 0.00700 50 140 0.475 1 3014507
13 0.35 0.01 0.005 0.165 -1.0 0.006884 227 227 0.015 1.7 3516925
14 3.7 0.385 0.090 0.165 -373 0.00700 65 140 0.475 1 3014507
15 0.35 0.01 0.005 0.165 -1.0 0.006884 227 227 0.015 1.7 3516925
16 10.553752 0.340788 0.041 1.622464 -343.1980 0.001698 743.762 743.762 0.453 1.65 2721430
17 10.553752 0.340788 0.041 1.622464 -343.198011 0.0016 743.762 743.762 0.453 1.65 2721430
18 10.553752 0.340788 0.041 1.622464 -343.198011 0.0016 743.762 743.762 0.453 1.65 2721430
19 0.35 0.01 0.005 0.165 -1.0 0.006884 227 227 0.015 1.7 3516925
20 0.35 0.01 0.005 0.165 -1.0 0.006884 227 227 0.015 1.7 3516925

APPENDIX D

SOFTWARE DEVELOPMENT

This appendix compiles major software development during this thesis. Scripts and programs were all constructed in R (www.r-project.org) a free environment for statistical computing and graphics. The Table D.1 briefly describes scripts functionality. Additional help may be found at the first lines of each script file.

Table D.1 Software development.

Type	Folder names	Description
VisualtRIBS V1.3	Visual_tRIBS	Visual tRIBS V1.3 and Watershed Processing. Computational tool for DEM processing and watershed-channel network extraction. It is also useful for visualizing and exporting multiple serial and parallel outputs of tRIBS (triangulated Real-time Integrated Basin Simulator) including time series and spatial outputs of multiple variables, friendly programmed in R. You have to install R (free programming language) in your O.S. (LINUX, MAC or Windows), execute it by typing R on the terminal and install the following packages, using install.packages("name_of_the package"):playwith, sp, akima, maptools, fields, plotrix. Some users had to update their R libraries by typing "update.packages(checkBuilt=TRUE)" within the R console.
SCE optimized calibration	SCE_tRIBS*	This folder contains two subfolders organized by type of calibration: - Event_calibration: That contains the scripts that were used to calibrate the eleven watersheds during the storm period in 2004 using the Shuffle Complex Evolution. - Seasonal_calibration: Than contains the scripts and results after calibrating the four watersheds during the summer 2004, using the Shuffle Complex Evolution. Within each basin folder several R-scripts and subroutines to run the SCE in a fail-safe mode can be found. Some output examples are included in each folder, so that the user gets familiarized with the type of outputs expected from these runs. The scripts are able to run the calibration from a local computer sending jobs to a supercomputer using X number of processors and store the "best" behavioral parameterizations in a local folder called "Behavioral".

Additional coding	Codes_to_run_tRIBS_in_cluster	Four R-scripts that run tRIBS continuously in a parallel fashion at the Saguaro Supercomputer by using different forcing and storing outputs in an external folder (maybe Saguaro itself). This is convenient to run when testing different Z-R relations, QPE products or ensemble QPFs.

* The actual code is printed below.

SCE MAIN CODE

The following is an example of SCE coding for the case of BTHOM for the event calibration. This code can be modified at the Input section to work in different basins.

```
# This script runs the SCE algorithm from the DESKTOP which runs ptRIBS in the cluster by using "qsub
fish_parallel_part.sh".  CAVEATS:
# 1. Need to connect the cluster folder as a disk in your computer called "cluster" using sshfs. See:
http://embraceubuntu.com/2005/10/28/how-to-mount-a-remote-ssh-filesystem-using-sshfs/
# 2. Need to generate automatic password for ssh through ssh key authentication: keygen, etc:
http://www.youtube.com/watch?v=R65HTJeObkI (SSH logins without passwords)
# 3. This script needs to be saved on a desktop local folder: /media/D/SourceCodes/SCE_tRIBS/SCE
# 4. Do not forget to modify the "fish.par.part_base.in" file for calling the corresponding Metis partition
base_flow_#nodes.reach" correspondign to the number of processors, as well as the absolute paths for the output, weather,
rain...etc folders. This base file has spaces necesarries to modify the routing pars. Need to change the name of the iterative
file (e.g svrain_par_part_iterative.in) but no need to modify it inside. It only serves as a writable file.
# 5. The sdt file must contain exaclty 20 (or more) complete rows.  No blank lines or with spaces are allowed at the end of
the file.
# 6. Review the job script (.sh file) to check the number of processors that must correspond to the same as the variable
called "processors" here and the number of hours for parallel computation. This  .sh file needs to be inside the path "ruta".
Aso check the executable path and .in file that is called. Make sure you change the jobname (e.g "Fish_cal").
# 7. The outputs are written in the "ruta1" folder.
# 8. You can run this script by typing on a terminal: R CMD BATCH
tRIBS_SCE_parallel_optimize_soils_from_Desktop_to_Cluster.R, or simply by openning R and typing: source(
#   "/media/D/Sourc.....")
# 9. If this script fails  or there is an electric outage please use the re-start system
# 10. Remember to create a folder called GWinit where all tge GW init cases are saved. For instance the case :
GW_1056_fish, GW_1450_fish, etc. The first case is the wettest


## Running tRIBS #####
rm(list=ls(all=TRUE))   # INITIAL RUN..
require(audio)
options(scipen = 6) # avoid using 1e-x  notation

#***********************************INPUT
************************************************************
## Interpreting simulations  ######################################################################
init<<-1   #Inital analysis hour for plotting and error estimation. This is useful when we have spin up time. Usually it is =1
or 721
d<<-200    #2190 duration of the simulation in hours. TIme from the *.in file.. 2910 including june
year<<-2004 # Starting year for plotting and error calculation
month<<-8  # STARTING MONTH for plotting and error calculation
day<<-14      # STARTING DAY for plotting and error calculation
hour<<-6    # STARTING HOUR for plotting and error calculation
```

```
minu<<-0
observed_PATH<<-"/media/D/Hernan/Research/Moreno_PhD_Thesis/Additional_Information_CFR/Stream
gaging/BigThompson/15 min/5_15min_Stage_Disch/" # path to the observed discharges
obs_name<<-"BTABESCO_MJJAS_2004_H-D_FILLED.txt"   #  observed. It may start at any month and time. It has
stage and discharge
Qobs_int<<-0.25   # original time resolution of observed streamflowsn named in obs_name
mean_hourly<<-1   # 0 for not averaging hourly simulated and observed streamflows, 1 does it.
Qinterv<<-0.25    # in fractions of 1-hour (e.g 0.25 is 15 minutes).. it is the desired interval for calculating error metrics. it
still works even if mean_hourly=0.. taking instantaneous data
cluster_simulation_folder<<-"/home/hamoreno/Event_calibration/Bthom/"
parallel_jobscript<<-"bthom_parallel_part.sh"

## SCE   ##
ruta<<-"/media/cluster/Event_calibration/Bthom/"   # simulation folder name
base_name<<-"bthom"                          #base name
infile<<-"bthom_par_part_base.in"                          #.in file for the parallel run
iterative_in<-paste(base_name,"_par_part_iterative.in",sep="")

processors<<-16  # number of processors that need to be the same as the .reach file called ny the .in file
ruta1<<-"/media/D/SourceCodes/SCE_tRIBS/SCE/Event_calibration/BTHOM/"   # path to the R-script and where the
"SCE_for_cluster" folder is.
Output_Behav<<-"OUTPUTS_BEHAV"  #Folder to save and rename the output files mrf, rtf and qout from each of the
simulations. This folder is inside ruta1
GWcal<<- 1   # 1 = if calibrating GWinit; 0 if not
GWfolder<<-"GWinit/"  # name of folder within ruta for GWinit scenarios if GWcal=1.

   if (GWcal==1) listaGW= dir(path=paste(ruta,GWfolder,sep=""),all.files=FALSE,full.names=FALSE,recursive=FALSE)

Routing<<-1  # # 1 = if calibrating routing pars; 0 if not
Routing_pars<<-c(54,164)  # 57=Manning; 48=Kinematcoeff=48, 54=flowexp; coeff_w-A_rel=63; exp_w-A_rel=66;
Bedrock_depth=164
Routing_ref<<-c(0.4,2) # reference values for the chosen routing parameters
lower_routing<<-c(0.3,0.25)   # lower limits for the ruting pars
upper_routing<<-c(0.45,3)     # upper limits for the ruting pars

# The soil parameters to optimize:
# x=[Ks, Qs,  Qr,  m, Ksi, f, As, Au,  n,  Ks,  Cs]
# x=[x1, x2, x3,  x4, x5, x6, x7, x8,  x9, x10, x11]

soil_types<<-c("3","13")  # soil types to calibrate
choose_soils<<-c(1,2,4,5,6,7)   # Choose the variables to iterate from ref= "1=Ks" "2=Qs," "3=Qr" "4=m" "5=Ksi" "6=f"
"7=As" "8=Au" "9=n" "10=Ks" "11=Cs"

consider_A_same=1   # Consider anysotropy ratios the same? Unsaturated = saturated, As=Au?  1= yes, 0 = no
#values<<-     c(var1,var2,var3,var4,var5,var6,var7,var8...etc)  in order of soil types...

values_soils<<-c(10.9,0.412,  0.378, -146.6,    0.008758, 223,   0.35,    0.01,  0.165,   -1,   0.006884, 1.5)  #vector of initial
conditions of the selected variables (choosev x soil_types) in  order. For example in the case of 4 pars the first 4 values are
the corresponding to the first soil class and the following four are for the second soil type. The rest of paremeters that will
not be calibrated need to be prescribed at the .sdt file.
lower_soils<<-c(0.36,  0.271,  0.140,  -454.7,  0.0003,  1,      0.0036,  0.01,  0.037,  -1000,  0.0003, 1)     #lower boundaries
for the variables range
upper_soils<<-c(36,   0.608,   2.0,     0,      0.05,    1000,    3.6,     0.1,  0.293,    0,     0.05,  2)     #upper boundaries for the
variables range
complejos<<-5

tolerance<<-0.00001 # tolerance for consecutive iterations
decim<<-6  # digits for the output and the sdt files
walltime<<-700  #mins... Time after which a new job should be sent, as the current is taking too much time. This time must
be at least 20 minutes before the walltime used in the jobscript to the cluster.
longdurationRMSE<<-10   # RMSE for a simulation of duration > walltime

## OPTIONAL SETTINGS ^^^^^^^^^^^^^^^^^^^^^^^^^^^^^^^^^^^^^^^^
# If the user has less than 12 and different organization of classes do not worry, only assign 0 (zero) to new_groups and this
condition does not make effect.
new_groups<<-2  # The number of new groups of parameters that will have the same parameterization. For example the
classes (13) Unweathered Bedrock,(15)Stones, (19)Weathered Bedrock,(20) Fragments could have the same
parameterization. Those will conform a new group.
```

```
group1<<-c(13,15,19,20)   # the first component of this vector is the independent class that appears in the vector
"soil_types"
n1<<-length(group1)       #this line must accompany the line before
group2<<-c(3,16,17,18)    # the first component of this vector is the independent class that appears in the vector
"soil_types"
n2<<-length(group2)       #this line must accompany the line before
# ... Continue to name as many groups as specified by new_groups. For example if there are four groups the fourth group
will be group4 and the base class will be base4

bases<<-c(group1[1],group2[1])     #include here the first elements of the number of groups that you have
groups<<-c(group1,group2)  #include here the number of groups you have
length_groups<<-c(n1-1,n2-1)  #include here the number of n's you have minus one in all of them

## Programmed cluster shutdowns
startingshut<<-c(2012,3,19,22)   # enter the year,month, day, military hour of the cluster shutdown and R will pause
n_hours_shut
n_hours_shut<<- 60 # number of hours that the program must be paused


## END OF OPTIONAL SETTINGS ^^^^^^^^^^^^^^^^^^^^^^^^^^^^^^^^
## END OF INPUT SECTION
#########################################################################################
#*****************************************************************************************************
*******
vec_routing=rbind(c(57,"Manning"),c(48, "Kinematcoeff"),c(54,"Flowexp"),c(63,"a_W-A"),c(66,"b_W-
A"),c(164,"Bedrock"))  # These numbers should correspond to the lines to replace in the iterative.in file

if (Routing==1) {
  lower_soils=c(lower_soils,lower_routing)
  upper_soils=c(upper_soils,upper_routing)
  }

if (GWcal==1) {
  lower_soils=c(lower_soils,1)
  upper_soils=c(upper_soils,length(listaGW))
  }

tiempo<<-as.character(Sys.time())
nbehaviorals=complejos*((2*(length(values_soils)+GWcal+(Routing*length(Routing_pars))))+1)
status_before<-"I"   # Initial status
path_to_sce_alg<<-paste(ruta1,"SCE_for_cluster/",sep="")#"/media/cluster/SCE/"
logtxt<<-paste(base_name,"_log.txt",sep="")
node<<-rep(1:3,10000)   # 3 computational nodes to use... if one is broken
soilparameters<<-
c("Sat.Hyd.Cond_","Sat.SMC","Res.SMC","PoreIndex","AirEntryPress_","DecayPar_","Anis.Rat_","Anis.Rat_","Tot.Por
os._","Vol.Heat.Cond_","SoilHeat.Cap_")
vars<<-soilparameters[choose_soils]

name_vars<<-rep(NA,length(values_soils))
  for (v in 1:length(soil_types)) {
    empiece=((v-1)*length(choose_soils))+1
    name_vars[empiece:(empiece+length(choose_soils)-1)]=paste(vars,rep(soil_types[v],length(choose_soils)),sep='')
  }

if (Routing==1) {
    for (vv in 1:length(Routing_pars)){
                cual=which(as.numeric(vec_routing[,1])==Routing_pars[vv])
                name_vars=c(name_vars,vec_routing[cual,2])
    }
}

if (GWcal==1) name_vars=c(name_vars,"GWinit")

# Complete soils information ##
table_sdt<<-read.table(paste(ruta,"Input/",base_name,".sdt",sep=''),skip=1) # Initial values for the soil parameters
refe<<-matrix(NA,length(soil_types),12)
  for (u in 1:length(soil_types)){
```

```
      refe[u,]=as.numeric(table_sdt[as.numeric(soil_types[u]),1:12])  # the soil type and all 11 parameters
  }

base_input<<-paste(base_name,".sdt",sep='')
hyd_PATH<<-paste(ruta,"Output/hyd/",sep="")
iter=1
salga<<-matrix(NA,1,(GWcal+3+length(values_soils)+(Routing*length(Routing_pars))))   # number of expected iterations
colnames(salga)=c("iter","FunctValue","Date-Time",name_vars)
write.table(salga,paste(ruta1,logtxt,sep=''),quote=FALSE,col.names=TRUE,row.names=FALSE)
save(list=ls(all=TRUE),file=paste(ruta1,"all.Rdata",sep=''))
#setwd(ruta)  # important because the tRIBS outputs are going ro be written in this path

if (Routing==1) values_soils=c(values_soils, Routing_ref)
if (GWcal==1) values_soils=c(values_soils, 1)    # fuse the soils with the GW inint condition. starts with the wettest
condition

## Rosenbrock Banana function
  RMSES <- function(x){
    longjob<<-0
  # check for programmed shutdowns
     pa= substring(tiempo, 1:nchar(tiempo), 1:nchar(tiempo))
     yearshut=as.numeric(paste(pa[1],pa[2],pa[3],pa[4],sep=''))
     monthshut=as.numeric(paste(pa[6],pa[7],sep=''))
     dayshut=as.numeric(paste(pa[9],pa[10],sep=''))
     hourshut=as.numeric(paste(pa[12],pa[13],sep=''))
    if (yearshut==startingshut[1] & monthshut==startingshut[2] & dayshut==startingshut[3] & hourshut==startingshut[4]) {
    cat(paste("R went to sleep at ",tiempo, " for cluster shutdown during ",n_hours_shut," hours",sep=''),fill=TRUE)
    Sys.sleep(n_hours_shut*3600)
    }
#
  cat("now trying: x= ",fill=TRUE)
  cat(x,fill=TRUE)
   solosuelos<<-x[1:(length(x)-GWcal-(Routing*length(Routing_pars)))]
for (w in 1:(length(soil_types))) {
      fir=((w-1)*length(choose_soils))+1
      refe[w,((choose_soils[1:length(choose_soils)])+1)]=round(solosuelos[fir:(fir+length(choose_soils)-1)],digits=decim)
## try to decrease the number of digits
  }

 if (consider_A_same==1) refe[,9]=refe[,8]

  values_soils<<-x

  if (iter==1) onset<<-as.character(Sys.time())

  #Opens the .sdt file and writes values
  iter<<-iter+1
  cat("Line 186",fill=TRUE)
  wait(system(paste("ls /media/cluster/ >",ruta1,base_name,"_zj.txt",sep="" )),timeout=5)
  infor00<-file.info(paste(ruta1,base_name,"_zj.txt",sep=""))
    if (as.numeric(infor00[1])==0){
    source(paste(ruta1,"function1_cluster_link.R",sep=''))  # script to check cluster link connection
    Q0(iter)
    }

  #start writing the sdt file
  yup= read.fwf(paste(ruta,"Input/",base_input,sep=''),width=200)  # reads fixed-width data
  yum=as.matrix(yup)

  for (u in 1:length(soil_types)){
     yum[as.numeric(soil_types[u])+1]=paste(refe[u,1]," ",refe[u,2]," ",refe[u,3]," ",refe[u,4]," ",refe[u,5]," ",refe[u,6],"
",refe[u,7]," ",refe[u,8]," ",refe[u,9]," ", refe[u,10]," ",refe[u,11]," ",refe[u,12],sep="")
      #optional grouping runs here
       if (new_groups>0){
                  if (any(bases==refe[u,1])){
                    cual=which(groups==refe[u,1])
                    bas=which(bases==refe[u,1])
```

```
for (jj in (cual+1):(cual+length_groups[bas])){
                        yum[groups[jj]+1]=paste(groups[jj],",",refe[u,2],",",refe[u,3],",",refe[u,4],",",refe[u,5],",",refe[u,6],",",refe[u,7],",",refe[u,8],",",refe[u,9],",",refe[u,10],",",refe[u,11],",",refe[u,12],sep="")
                        }
            }
   }
  }

  yum_da_fr=as.data.frame(yum)

  # writes the sdt file

write.table(yum_da_fr,paste(ruta,"Input/",base_name,".sdt",sep=''),quote=FALSE,col.names=FALSE,row.names=FALSE)

  # start writing the .in files
     yupin= read.fwf(paste(ruta,infile,sep=""),width=85,fill=TRUE)  # reads fixed-width data as a dataframe
     yui2=scan(paste(ruta,infile,sep=""),what="character")  # reads many characters
               for (i in 1:dim(yupin)[1]) {     # within yui2 the first dim(yup)[1] values are put
               yui2[i]=as.character(yupin[i,1])
               }
     yui3=yui2[1:dim(yupin)[1]]   #makes yui3 only equal to the first dim(yup)[1] values

     for (gu in 1:length(Routing_pars)){
              yui3[Routing_pars[gu]]=values_soils[length(solosuelos)+gu]
     }

     # writes the in file
     Pre <- file(paste(ruta,iterative_in,sep=''), "w") # open an output file connection
     cat(yui3, file = Pre, sep = "\n")    #writes in that file
     close(Pre)    # closes the connection


  cat("Line 238",fill=TRUE)
  wait(system(paste("ls /media/cluster/ >",ruta1,base_name,"_zj.txt",sep="" )),timeout=5)
  infor00<-file.info(paste(ruta1,base_name,"_zj.txt",sep=""))
   if (as.numeric(infor00[1])==0){
   source(paste(ruta1,"function1_cluster_link.R",sep=''))  # script to check clulster link connection
   Q0(iter)
   }


   # extract and copy the GW case
    if (GWcal==1){
    GWcase<<-round(values_soils[length(values_soils)])
    file.copy(paste(ruta,GWfolder,listaGW[GWcase],sep=""),
paste(ruta,"Input/",base_name,".iwt",sep=""),overwrite=TRUE)
    }
#

  cat("Line 252",fill=TRUE)
  wait(system(paste("ssh hamoreno@saguaro.fulton.asu.edu /usr/bin/qsub ",cluster_simulation_folder,parallel_jobscript," >
",ruta1,base_name,"_fj.txt",sep=""),intern=FALSE, ignore.stderr = FALSE,wait=FALSE),timeout=10)
  infor0<<-file.info(paste(ruta1,base_name,"_fj.txt",sep=""))
  if (as.numeric(infor0[1])==0){
  source(paste(ruta1,"function2_ssh_broken_pipe.R",sep=''))  # script to check clulster link connection
  Q1(iter)
  }
  jobid<<-as.character(read.table(paste(ruta1,base_name,"_fj.txt",sep=""))[1,1])
  cat(jobid,fill=TRUE)

auxcount<-0
for (counterr in 1:10000){
              auxcount<-auxcount+1
              counterr<-counterr
              cat("Line 266",fill=TRUE)
              #sj<-wait(system(paste("ssh hamoreno@saguaro2.fulton.asu.edu /usr/local/bin/qstat -a >
",ruta1,base_name,"_salgaex.txt",sep=""),intern=FALSE, ignore.stderr = FALSE,wait=FALSE),timeout=10)
```

```
            sj<-wait(system(paste("ssh hamoreno@saguaro.fulton.asu.edu /usr/bin/qstat ",jobid," >",
ruta1,base_name,"_salgaex.txt",sep=""),intern=FALSE, ignore.stderr = FALSE,wait=FALSE),timeout=10)
            infor<-file.info(paste(ruta1,base_name,"_salgaex.txt",sep=""))

                # In case of communication fails for qstat -a
                 if (as.numeric(infor[1])==0) {
                        source(paste(ruta1,"function3_qstat_failure.R",sep=""))  # script to check qstat fail
                        Q2(infor)
                        }

            SAL=read.table(paste(ruta1,base_name,"_salgaex.txt",sep=""),skip=2)
            status=as.character(SAL[1,5])

             if (status=="C" & status_before=="Q"){   # In case of the error when the job is canceled after Queued..re-
submit another job
              cat("Line 281... Completed without running.. abnormal (C)...sending a new jobscript",fill=TRUE)
              wait(system(paste("ssh hamoreno@saguaro.fulton.asu.edu /usr/bin/qsub
",cluster_simulation_folder,parallel_jobscript," > ",ruta1,base_name,"_fj.txt",sep=""),intern=FALSE, ignore.stderr =
FALSE,wait=FALSE),timeout=10)
              infor0<-file.info(paste(ruta1,base_name,"_fj.txt",sep=""))
                 if (as.numeric(infor0[1])==0){
                 source(paste(ruta1,"function2_ssh_broken_pipe.R",sep=""))  # script to check clulster link connection
                 Q1(iter)
                 }
               auxcount<-1
               jobid<<-as.character(read.table(paste(ruta1,base_name,"_fj.txt",sep=""))[1,1])
               cat(jobid,fill=TRUE)
             }

                 if ((status=="Q") & (auxcount==walltime)){   # Too long runs are canceled and re-submitted
                 cat("Line 294... Job is taking too loong to start.. deleting and starting a new one...",fill=TRUE)
                 wait(system(paste("ssh hamoreno@saguaro.fulton.asu.edu /usr/bin/qdel ",jobid,sep=""),intern=FALSE,
ignore.stderr = FALSE,wait=FALSE),timeout=10)
                 Sys.sleep(15)
                 wait(system(paste("ssh hamoreno@saguaro.fulton.asu.edu /usr/bin/qsub
",cluster_simulation_folder,parallel_jobscript," > ",ruta1,base_name,"_fj.txt",sep=""),intern=FALSE, ignore.stderr =
FALSE,wait=FALSE),timeout=10)
                 Sys.sleep(15)
                 infor0<-file.info(paste(ruta1,base_name,"_fj.txt",sep=""))
                 Sys.sleep(15)
                            if (as.numeric(infor0[1])==0){
                            source(paste(ruta1,"function2_ssh_broken_pipe.R",sep=""))  # script to check clulster link
connection
                            Q1(iter)
                            }
                 auxcount<-1
                 jobid<<-as.character(read.table(paste(ruta1,base_name,"_fj.txt",sep=""))[1,1])
                 cat(jobid,fill=TRUE)
                 }

                if ((status=="R") & (auxcount==walltime)){   # Too long runs are canceled and re-submitted
                 cat("Line 311... Job is taking too long.. canceling and assigning the longdurationRMSE",fill=TRUE)
                 wait(system(paste("ssh hamoreno@saguaro.fulton.asu.edu /usr/bin/qdel ",jobid,sep=""),intern=FALSE,
ignore.stderr = FALSE,wait=FALSE),timeout=10)
                 Sys.sleep(15)
                 longjob<<-1
                 break
                 }



            if (status=="C") {
            break
            } else {
            cat(paste("waiting for completed status_",auxcount,"mins status: ",status,"....time:
",as.character(Sys.time()),sep=""),fill=TRUE)
            status_before=status
            Sys.sleep(50)
```

```
            }
}

if (longjob==0){

tiempo<<-as.character(Sys.time())
 source(paste(path_to_sce_alg,"Q_out_Q_obs_Rain_for_SCE.r",sep=''))
 Q(d,year,month,day,hour,hyd_PATH,observed_PATH,obs_name,init)
 cat("---",sep="")
 cat("---- x=",x,"--Function_value=",sqrt((sum(SEE_PIX1))/(n)),"..iteration=",iter-1,"..",
 tiempo,"..Started at..",onset,fill=TRUE)
 salga[1,1]=iter-1
 salga[1,4:(3+length(values_soils)-GWcal)]=round(values_soils[1:(length(values_soils)-GWcal)],digits=decim)
 if (GWcal==1)  salga[1,length(values_soils)+3]=round(values_soils[length(values_soils)])
 salga[1,2]=round(sqrt((sum(SEE_PIX1))/(n)),digits=7)
 salga[1,3]=tiempo
 #salgai=rbind(salgai,salga)
 #if (iter==2) {
 save(list=ls(all=TRUE),file=paste(ruta1,"RMSES.Rdata",sep=''))
 write.table(salga,paste(ruta1,logtxt,sep=''),append=TRUE,quote=FALSE,col.names=FALSE,row.names=FALSE)
 if (iter==2) {
 RMSESold<<-sqrt((sum(SEE_PIX1))/(n))
 } else {
 RMSESold<<-c(RMSESold,sqrt((sum(SEE_PIX1))/(n)))
 }

pad= substring(d, 1:nchar(d), 1:nchar(d))
if (length(pad)==1) durm=paste("000",d,sep="")
if (length(pad)==2) durm=paste("00",d,sep="")
if (length(pad)==3) durm=paste("0",d,sep="")
if (length(pad)>=4) durm=d

 if (iter < (nbehaviorals+1)){
 cat("Copying files",fill=TRUE)
 file.copy(paste(ruta,"Output/hyd/",base_name,durm,"_00.mrf",sep=""),
paste(ruta1,Output_Behav,"/",iter,"_",base_name,durm,"_00.mrf",sep=""),overwrite=TRUE)
 file.copy(paste(ruta,"Output/hyd/",base_name,durm,"_00.rft",sep=""),
paste(ruta1,Output_Behav,"/",iter,"_",base_name,durm,"_00.rft",sep=""),overwrite=TRUE)
 file.copy(paste(ruta,"Output/hyd/",base_name,"_Outlet.qout",sep=""),
paste(ruta1,Output_Behav,"/",iter,"_",base_name,"_Outlet.qout",sep=""),overwrite=TRUE)
               if (iter>2){
                 if (sqrt((sum(SEE_PIX1))/(n))<min(RMSESold[1:(iter-2)])) {
                 cat("Optimum found",fill=TRUE)
                 file.copy(paste(ruta,"Output/hyd/",base_name,durm,"_00.mrf",sep=""),
paste(ruta1,Output_Behav,"/",1,"_",base_name,durm,"_00.mrf",sep=""),overwrite=TRUE)
                 file.copy(paste(ruta,"Output/hyd/",base_name,durm,"_00.rft",sep=""),
paste(ruta1,Output_Behav,"/",1,"_",base_name,durm,"_00.rft",sep=""),overwrite=TRUE)
                 file.copy(paste(ruta,"Output/hyd/",base_name,"_Outlet.qout",sep=""),
paste(ruta1,Output_Behav,"/",1,"_",base_name,"_Outlet.qout",sep=""),overwrite=TRUE)
                 }
               }
 } else {
 if (sqrt((sum(SEE_PIX1))/(n))<min(RMSESold[1:(iter-2)])) {
      cat("Optimum found",fill=TRUE)
               file.copy(paste(ruta,"Output/hyd/",base_name,durm,"_00.mrf",sep=""),
paste(ruta1,Output_Behav,"/",1,"_",base_name,durm,"_00.mrf",sep=""),overwrite=TRUE)
               file.copy(paste(ruta,"Output/hyd/",base_name,durm,"_00.rft",sep=""),
paste(ruta1,Output_Behav,"/",1,"_",base_name,durm,"_00.rft",sep=""),overwrite=TRUE)
               file.copy(paste(ruta,"Output/hyd/",base_name,"_Outlet.qout",sep=""),
paste(ruta1,Output_Behav,"/",1,"_",base_name,"_Outlet.qout",sep=""),overwrite=TRUE)
  }
 }

 sqrt((sum(SEE_PIX1))/(n))  #
 } else {
 salga[1,1]=iter-1
 salga[1,4:(3+length(values_soils)-GWcal)]=round(values_soils[1:(length(values_soils)-GWcal)],digits=decim)
```

```
 if (GWcal==1)  salga[1,length(values_soils)+3]=round(values_soils[length(values_soils)])
 salga[1,2]=longdurationRMSE
 salga[1,3]=tiempo
 save(list=ls(all=TRUE),file=paste(ruta1,"RMSES.Rdata",sep=""))
 write.table(salga,paste(ruta1,logtxt,sep=''),append=TRUE,quote=FALSE,col.names=FALSE,row.names=FALSE)
 RMSESold<<-c(RMSESold,longdurationRMSE)
 longdurationRMSE
 }
}


source(paste(path_to_sce_alg,"SCEoptim_tRIBS.R",sep=""))
ans <- SCEoptim(RMSES, values_soils,lower= lower_soils,upper = upper_soils,control = list(trace = 2,fnscale=1,
            reltol=tolerance,tolsteps=7,maxtime=Inf,ncomplex=complejos))
str(ans)
```

APPENDIX E

STORM SCALE ANALYSIS

This Appendix constitutes additional material for the interpretation of Figures 4.11, 4.12 and 4.13 in Chapter 4 that postulated the typical scale of mountain storms as the main responsible of the increased uncertainty at middle size basins. Estimations of the typical size of convection systems are dictated by the presence of distinguishable storm cores. The Figure E.1 represents the spatial coverage of main precipitation cores during Storm 2004 at BUCK, NFORK, BTHOM, LTHOM and Storm 2006 at NVRAIN, MVRAIN, SVRAIN, MBOUL, COAL, RALS, as percent of total basin area (black bars) and actual scale (km^2, red bars). This analysis was performed for three different precipitation thresholds (P_T) of 0.8, 0.5 and 0.3 times the maximum cumulative precipitation (P_{max}) at each individual watershed. In other words, the size of storm cores is determined by different percentiles of the maximum precipitation in the watershed. Evidently, P_T differs among basins and has been added at the top of each bar for purposes of comparison. The Figure 4.3 can be used as supplemental aid for visualizing the distribution of rainfall and maximum values at each basin. The selection of $P_i > 0.3P_{max}$ (Figure E.1e,f) results in large storm coverage but insignificant flooding responses across watersheds, as the selected threshold is quite low for representing storm cores. On the other hand, $P_i > 0.5P_{max}$ (Figure E.1c,d) decreases the coverage of the storm, but still does not capture storm cores correctly. Finally, $P_i > 0.8P_{max}$ (Figure E.1a,b) represent areas of significant precipitation (larger than the 80 percentile) that produce flooding across most of the basins and correspond well with the storm cores observed in Figure 4.3. If we

compare the range of increased uncertainty in Figure 4.13 (1 to 10% of A_c) with the typical coverage of the storms in this group (Figure E.1a) we can conclude that convection systems causing of hydrologic uncertainty range approximately between 2 and 20 km^2 in the CFR (see Figure E.1b). In summary increased SE at intermediate scale coincide with the typical size of convection systems whose storm cores cover an overlapping geographic fraction of the basin area.

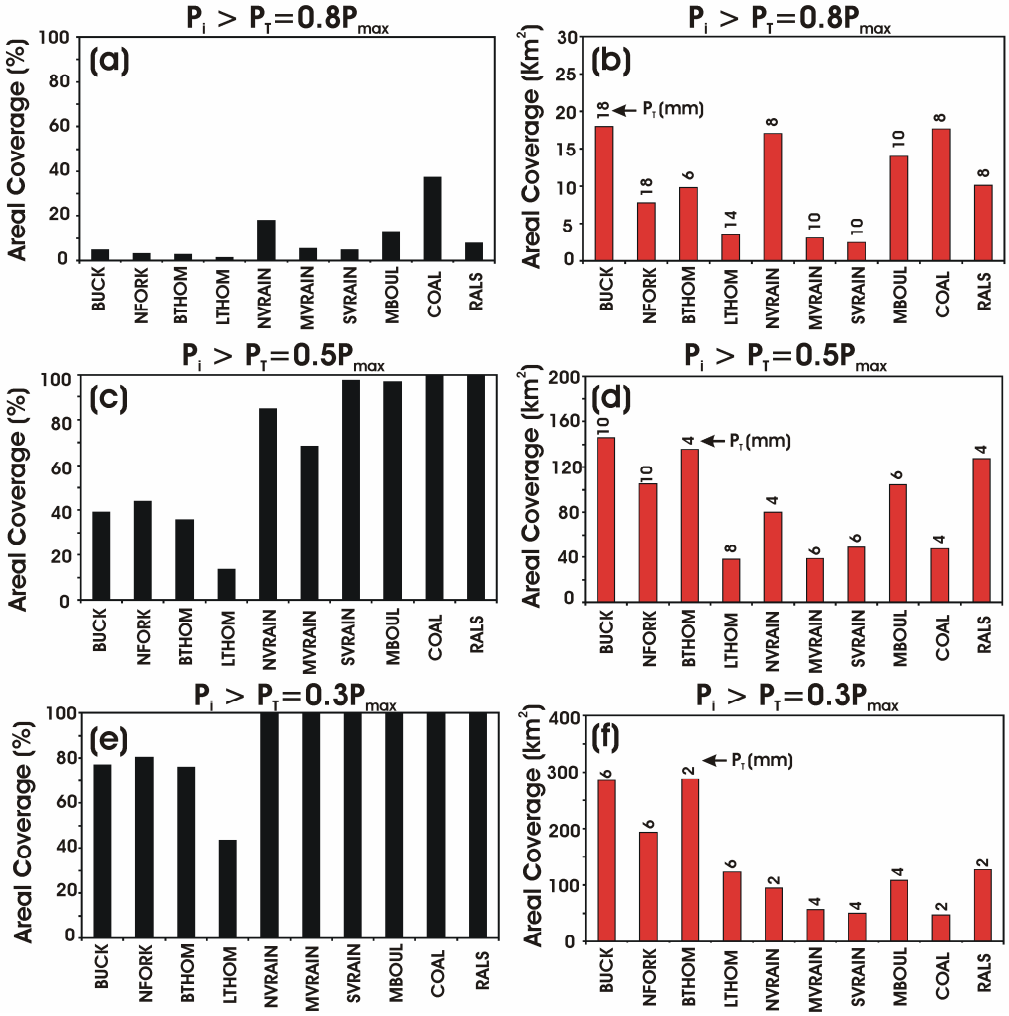

Figure E.1. Spatial coverage of Storm 2004 at BUCK, NFORK, BTHOM, LTHOM and Storm 2006 at NVRAIN, MVRAIN, SVRAIN, MBOUL, COAL, RALS, as dictated for three precipitation thresholds (P_T) in km^2 (red bars) and as a fraction of the total basin area (blackbars).

APPENDIX F

RUNOFF SCALE ANALYSIS

This Appendix constitutes additional material for the interpretation of Figure 4.12 in Chapter 4 that postulated that increases in the runoff coefficient in areas that are fully covered by the storm cores are the responsible for rises in prediction uncertainty as expressed by SE. We analyze the behavior of the spatial distribution of cumulative runoff (Storm event accumulations) averaged per sub-basin area. Selected internal locations match those selected in Chapter 4, from Figures 4.10 to 4.13. The Figure F.1 summarizes the results for one testing watershed (LTHOM) whose spatially-varying runoff maps were produced and shown in Figure 4.9. The Figure F.1 shows the total storm runoff per sub-basin scale with standard deviation bars representing the dispersion from ensemble members, while Figures F.2a,b summarize mean and standard deviation from Figure F.1. A careful analysis to Figure F.1 reveals that runoff production patterns are analogous to those found in Figure 4.11 for LTHOM with increasing values at spatial scales ranging between 1 and 10 Km^2. Likewise, Figures F.2a,b recall similar patterns found in Figure 4.13 for the same watershed. These results show that areas directly below storm cores, whose scales coincide with the preliminary storm size analysis (between 2 and 20 km^2) are the responsible for increased flood forecasting uncertainty through an average increase in the runoff production rates.

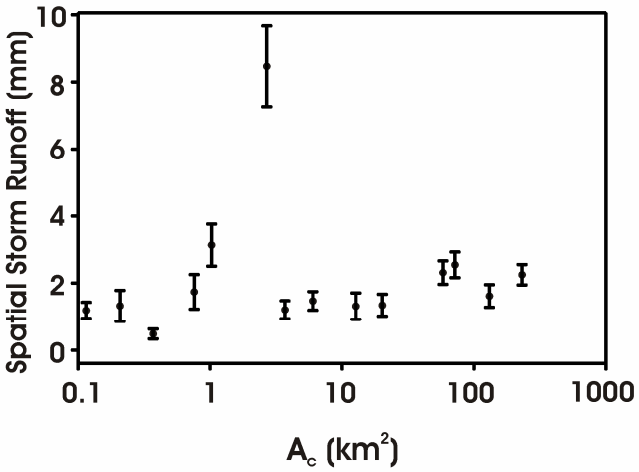

Figure F.1. Mean and standard deviation of cumulative ensemble runoff production per sub-basin areas (A_c) in LTHOM for Storm 2004.

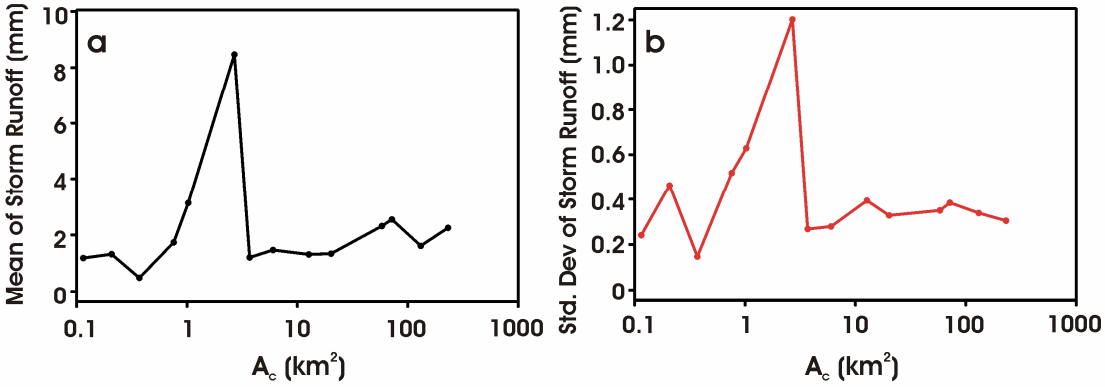

Figure F.2. (a) Mean and (b) standard deviation of cumulative ensemble runoff production per sub-basin scales (A_c) in LTHOM for Storm 2004.

This document was generated using the Graduate College Format Advising tool. Please turn a copy of this page in when you submit your document to Graduate College format advising. You may discard this page once you have printed your final document. DO NOT TURN THIS PAGE IN WITH YOUR FINAL DOCUMENT!
Font Type: TimesNewRoman
Font size: 12